GSA Data Repository Item 2019167

Lamont, T.N., Searle, M.P., Waters, D.J., Roberts, N.M.W., Palin, R.M., Smye, A., Dyck, B., Gopon, P., Weller, O.M., and St-Onge, M.R., 2019, Compressional origin of the Naxos metamorphic core complex, Greece: Structure, petrography, and thermobarometry: GSA Bulletin, https://doi.org/10.1130/B31978.1.

Data Repository

Supplementary Material

Table S1. ELECTRON MICROPROBE-DERIVED REPRESENTATIVE MINERAL COMPOSITIONS FOR ALL STUDIED SAMPLES (WT% OXIDE AND CATIONS PER FORMULA UNIT)

Compressional origin to the Naxos Metamorphic Core Complex, Greece, Part 1: Supplementary Material

Contents

1. Field relationships and structure of Naxos:

Fieldwork was conducted over five field seasons spanning 2012-2017. During this time, the entire island of Naxos was remapped on a scale of 1:10000. A foliation and lineation map is presented below with accompanying cross-sections and more field photographs of cross-cutting relations and panoramas.

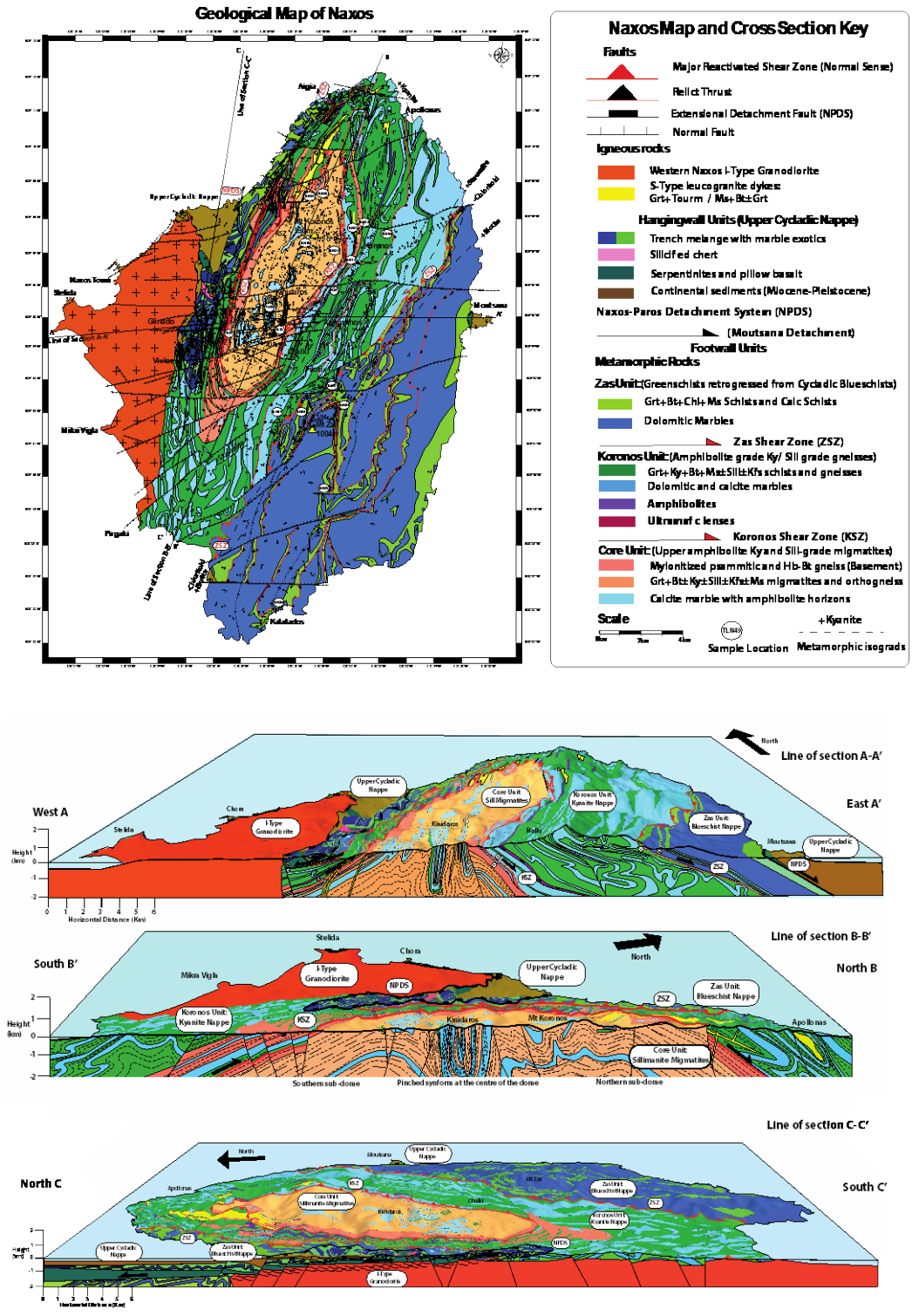

Figure 1.1 Geological map of Naxos and 3D cross sections

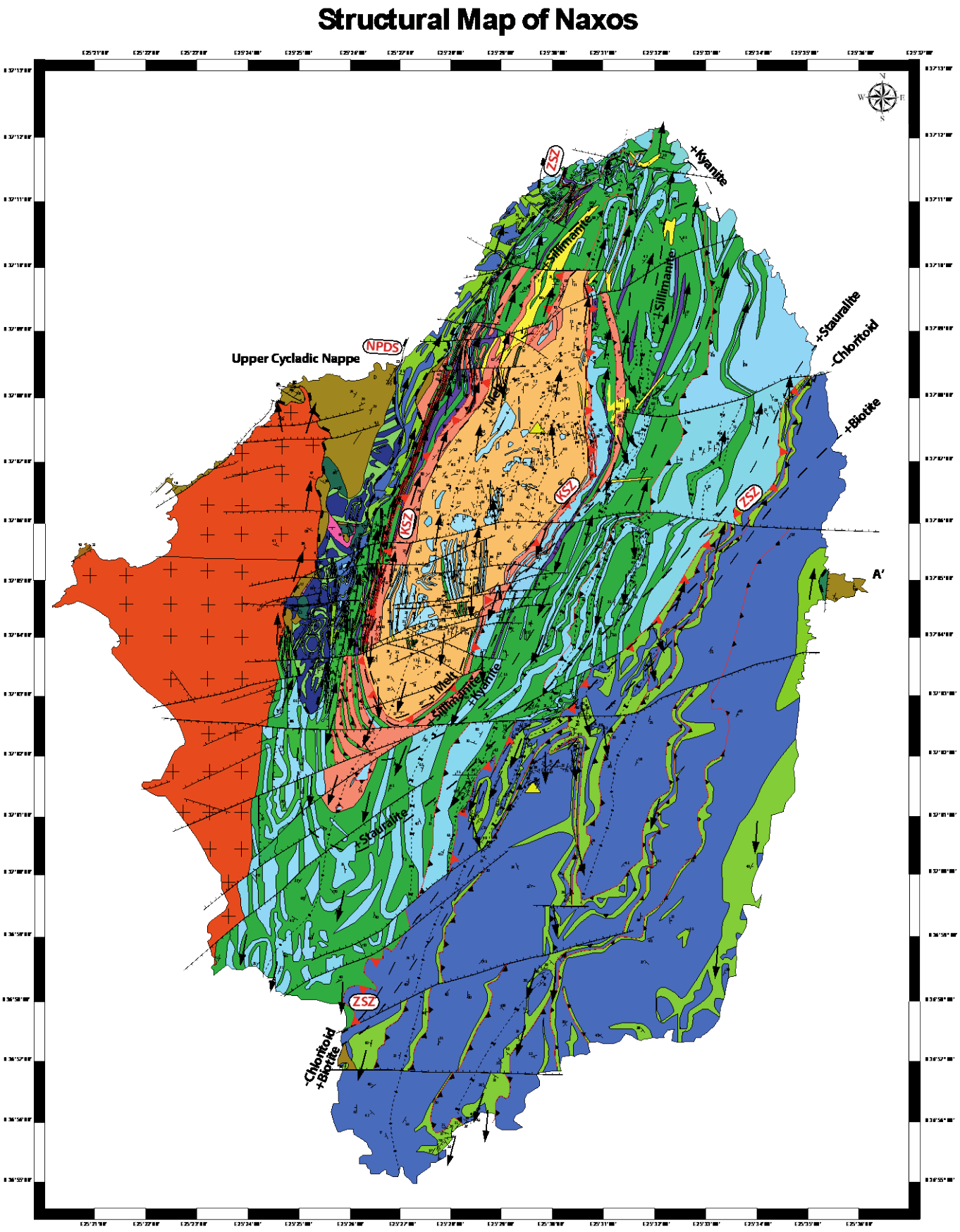

Figure 1.2 Structural map of Naxos with foliations and lineations, note lineations trend NNE-SSW due to doming which post-dates shearing

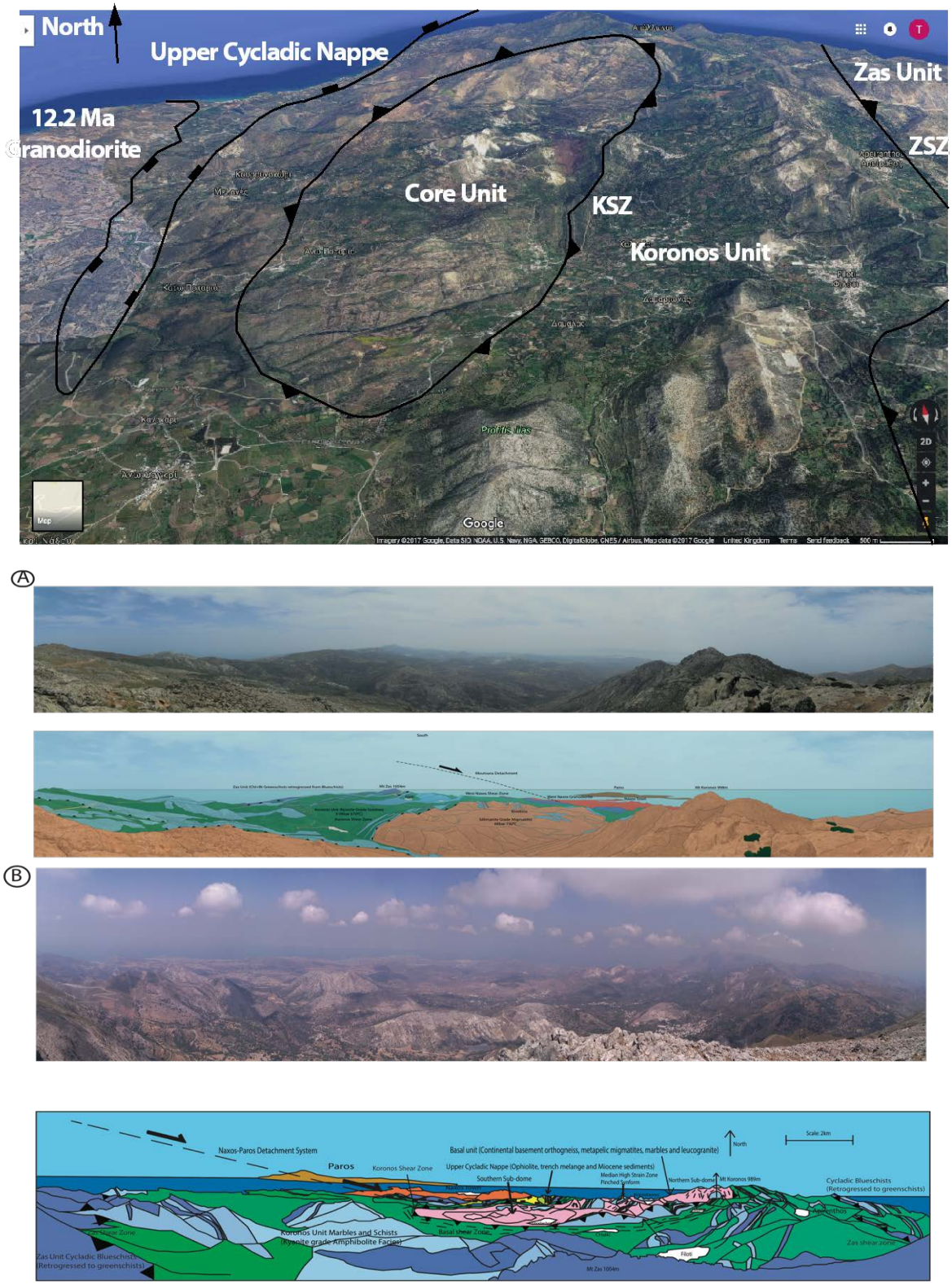

Figure 1.3 Above: Google Earth Imagery in an oblique view looking north over central Naxos showing major structures which can be picked out from the imagery. Below: Annotated panoramic views of the core complex from A) Mt Koronos looking south (N37.126066, E25.502700), B) Mt Zas looking west (N37.030835 E25.501928).

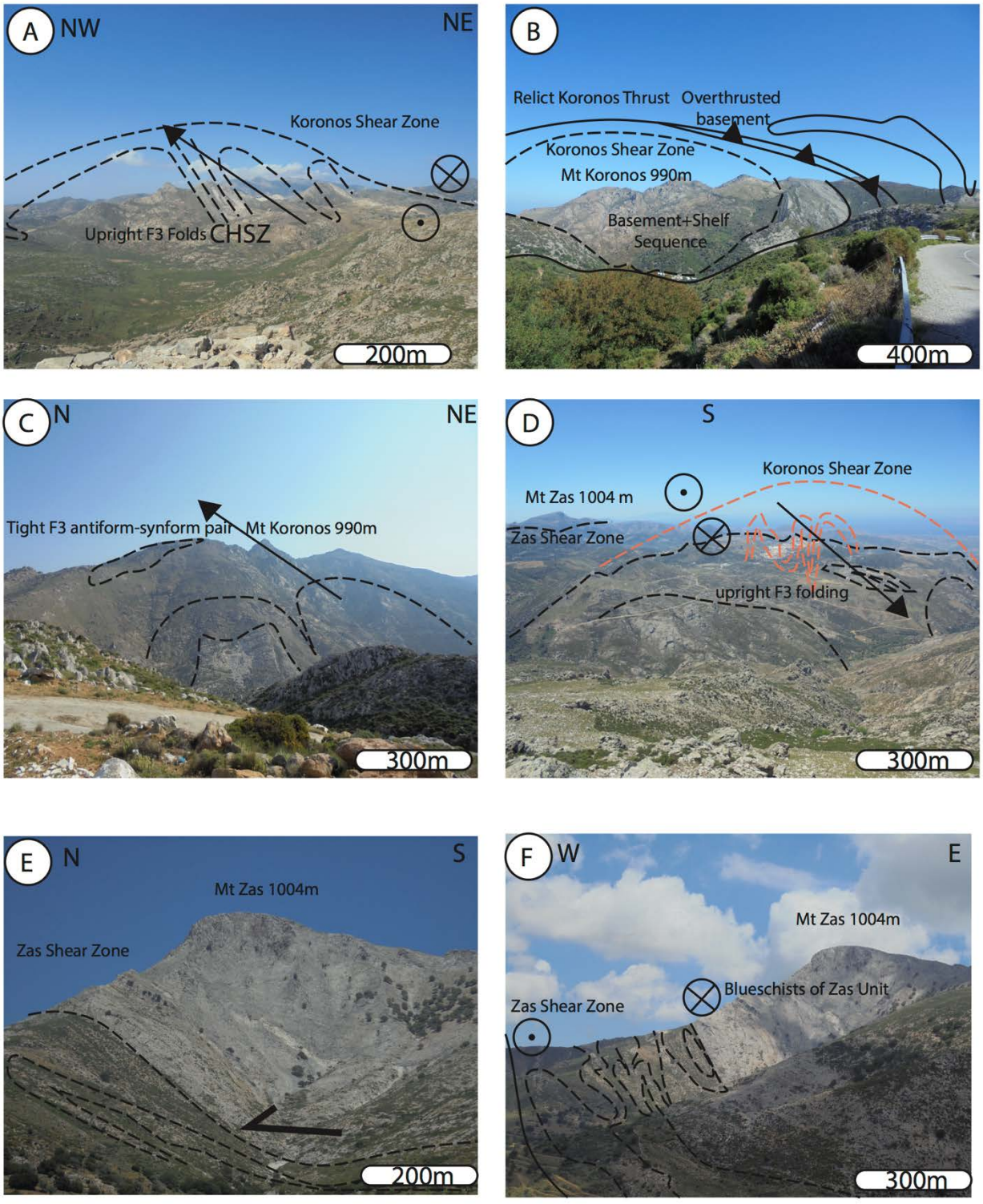

Figure 1.5 Photos of various structures within the Naxos MCC. A) Core High-Strain Zone with upright F_3 folds taken from Apano Kastro looking north (N37.067085, E25.459981), B) Overview of the northern migmatite dome and Mt Koronos taken looking north from (N37.100786, E25.515878), C) Major upright folding under Mt Koronos taken looking north from (37.109200, 25.483767). D) Overview of the southern migmatite dome taken looking south from (N37.124787, E25.514259). E) Zas shear zone looking towards Mt Zas taken from (N37.029856, E25.482163) and F) Taken from (N37.014105, E25.480110)

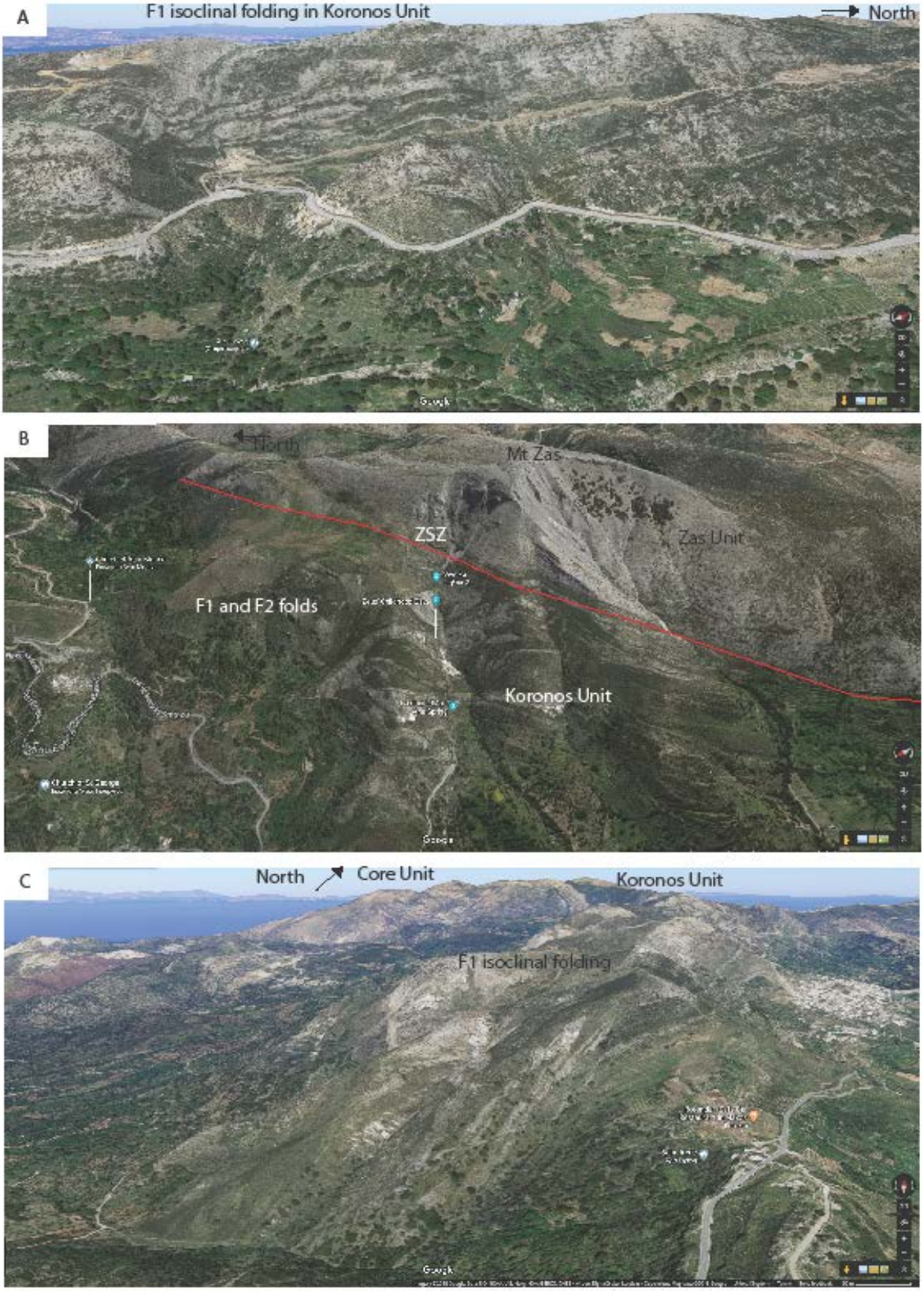

Figure 1.6: Google Earth imagery of some intense F1 and F2 isoclinal folds that can be seen within the light-colored marble bands. A) Sub-horizontal F1 isoclinal folding in the eastern side of Fanari within the Koronos Unit. B) Remnants of F1 isoclinal folds overprinted by F2 folds along the ZSZ overprinted and truncated by top-to-NNE shearing. C) F1 and F2 isoclinal folds in the marble bands above Filoti within the Koronos Unit, note they appear as upright folds but this is due to topographic relief and the fold axes have been rotated by the late doming.

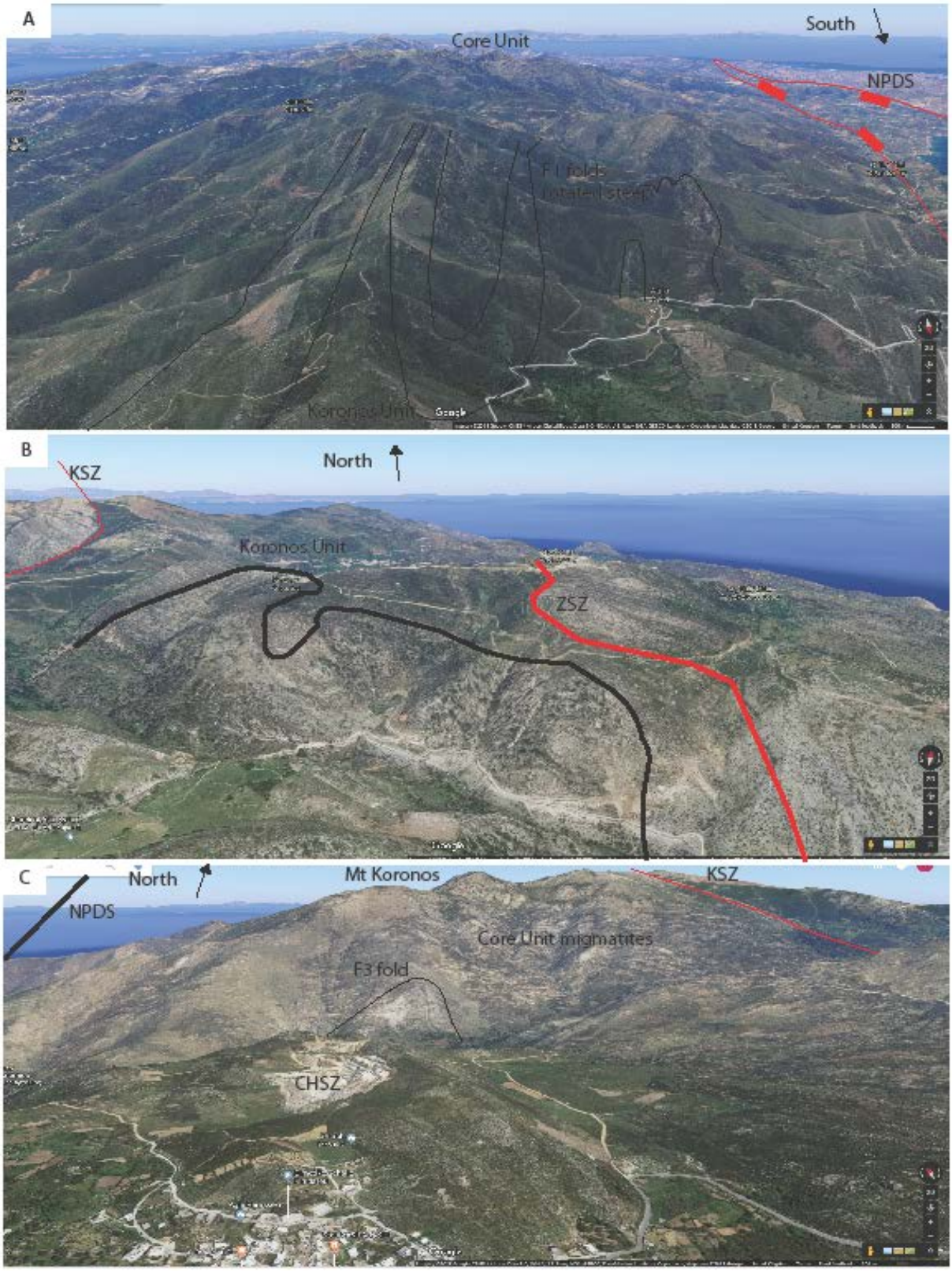

Figure 1.7: More Google Earth imagery of structures within the core complex, the deformation and folding can be picked out by tracing light marble bands. A) Isoclinal folds in the Koronos Unit in Northern Naxos, just structurally above the migmatite dome, showing uprightly folded F3 folds that overprint sub-horizontal isoclinal F1 folds. B) Discorandance between the ZSZ and folded marble bands of the Koronos Unit. C) Internal view of the Core Unit with upright F3 isoclinal folds that can be traced by marble bands within the centre of the dome, note the granitic gneissic protoliths structurally above marbles suggesting structural repetition and thick skinned thrusting prior to doming.

To the first order scale, Naxos could be described as a classic Cordillean–Style metamorphic core complex composed of a metamorphic footwall separated from an un-metamorphosed hanging wall by a brittle-ductile low angle normal fault. However, on the second order scale within the metamorphic footwall, there is evidence for different tectonic units that record different *P–T–t* paths and are associated with structures that are complexly discordant to and truncated by the normal faulting related to crustal extension. In particular, discrete top-to-NNE shear zones separate these tectono-metamorphic units that appear to pre-date deformation associated with crustal extension, and are later folded about the dome. These Shear zones include the Zas Shear Zone (ZSZ) separating retrogressed blueschist-facies rocks of the Zas Unit at high-structural levels from the Barrovian metamorphic rocks at deeper levels. And the Koronos Shear Zone (KSZ) associated with top-to-NNE shearing separating the Core Unit migmatites from the overlying carapace. Along these shear zones there is evidence for thick skinned thrusting as indicated by basement cover repetitions and isoclinal folding, that is overprinted by top-to-NNE shearing. This top-to NNE shearing foliation is defined by kyanite transforming to sillimanite at deep structural levels and greenschist-facies minerals at shallower levels. This foliation is domed with the migmatite dome indicating the decompression of Naxos from-deep to shallow crustal depths was associated with top-to-NNE shearing and doming of migmatites post-dates this shearing. The NPDS associated with regional crustal extension cuts this frozen in metamorphic stratigraphy and is also domed around the island. On the western side of the core complex it dips very steeply that cannot be a result of isostic rebound. A more likely mechanism to explain this as with the large scale doming of the island is a significant component of E-W shortening that even is responsible for rotating Miocene-Pleistocene fluvial sediments. Below we provide further field evidence to support these key points in the paper.

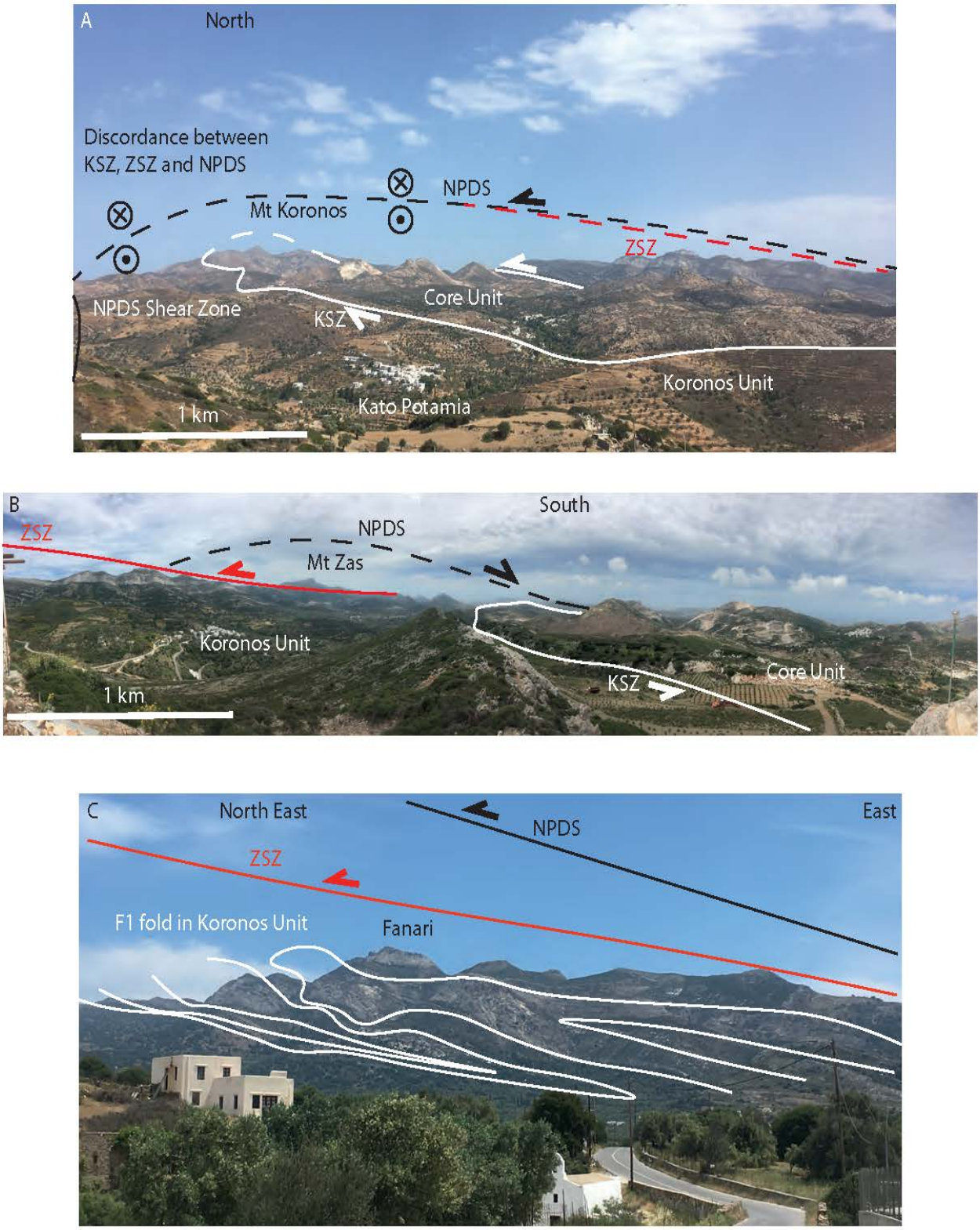

Figure 1.8: Panoramic annotated photographs of the interior of the Naxos MCC: A) Overview of the migmatite dome and metamorphic carapace looking north, showing the discordance between the NPDS and internal structures of the MCC including the KSZ, ZSZ and geometry of the migmatite dome. B) overview of the perimeter of the migmatite dome and KSZ from the summit of Mohni looking south, the KSZ structurally underlies the continuous marble band in the fore-ground for over 10 km along strike. C) Overview of isoclinal and sub horizontal F_1 folds in the Koronos Unit through the Fanari ridge (863 m) looking ENE.

Zas Unit

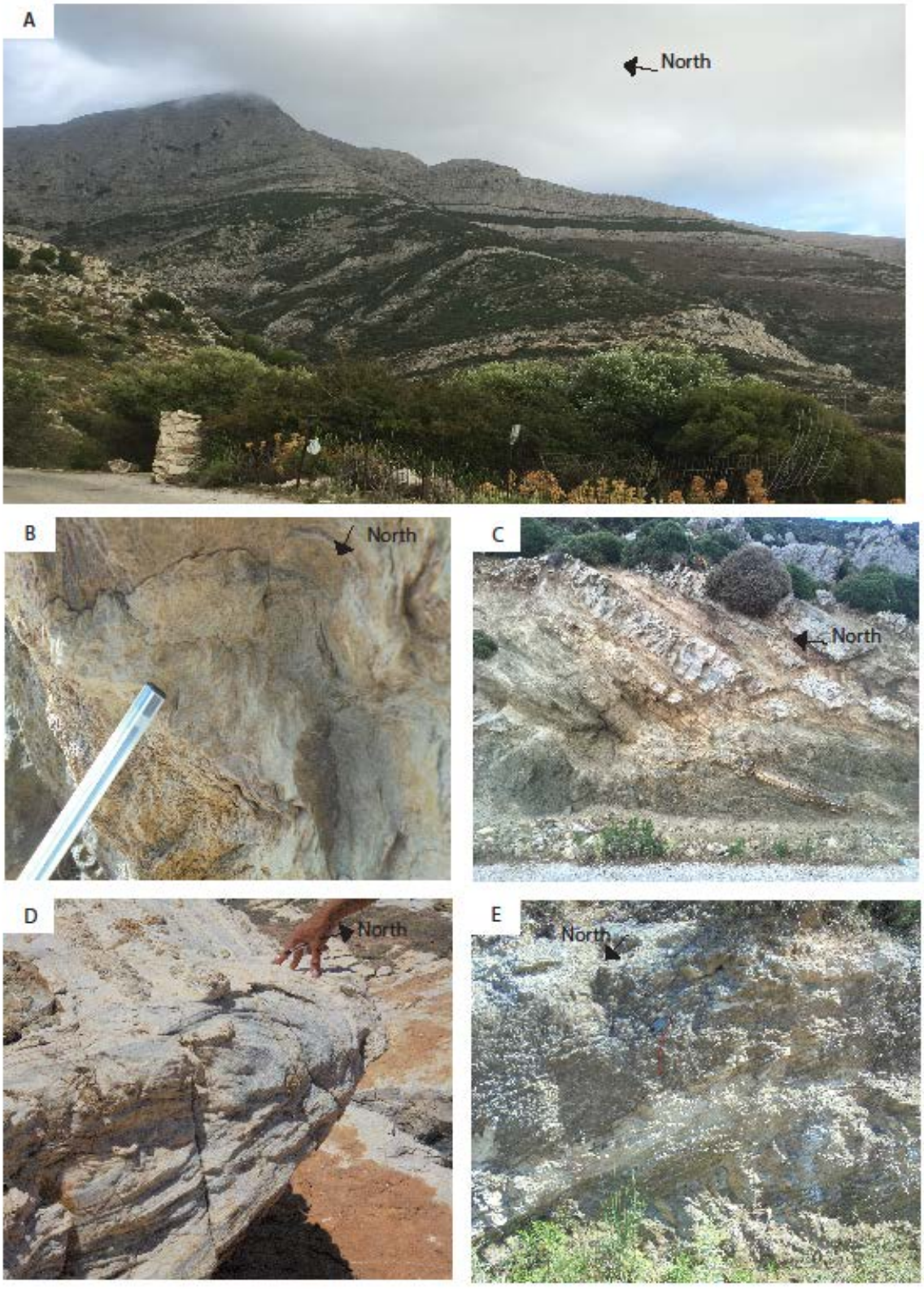

Figure 1.9: Outcrop photographs of the Zas Unit: A) F1 and F2 isoclinal folds under Mt Zas associated with the Zas Shear Zone. B) S_{2a} Crenulation cleavages in qtz-mica schist. C) Zas Shear Zone, intensely sheared dolomitic marbles and schists. D) F2 Isoclinal fold within dolomitic marble at Kalataos Bay. E) Zas Shear Zone intensely deformed calc schists.

Koronos Unit

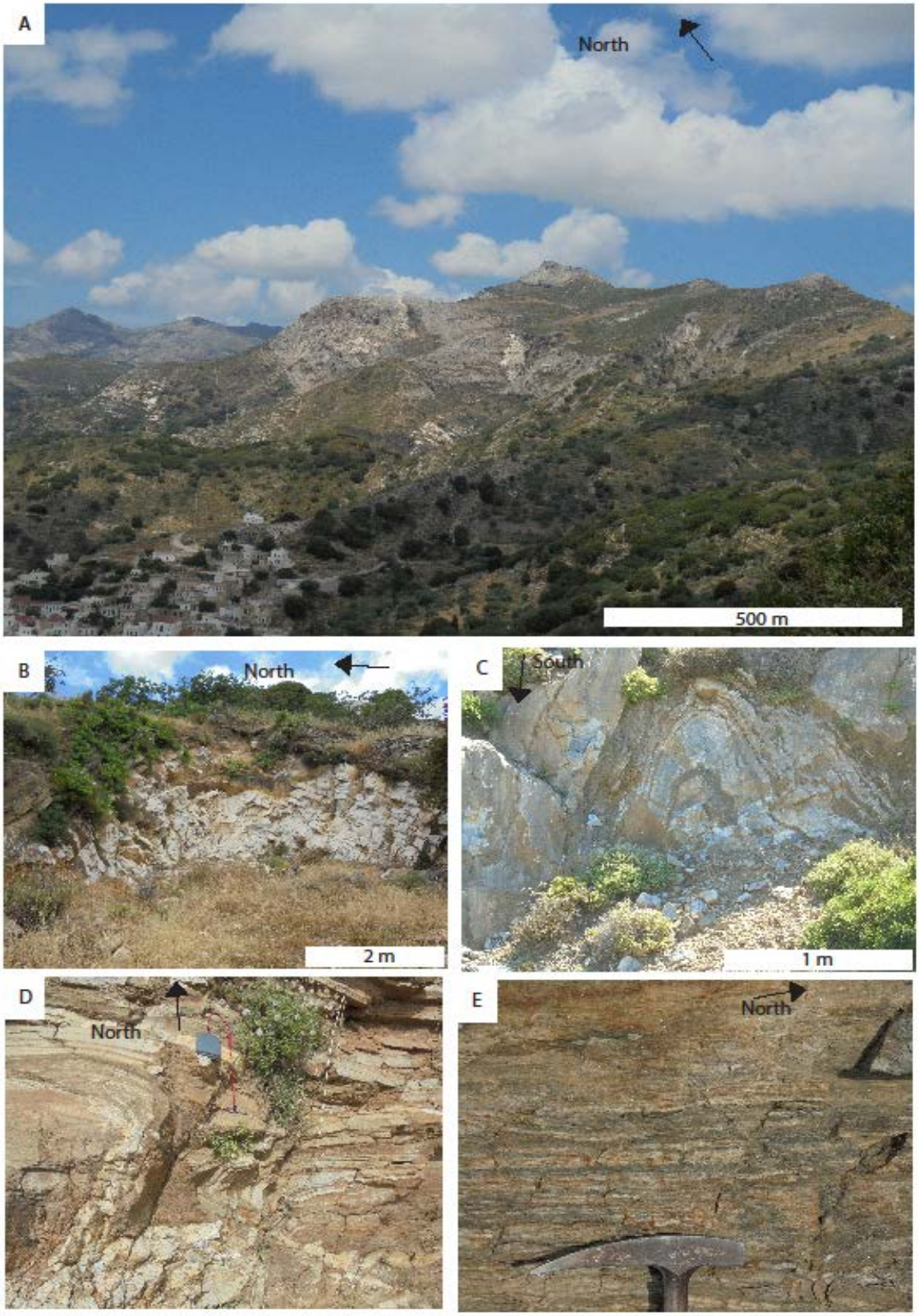

Figure 1.10: Koronos Unit outcrop photographs: A) Overview panorama over Filoti showing F1 and F2 isoclinal folding in marbles, note the tight isoclinal to the eastern side of image are recumbent N-S trending isoclinal folds plunging to the NNE. B) Open upright gentle F3 fold affecting marble band. C) Tight isoclinal upright F3 fold in dolomitic marble. D) F2 isoclinal meter scale folds affecting the limbs of larger scale folds. E) Koronos Shear Zone meta-sediment showing cm -scale localized boudinage of quartzo-feldspathic layers.

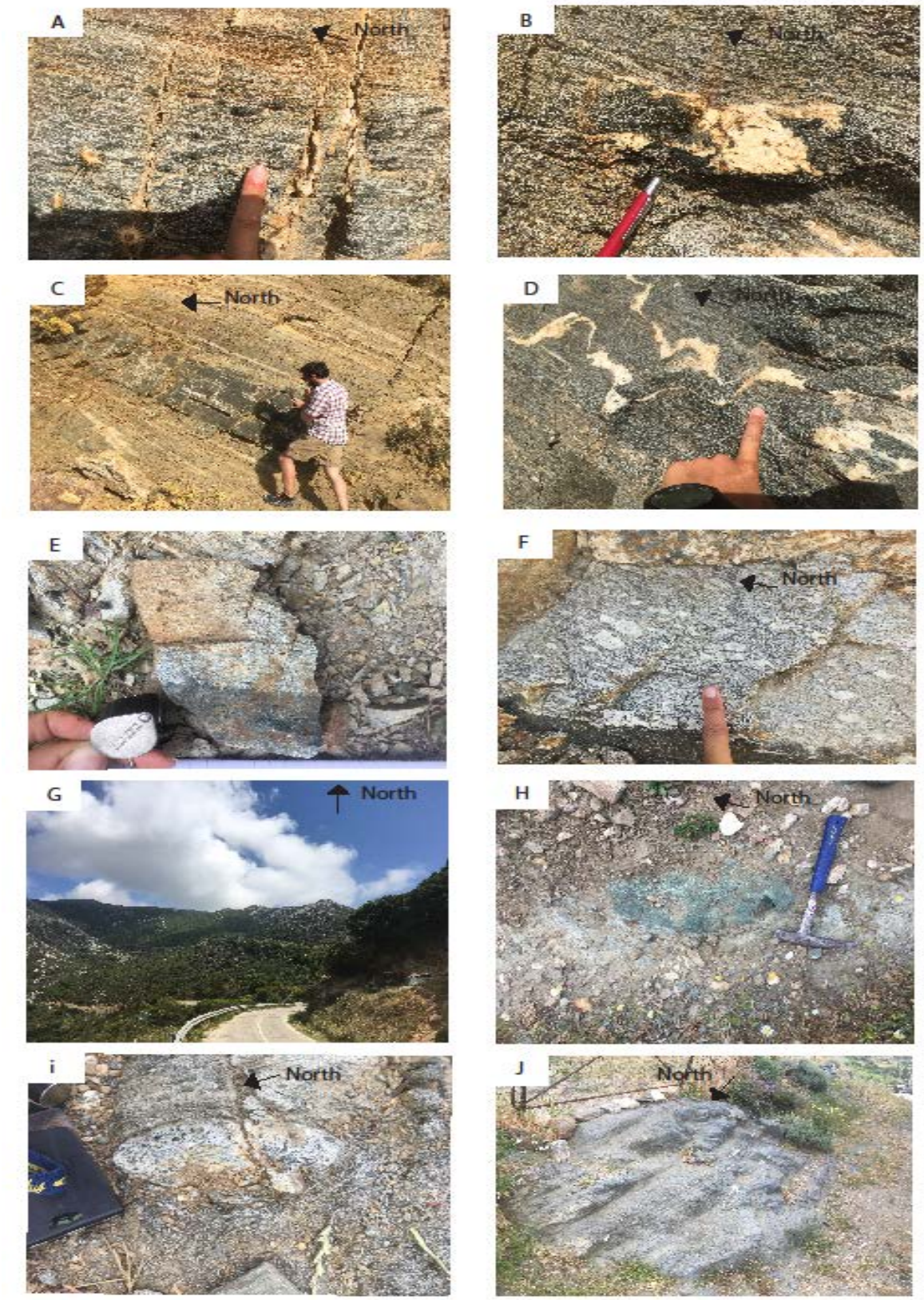

Figure 1.11: A) Amphibolite with ultramafic enclaves from just north of Mohni. B) The same amphibolite as A, but showing leucosomes. C) Amphibolite band parallel to the S0 foliation (bedding). D) Folded leucosomes within amphibolite from "The Main Ultramafic Horizon" E) Sample 17TL72 showing the transition between amphibolite and ultra-mafic lithologies, the ultramafics occur as enclaves within the amphibolites. F) Sheared orthogneiss basement of the KSZ showing top-to-NNE fabrics. G) Folding in Marbles bands just above the KSZ. H) Serpentinized ultra-mafic pod within host sheared amphibolite, within the KSZ. I) Completely serpentinized pod of ultramafic. J) Amphibolite horizon within the upper KSZ that hosts the ultramafics.

Cross-cutting Leucogranites

S-type leucogranites have emanating geometries from the migmatite dome and occur as sills or dykes no more than 5 m wide. On the eastern side of the dome, they cross-cut the Koronos shear zone and therefore post-date ductile top-to-NNE shearing. Whereas on the Western side of the core complex they rotate into alignment with the Naxos-Paros Detachment fault indicating they are pre-syn-tectonic with respect to extensional shearing. In the middle of the migmatite dome (Core high-strain zone) they intrude vertically along a N-S trending vertical plane and are boudinaged both vertically and horizontally N-S. These are dated by U–Pb zircon in Part 2.

Figure 1.12: Various cross-cutting leucogranite dykes. All leucogranites cross-cut the top to the NNE shearing on the Koronos Shear Zone but are all sheared into alignment with the Naxos-Paros Detachment System, indicating they post top-to-NNE shearing on KSZ but pre-date movement on the NPDS. Almost all have emanating geometries from the core migmatites suggesting they have been later folded with the doming migmatites.

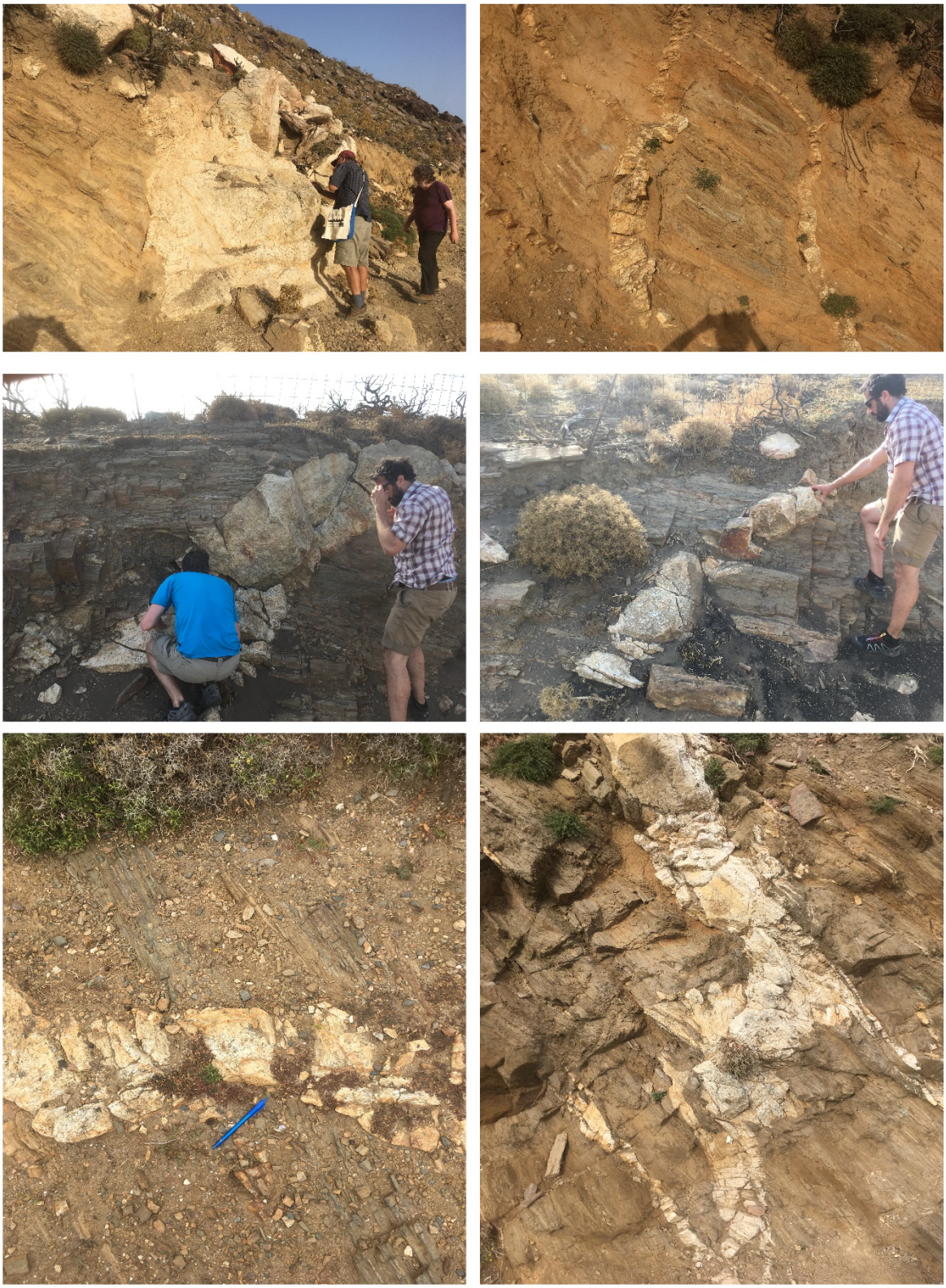

Figure 1.13: Various S-type cross-cutting granites emanating from the eastern margin of the migmatite dome clearly cross-cutting the S_3 top-to-NNE foliation.

Figure 1.14 More examples of S-type leucogranites cross-cutting the Koronos Shear Zone regional S_3 to-to-NNE shear fabric and foliation in the Koronos Unit, with either Garnet + Tourmaline or Biotite + Muscovite and always rooting from the Core Unit.

Upper Cycladic Nappe (Hangingwall)

Trench Melange (Silicified pillow basalts and radiolarian chert and exotic limestone)

Figure 1.15 Field photographs of Left) A silicified pillow basalt. Right) Silicified pillow basalt and radiolarian chert from the Upper Cycladic Nappe, author for scale (.

Naxos-Paros-Detachment System

On the western side of the metamorphic core complex, the NPDS truncates frozen in metamorphic stratigraphy to produce a metamorphic field gradient of 350-700 °C km^{-1}. Along this shear zone, leucogranites emanate from the core and rotate into alignment with the strong shearing foliation. The foliation is steeply dipping to the west with a sub-horizontal lineation trending NNE-SSW with top-to-NNE sense of shear. Brittle normal faulting is in abundance in the relatively-metamorphosed hanging wall and seem to root into a 25-50m cataclasite zone, marked by fault breccia and cataclasites that overprint ductile deformation. Repetition of orthogneiss basement lithologies with schist and marble derived from the continental shelf sequence suggest structural repetition by thrust faulting pre-dates and is reactivated by extension. The cross-section below illustrates these relationships.

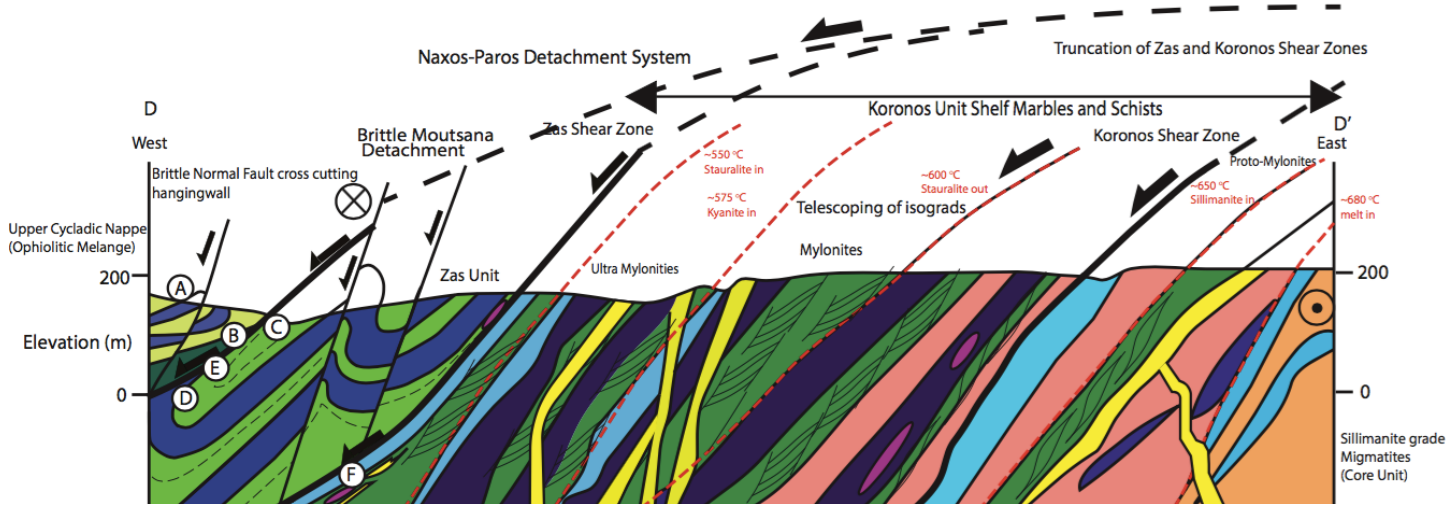

Figure 1.16 Cross-section through the Naxos Paros Detachment System on the western side of the core complex, note the telescoping of isograds suggesting the fault cross-cuts previously frozen in metamorphic stratigraphy, below zoomed in geological map of the central part of the Naxos metamorphic core complex

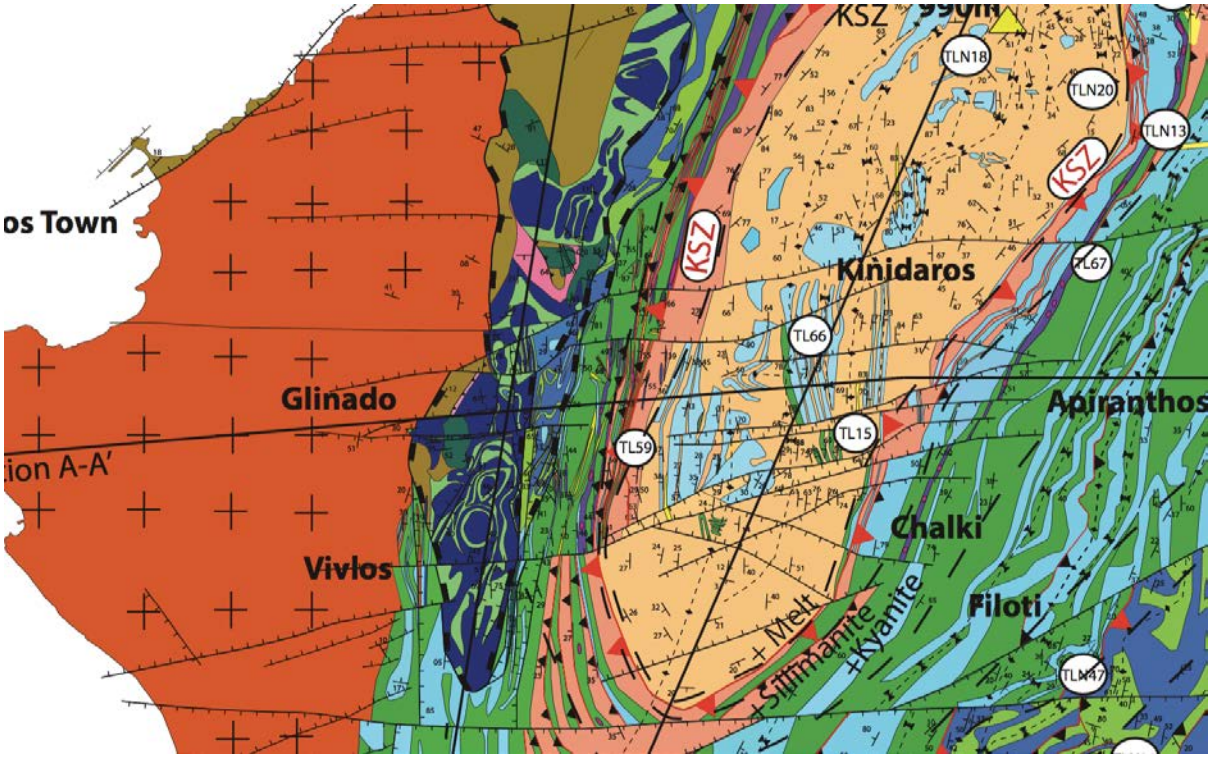

Detailed geological map of the western side of the migmatite dome illustrating the relationships with the NPDS, that cuts the metamorphic stratigraphy. Also note the repeated gneissic bands intercalated with schist which represent previous thick skinned thrusts responsible for the Barrovian metamorphism recorded on Naxos. The amphibolite horizon (marked in purple) with ultramafic enclaves is a semi-continuous horizon that envelops the structurally deepest level of the shelf carbonate meta-sedimentary sequence on the perimeter of the migmatite dome. ENE/WSW trending normal and strike slip faults transect the metamorphic footwall and offset some of the marble-gneiss horizons by up to a few hundred meters. The granite intrudes into the southern part of the island but has a sheared boundary along the NPDS on its northern contact. The Western side of the Granite is cut by a high angle fault near Naxos Town, with highly silicified sediments along this fault zone. Fluvial sediments near the port dip westward away from the island at ~20°, which is not expected for simply a normal sensed fault indicating some component of E-W shortening must accompany N-S extension.

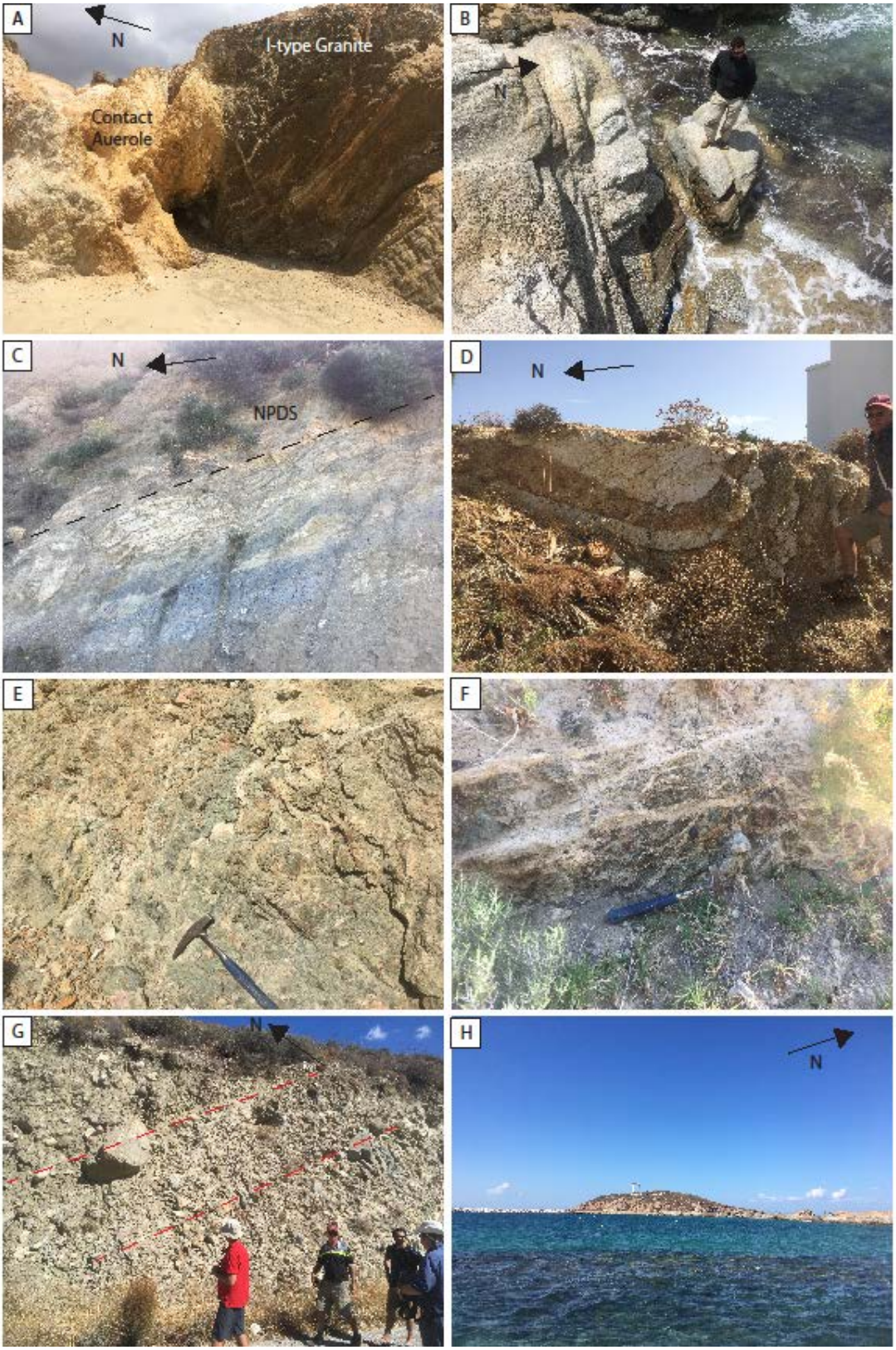

Figure 1.17: Various outcrop photographs of the I-type granite contact to the south of Mikra Vigla in Southern Naxos (N36.986285, E25.389467) (A and B) C) the NPDS brittle/ductile fault surface (N37.071497, E25.416252) D) (N37.074052, E25.399977) folded aplite sills within the I-type granite near Glinado E) Pillow basalts in the hangingwall of the NPDS (N37.097377, E25.433838). F) Fluvial conglomerate that overlies the basalts with clasts of ultra-mafic, and metamorphic clasts possibly derived from the footwall of Naxos MCC (N37.072059, E25.415357). F and G) Poorly sorted conglomerates and gravels dipping to the west, F) deposited on the western margin of the island unconformably laid on top of the trench mélange and pillow basalts of the upper Cycladic Nappe (N37.126076, E25.435650) and G) The peninsular with the temple of Apollo to the west of Naxos Town (N37.109553, E25.372366).

Core Unit migmatites and gneisses

The Core Unit represents intercalated continental margin metasediments and marbles with orthogneissic basement to the shelf sequence. The structural repetition of lithology indicates the Core Unit must comprise of a series of thick-skinned thrusts overthrusting and thickening the sequence. These contacts have been completely reworked by anatexis and folding during migmatite dome formation. Melt quantity varies in response to metamorphic grade and bulk composition, with meta-pelites locally having up-to 20-25% melt but orthogneiss and leucogneiss having very little evidence for melting during peak Barrovian conditions. Stromatic migmatites with peritectic K-feldspar can be seen at deep levels of the dome indicating the rocks crossed the muscovite dehydration reaction.

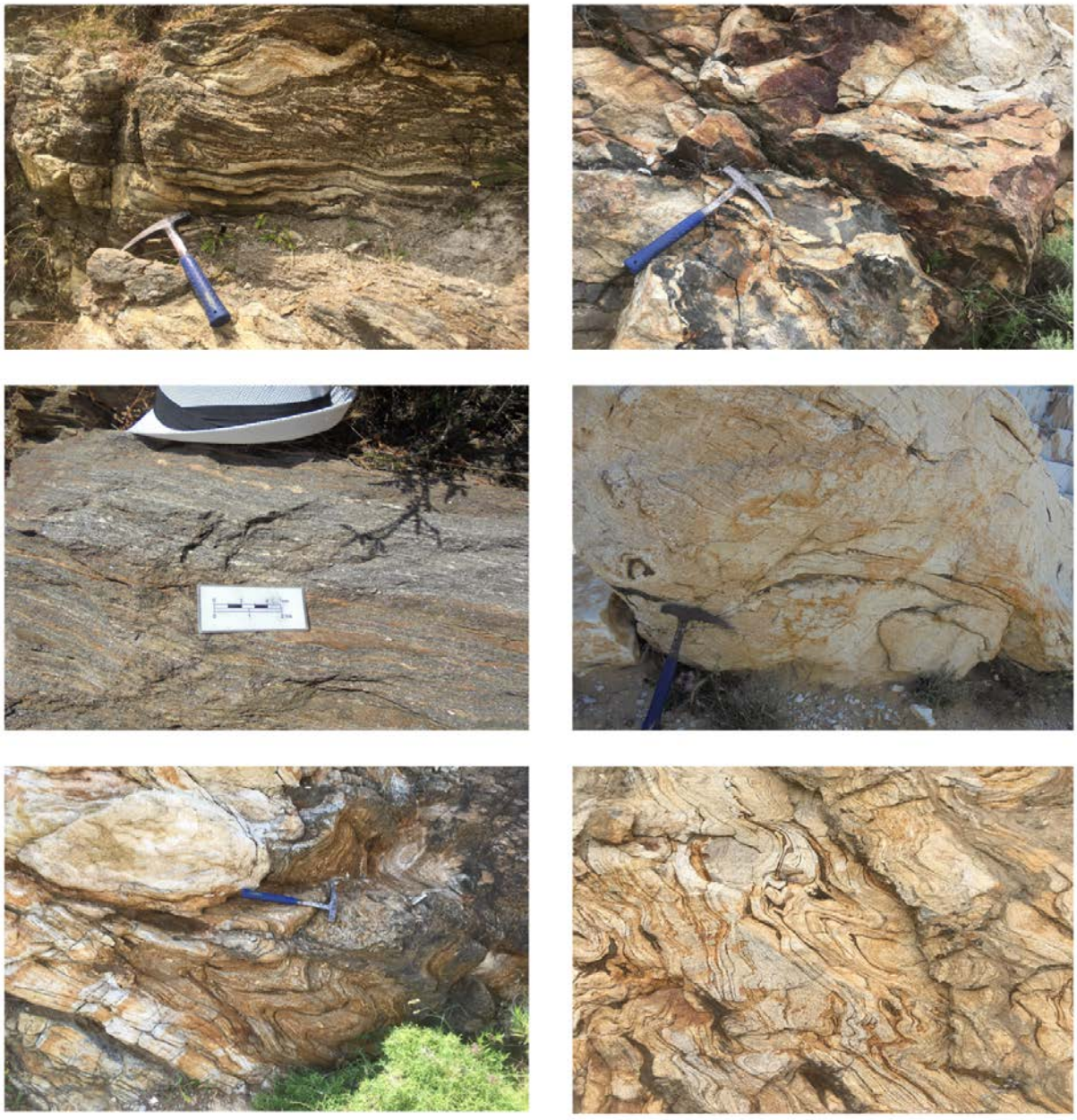

Figure 1.18 Outcrop photographs of a variety of migmatites and small-scale deformation structures from the Core Unit

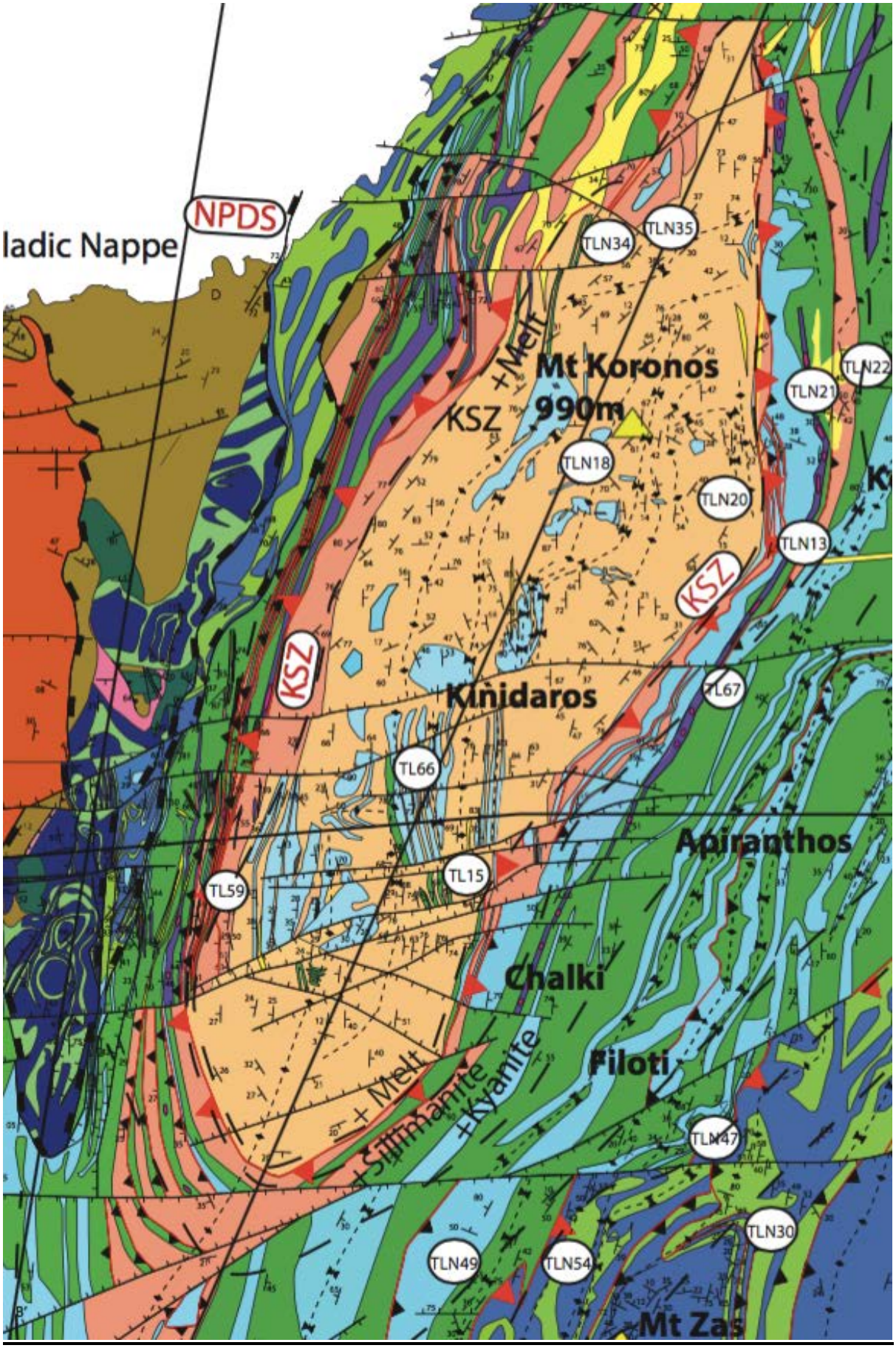

Figure 1.19 Geological map of the migmatite dome with location positions of key samples

Field and microstructural evidence from the migmatite dome and carapace suggest top-to-NNE shearing pre-dated migmatite doming, and the migmatite dome formed under horizontal constrictional strain at low pressure conditions (M_3) (5-6 kbar, 690-730 °C). We may expect the rotation of the principle stress axes to cause constriction, as E-W shortening become more dominant and this may become localised in partially molten crust and ductile. This may occur during the transition from compression to extension as shown overleaf.

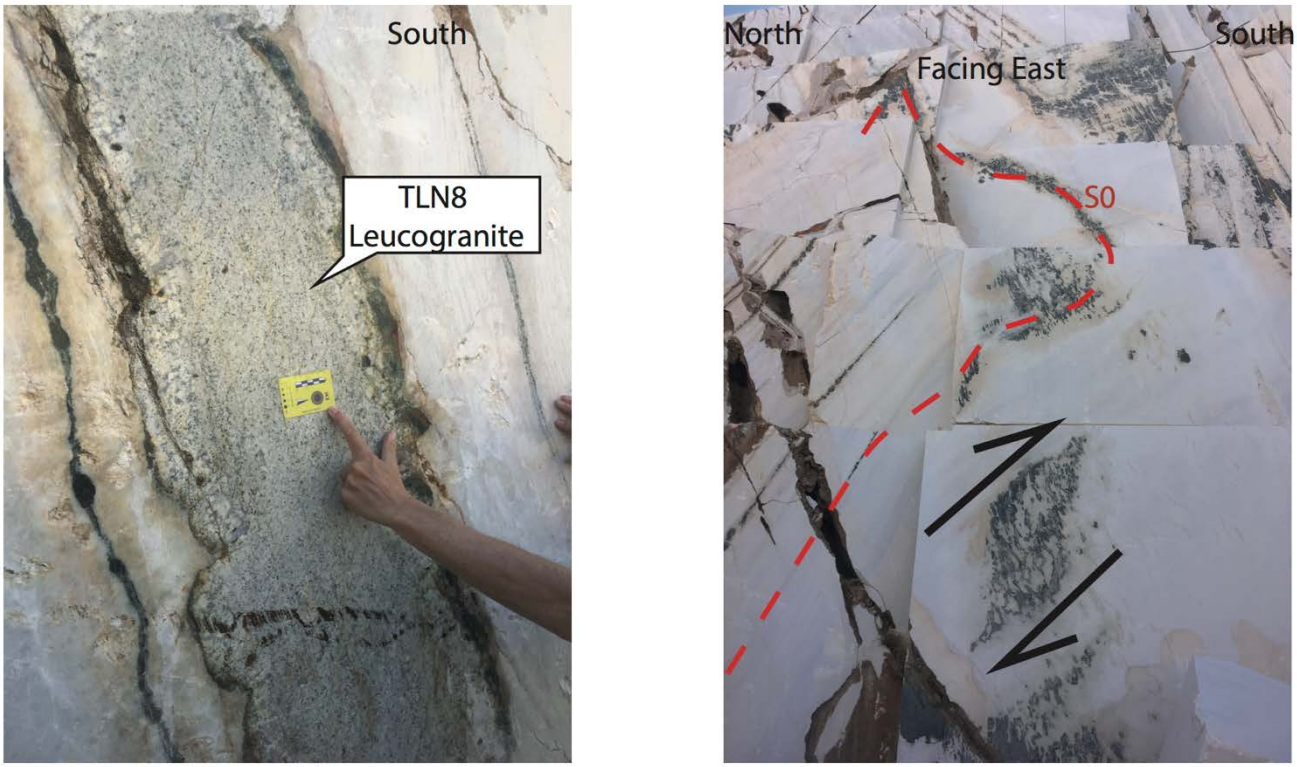

Figure 1.20 outcrop photos from the Core High Strain Zone. Left Deformed and vertically boudinaged leucogranite dyke with boudinaged amphibolite mafic sills that intruded the shelf marbles prior to deformation. Right Large scale upright east west trending isoclinal folding and top-to-south multi meter scale S-C fabric from the deformed amphibolites. S_0 is defined by the amphibolite horizons that represent the paleo horizontal.

Figure 1.21: A collection of outcrop photographs from the Kinadaros and Boulibas Quarries showing the isoclinal folding and spectacular boudinage overprint.

Figure 1.22: More outcrop photographs from the Kinidaros Quarry showing the 3-D folding geometry, boudinage and folding of S-type leucogranites (e.g. F&H).

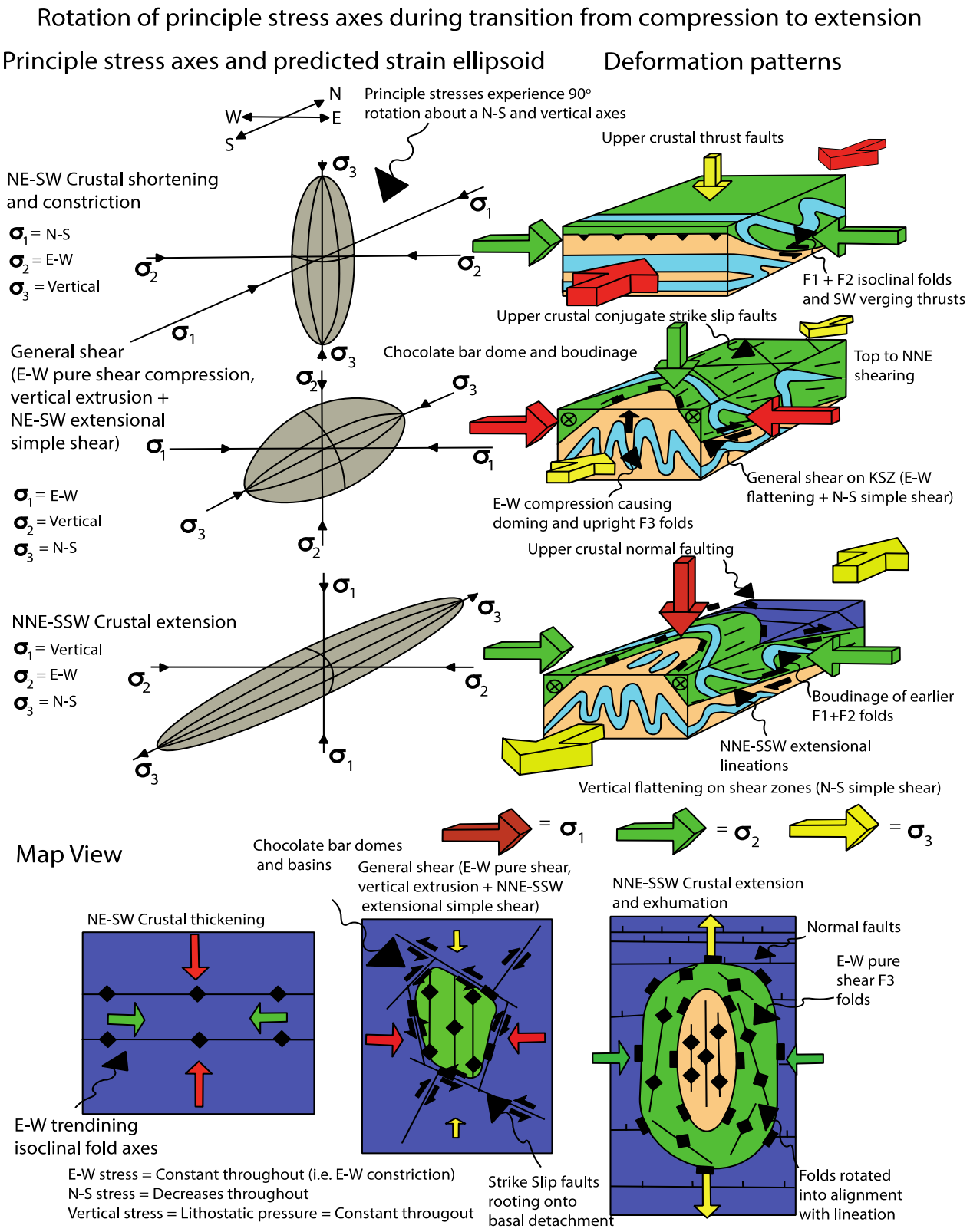

Figure 1.23: Cartoon model to illustrate the changing stress regime that may be expected to produce such structures. Decreasing N-S compressive stress causing a switch from horizontal constriction to NNE-SSW extension. During this transition, a strike slip stress regime would be created.

2. Key sample descriptions, and microstructure:

2.1 Zas Unit:

TLN54: (N37.036781 E25.493024)

TLN54 is a blueschist facies calc-schist that has been retrogressed in greeschist facies. It has an unusual bulk composition, presumably reflecting its meta-volcanic protolith with interstitial layers of carbonate. There are large glaucophane poryroblasts distributed throughout that record M_1 *HP-LT* phase, these are mainly aligned well with respect to S_3 shearing that deforms around them. Glaucophanes are also deformed in isoclinal folds, where they follow compositional horizons indicating folding happed post glaucophane growth and is therefore an exhumational structure. Clinozoisite grains are sometimes pseudomorphed by haematite and chlorite grows adjacent to glaucophane and is a common breakdown product. Relict S_2 fabric preserved in isoclinal folds and ghost crenulation cleavages defined by microlithons of muscovite which are re-deformed by a later greenschist facies S_3 extensional fabric that utilizes their cleavage domains. Clinozoisites are aligned with the S_3 foliation, indicating they are pre-syn-tectonic with respect to shearing. Lots of dynamic recrystallization in quartz with predominantly bulging grain boundaries, suggesting S_3 development in the greenschist facies. Chlorite is distributed mainly along the more sheared domains probably due to fluids on the shear zone during exhumation.

TLN26: (N36.935434 E25.475521)

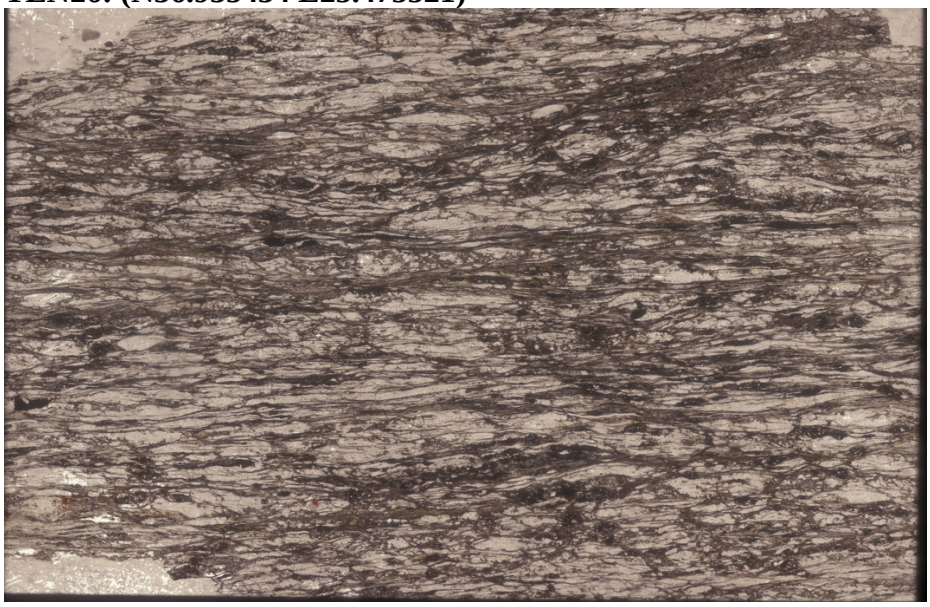

This rock was taken from Kalatados Bay in SE Naxos and represents an almost completely retrogressed mica schist associated with greenschist facies assemblages. There are domains of higher Si bearing mica that are phengitic in composition and rutile needles recording the earlier M_1 *HP-LT* blueschist facies event, however there is a lack of other diagnostic minerals associated with blueschist conditions. There is a range of dynamic recrystallization textures both subgrain rotation in quartz and also bulging microstructures indicative of deformation temperatures between 280-450 °C.

TLN30: (N37.098329 E25.557419)

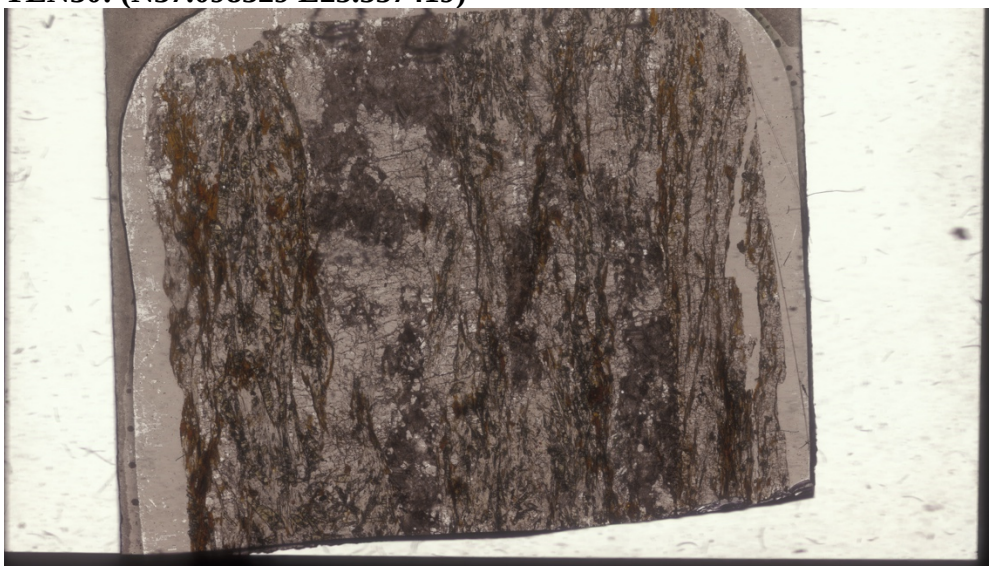

A multi domain rock, carbonate rich domains, and more pelitic domains, that preserves evidence for experiencing M_1 high-pressure conditions. There are lots of clinozoiste in the more pelitic domains that are strongly lineated and appear syntectonic with respect to the matrix fabric (S_3) associated with top-to-NNE shearing and these inter-grown with biotite, muscovite and quartz. Some clinozoisites show post-tectonic relationships with respect to the S_3 shearing fabric, as indicated by ilmanite inclusion trails in micaceous zones and commonly appears to grow after biotite, presumably at greenschist facies conditions. There are allanites within the cores of clinozoisite that

are used as a target for U–Pb dating. Because there is no evidence for thermal overprinting on this high-pressure relict assemlage, the resultant ages will provide a minimum age constraint for peak M_1 conditions.

TLN25: (N36.999229 E25.486564)

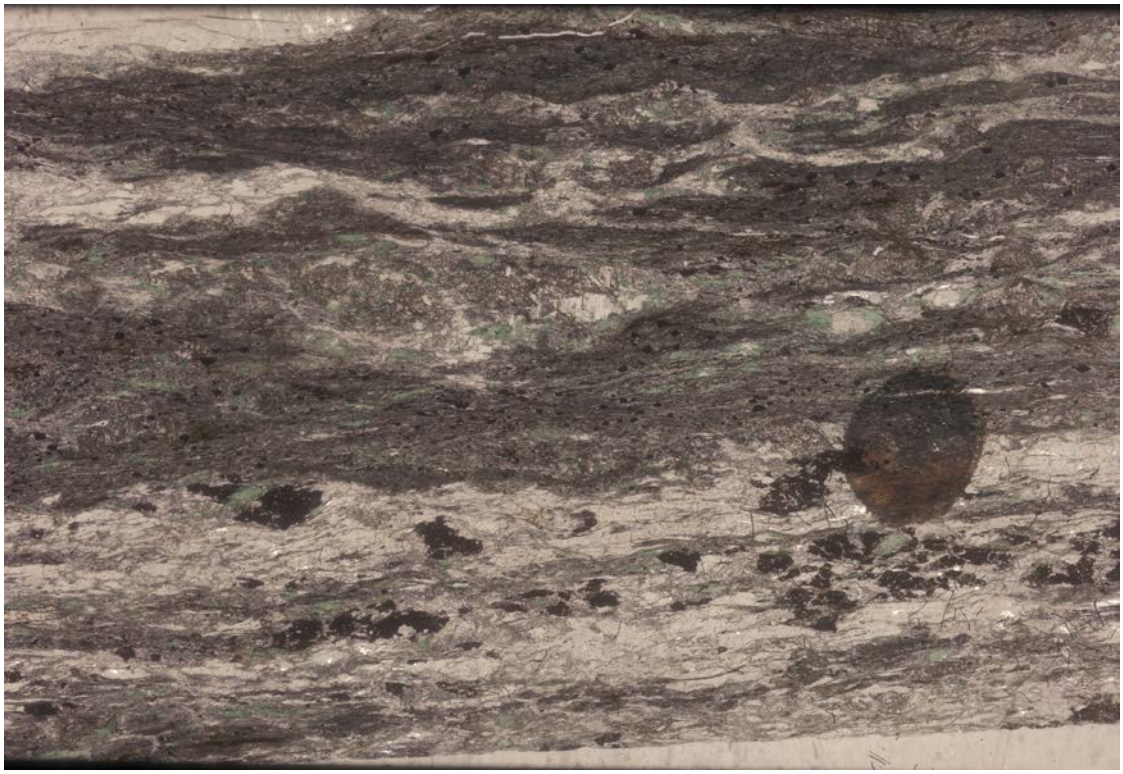

A calc-schist, preserving 3 major fabrics recording the transition from blueschist facies conditions to greenschist retrogression. The matrix is dominated by fine intergrowths of chlorite + actinolite, large epidote porphyroblasts that entrain glaucophane and paragonite inclusions (S_1), that are aligned with the mylonitic S_3 foliation but also show evidence for a folded asymmetric foliation (S_1) that formed at blueschist facies conditions. Clinozoisite is post-tectonic with respect to the foliation recorded by glaucophane (S_1) and in many places shows helical inclusion trails of a later crenulation cleavage (S_2). Epidotes are also post tectonic with respect to the S_2 foliation in deformed amphiboles and muscovite in the matrix. S_2 folds have axial planes parallel to the S_3 foliation that preserves top-to-NNE shearing in greenschist facies minerals.

Zas Unit Mineral Proportions:

Sample	Gln	Prg	Phg	Rt	Plag	Act	Chl	Bt	Ep	Czo	Talc	Cal	Qtz
TLN54	12%	2%	19%	5%	20%	0%	15%	1%	9%	0%	0%	4%	15%
TLN25	2%	1%	12%	0.5%	5%	16%	11%	10%	5%	0%	5%	3%	2%
TLN26	0%	2%	33%	1%	7%	0%	13%	2%	6	2%	0%	4%	20%
TLN30	0%	0%	9%	1%	12%	0%	8%	3%	14	23%	0%	6%	10%

2.2 Koronos Unit:

TLN47:
A deformed and sheared calc-schist was taken from the periphery of the Zas Shear Zone showing great evidence for early S_2 crenulation cleavages overprinted by S_3 shearing foliation in the lower amphibolite-greenschist facies. S_2 is preserved in post tectonic plagioclase (albite) porphyroclasts that also overgrow the sheared S3 foliation. Epidote is commonly found breaking down to muscovite + albite associated with greencshist facies retrogression. There are high degrees of static recrystallization, with annealing in quartz indicating high temperatures outlasted deformation in the epidote amphibolite-greenschist facies.

TLN49: (N37.04549 E25.50794)
This sample is a calc-schist with a lower amphibolite facies metamorphic assemblage. It preserves a very strong crenulation cleavage (S_2) or with well-developed microlithos and cleavage domains, this has been overprinted by a top-to-NE extensional fabric that utilizes cleavage domain fabrics, that are parallel to S_3. S_3 is a crosscutting shearing fabric, superimposed on the limbs of extremely tight folds, indicating top to the left sinstral S-C mica fish, that is opposite to the vergence direction to the folds. Compositionl banding is isoclinally folded on cm scale with parismtic folds. Quartz shows bulging grain boundries, indicating dynamic recrystallization in the greenschist facies, with quite a significant component of static recrystallization and annealing. Some paragonite and clinozoisite are trapped as inclusions within the muscovite, and are sometimes aligned with the foliation (S_3) but sometimes not.

TLN21: (N37.125787 E25.518516)

A garnet, kyanite, sillimanite gneiss taken from the northeastern margin of the migmatite dome very close to the base of the Koronos Shear Zone**.** It forms the basal schists just structurally overlying a slither of basement that has been overthrust onto

more shelf carbonate material**.** High temperature deformation fabric in Quartz at peak conditions, with a strong amount of annealing, indicating high temperatures outlasted deformation, also indicated by a desscuate texture of some late secondary muscovites and biotites. Kyanite transition to sillimanite by a Carmicheal reaction scheme, sillimanite biotite knots whereas kyanite is associated with quartz, muscovite horizons. Garnet breaking down to biotite. Late low temperature fractures and joints (300-400 °C) cross cuts everything. There is evidence for a continuum of deformation down to lower temperatures associated with bulging and sub-grain rotation within quartz. There is low temperature brittle fractures and deformation overprinting all fabrics through the matrix. Late biotite growing off garnet, due to garnet breakdown. Also most of the deformation appears concentrated within the quartz rich bands, with abundant deformation recrystallization textures overprinted by static recrystallization. The biotite, sillimanite intergrowths appear to grow within dilational strain sites and presumably formed during the close of deformation at peak conditions associated with decompression.

TLN22: (N37.127084 E25.524576)

There are lots of small ~ 100-300 μm garnets that are syn-post tectonic with respect to the surrounding matrix fabric. The quanity of garnets and their size suggests high reaction overstep was achieved during garnet growth. They commonly overgrow biotite folia, and have lots of fluid inclusions, with a mixture of both CO_2 represented by dark fluid inclusions and H_2O. Kyanite porphyroblasts are commonly found breaking down to biotite, and also muscovite and quartz and plagioclase clusters. Some small garnets are even trapped within a kyanite, indicating kyanite growth during and following garnet growth. Kyanite grows within domains unaffected by the exterior matrix fabric and deformation indicating this exterior fabric S_3 is syn-post-kyanite grade conditions. Top-to-NNE S-C' shear fabrics (S_3) affect the matrix and are diagnosed by asymmetry and stair stepping around enclaves of garnet, biotite and kyanite. High relief apatite crystals throughout that look like garnet but not isotropic. Not very much muscovite either. Deformation appears to be concentrated within the biotite rich folia, bands of coarsely annealed quartz. Quartz deforming mainly by sub-grain rotation but also some evidence for grain boundary migration and even bulging indicating a range of temperatures during deformation.

TLN16: (N37.100794 E25.515643)

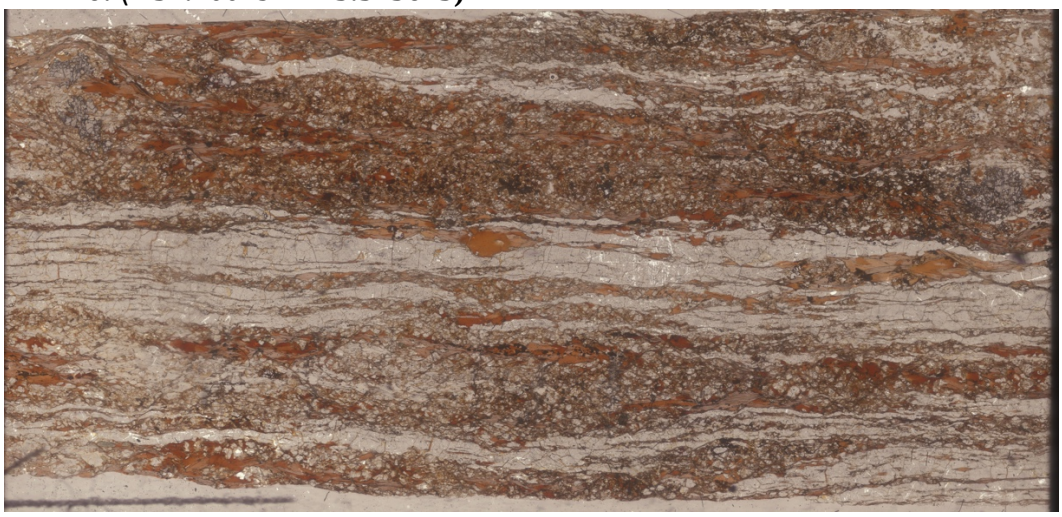

A highly strained garnet biotite gneiss, without any aluminium silicates. Garnet is intergrown with biotite rich domains, there is a high degree of dynamic recrystallization within the quartz rich domains, evident as grain boundary migration. Late C' shear bands cutting through define S_3 and are indicating top-to-right (NNE) shearing. Garnets trap earlier S_2 foliation sub-parallel to the current foliation and S_3 is only slightly developed but marked by biotites deforming around the garnets. Some K-feldspar grains with fabric wrapping around them in places, and muscovites are primary and not replaced by kyanite or vice versa. Large grains of rutile and sphene aligned parallel to S2 indicating they formed prior to S_2 development at high pressure. We relate S_2 with overthrusting of the Cycladic Blueschists over the un-subducted more proximal shelf sequence. There could be some potential high relief grain that could be kyanite that is breaking down to biotite aligned parallel to S_2 although unclear. Big garnets are pre-tectonic and wrapped by S_3 top-to-NNE shear fabric.

TLN13: (N37.107362 E25.481318)

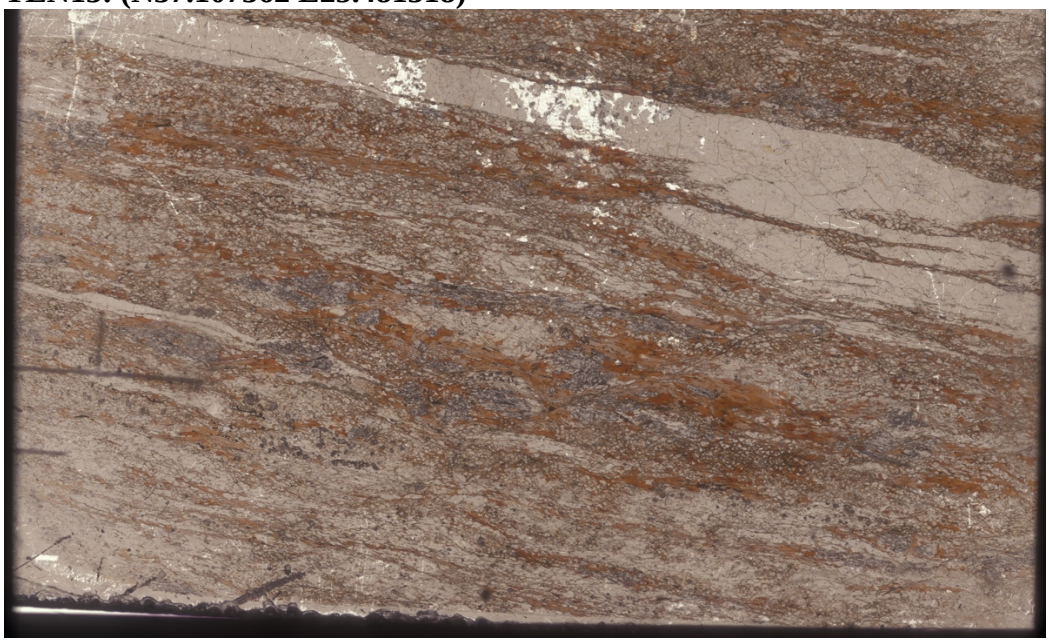

A garnet kyanite gneiss. Kyanite, poikioblasts breaking down to biotite which include rutile grains. Kyanite also got garnet inclusions, however these garnets look like they overgrow kyanite forming in fractures. Garnet appears to overgrow everything except

kyanite and they have lots of small fluid inclusions, both dark and clear indicating a mixed fluid of H_2O/CO_2. Kyanite is therefore pre-kinematic with respect to deformation, whereas garnet appears post tectonic with-respect-to shearing. Grain boundary migration acting in qtz rich horizons indicating high temperatures during shearing. Plagioclase and biotite rich domains, probably volcaniclastic in origin. There is not much Muscovite probably due to dehydration reactions. quartz rich domains intensely annealed with static recrystallization. Indicating shearing and development of S_2 at peak/ just prior to peak followed by thermal relaxation producing small garnets to nucleate. S_3 is top-to-NNE S-C' blasto-mylonite fabric with C' planes that cross-cut biotite and kyanite folia, which progress to brittle deformation. Biotite and chlorite inclusions within the kyanite grains. There is some potential stauralite trapped within kyanite (kyanite possibly pseudomorphing staurolite) indicated by yellow pleochroism. kyanite commonly in small biotite + plagioclase enclaves that behave more rigidly and are deformed by the shearing post kyanite growth, and some evidence for constrictional strain and shearing during kyanite growth, indicated by rotation of kyanite porphyroblasts into alignment with the lineation. There is a messy domain with small poikioblasts of staurolite, that all go into extinction at once, and therefore possibly represent a large relict staurolite poikioblast. This entrains a folded (S_{2a}) fabric defined by muscovite but has been wrapped by biotite indicating it is pre-tectonic with respect to the shearing.

TL67 (N37.088171, E25.498871):

This sample is a textbook high grade blasto-mylonite from the top of the Koronos Shear Zone directly above the migmatite dome. This rock contains enclaves of peak M_2 kyanite grade fabrics (S_2) which are wrapped by a later top-to-NNE extensional fabric (S_3). Grt occurs within enclaves and within the deformed matrix and is definitely pre tectonic with respect to the sheared matrix (S_3). Deformation microstructures suggest both grain boundary migration and dynamic recrystallization were the dominant deformation mechanisms, characteristic of deformation temperatures in excess of 600 °C. There is evidence for static recrystallization of quartz and high temperature annealing structures, which appear synchronous with peak conditions, indicating high temperatures outlasted deformation. Top-to-NNE S-C' S_3 fabric is later cut by brittle

deformation and prominent cross-cutting C' planes. Garnet growth history: Core grows syn-tectonic with S_2 parallel fabric and sometimes preserves an internal S_1 fabric oblique to S_2. Grt rim grows post S_2 foliation defined by kyanite and rutile in enclaves, and garnet has straight faces crosscutting biotite and kyanite folia. Kyanite grew pre-syn S_2 and is aligned with biotite and associated with muscovite, in some domains it breaking down to muscovite, plagioclase and biotite. S_3 cross-cuts everything with only lower temperature deformation affecting it. Indicates high pressures then thermal metamorphism at and following peak as garnet growing cross-cutting kyanite, indicating high temperatures outlasting deformation.

17TL75 (N37.126075, E25.517581):
A garnet amphibolite from what has been described previously as the "Main Ultramafic Unit" on the Koronos ridge within the Koronos Shear Zone that hosts the small enclaves of ultramafic compositions. The main assemblage contains amphibole, plagioclase with garnet, and ilmenite with minor titanite and chlorite retrograde breakdown products. The main fabric is shown by preferential alignment of amphibole that defines the S_{2b} fabric coarsened. There is a small degree of melting shown by undulating grain boundaries of plagioclase and quartz, and can be seen in hand specimen a mm-scale leucosomes aligned with the fabric. The microstructure appears to just preserve peak M_2 conditions with no evidence for any earlier or relict assemblages.

17TL110 (N37.104557, E25.546289):
A kyanite mica schist taken from the rocks surrounding the Emery (Corundum) as horizons within marbles within the Koronos Unit. Kyanite is aligned with and overgrows the crenulations (S_{2a}) whereas muscovite is isoclinally folded with the crenulation cleavage (S_{2a}). There are no obvious S_3 top-to-NNE shear fabrics, possibly because the sample was collected from an enclave from within a course dolomitic marble band and is away from the Koronos and Zas Shear Zones. We therefore interpret this microstructure to reflect prograde-peak M_2 kyanite grade upper amphibolite facies conditions.

Koronos Unit Mineral Proportions

Sample	Grt	Ky	Sill	Bt	Ms	Rt	Ilm	Plag	Kfs	Qtz
TLN13	8%	10%	1%	18%	12%	1%	0.5%	22%	0%	27.5%
TLN16	4%	0%	0%	20%	0%	0.5%	0.5%	32%	0%	40%
TLN21	8%	7%	5%	18%	16%	0.5%	1%	20%	1.5%	23%
TLN22	7.5%	8.5%	0%	18%	10%	0.5%	0.5%	22%	0%	33%
TLN47	0%	0%	0%	12%	33%	1%	1%	18%	0%	35%
TLN49	0%	1%	0%	13%	36%	2%	1%	25%	0%	22%
TL67	10.2%	7.5%	0.1%	17.5%	12.0%	0.6%	0.3%	20.3%	5.3%	26.2%

2.3 Core Unit:

TL15: (N37.08022 E25.47802)

A garnet, kyanite migmatite that has experienced small degrees of partial melting. There is no sillimanite in this sample but lots of secondary muscovite which could suggest the melt didn't escape and melt maintained equilibrium with the reactants, and that secondary muscovite formed by the back reaction. The garnets have inclusions of plagioclase + quartz + muscovite and biotite appears to be growing of garnet and kyanite. Some of the garnets have their cores partially destroyed, creating atoll structures. The garnets and kyanites are also found in distinct layer horizons within the rock, presumably corresponding to the primary compositional layering (S_0). Between these aluminium-rich horizons the matrix consists of dominantly quartz and plagioclase, that appears to have experienced anatexis by the very round and irregular quartz grains, suggesting remobilization. and high temperature grain boundary migration deformation is mostly occurring. Biotites are very Ti rich but with a descuate fabric suggesting internal deformation with a slight cpo parallel with the stretching lineation.

TL66: (N37.08880 E25.47022)

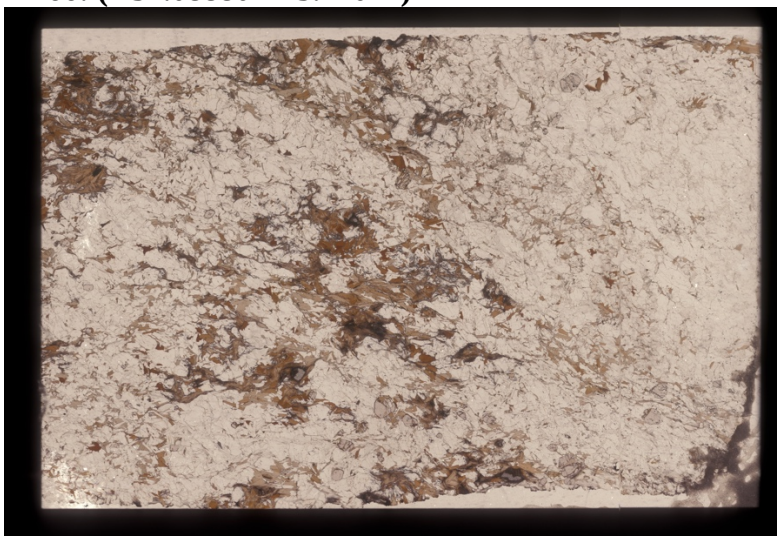

This is a sillimanite garnet migmatite that preserves evidence for having experienced both hydrous melting and (incomplete) muscovite dehydration melting. There are very late secondary muscovites that pseudomorph K-feldspar and kyanite relics, any preserved (minimal) are breaking down in contact with biotite and surrounded by plagioclase, quartz and muscovite. The secondary muscovites also preserve little inclusions of kyanite relicts. Garnets also trap inclusions of plagioclase, quartz and biotite. Zones of melt accumulation are distinguished by rounded grain boundaries of qtz. Leucosomes comprise of plagioclase + quartz, mesosomes comprise of biotite + muscovite + sillimanite, S_1 = biotite + muscovite + kyanite + garnet, S_2 = biotite + muscovite + garnet + biotite + sillimanite. Sillimanite is associated in regions with quartz and biotite creating knots of "faserkiesel", which is interpreted to preserve the back reaction of the muscovite dehydration melting reaction, producing the secondary muscovites at the expense of K-feldspar and kyanite in this back reaction. These microstructural features suggest melt remained in communication with the rock during anatexis.

TL59: (N37.06824 E25.44170)

A biotite gneiss, taken from an aluminium horizon near first appearance of melt at the base of the Koronos Shear Zone. This preserves some microstructural evidence for having experienced some degrees of melting but is very miniumal and can only be inferred from grain boundary coarsening. There are no Al-silicates, in this rock and kyanite has been replaced by secondary muscovite, and not transformed into sillimanite, there is abundant secondary muscovite, after melting. There is not much evidence for earlier fabrics in this sample Garnets have strong reaction coronas in contact with the secondary muscovites There is a strong fabric orientation with a disjunctive relict crenulation cleavage (S_2) that has been recrystallized by later shearing (S_3). S_3 is defined by a very slight S-C' extensional shear fabric developed particularly in micaceous domains indicating top-to-NNE sense of shear.

TLN2A: N37.059982 E25.455638

A kyanite migmatite. Garnets are fairly small with fluid inclusions, mainly near the cores, and are showing zoning patterns in thin section, with some dark inclusions indicating a mixed fluid (H_2O/CO_2). Kyanite grains distributed throughout with a general alignment with the foliation. Very coarse muscovites intergrown with the kyanites, but kyanite overgrows biotite in the folia, muscovites are secondary and trap inclusions of monazite, zircon and other accessory minerals. Garnets are syn-post tectonic with respect to the foliation of biotite and muscovite and appear to show top to the right kinematic indicators and secondary muscovites overgrow everything. There is some peritectic K-feldspar, that overgrows plagioclase grains and primary muscovite.

TLN18: (N37.124483 E25.495319)

A diatexite migmatite with a heterogeneous fabric completely destroyed by partial melting process. There are abundant melting features and no primary muscovite remaining, indicating the rock experienced muscovite dehydration melting. There are still wispy schileren of biotites preserved marking the deformed foliation.

TLN20A: (N37.126904 E25.499998)

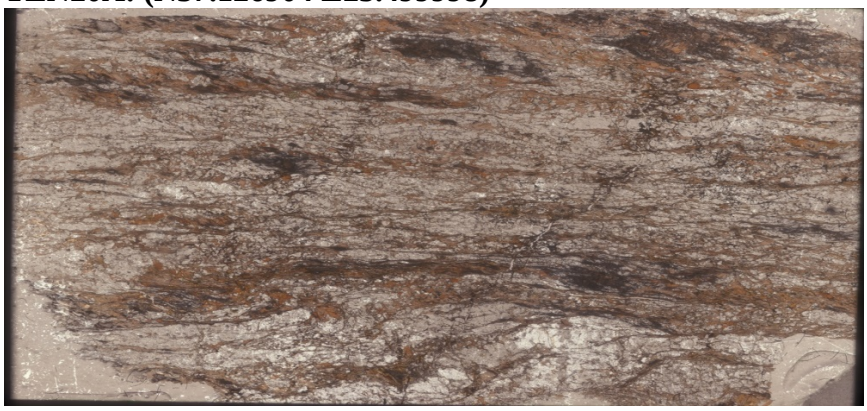

Lots of evidence for muscovite dehydration melting in the sillimanite field, consuming all muscovite as none left at all. Sillimanite, biotite intergrowths are folded and crenulated along an axis parallel to the stretching lineation (biotite-sillimanite intergrowths preserving the S_2 crenulation fabric). These are sometimes associated with peritectic K-feldspar. Late S_3 S-C' top to the right shear fabric slightly developed especially within the quartzo-feldspathic domains, Lower temperature strain dynamic recrystallization textures in quartz i.e. sub-grain rotation and bulging grain boundaries. Deformation is accommodated along the biotite folia and not zones of melting.

TLN34: (N37.16236 E25.50238)

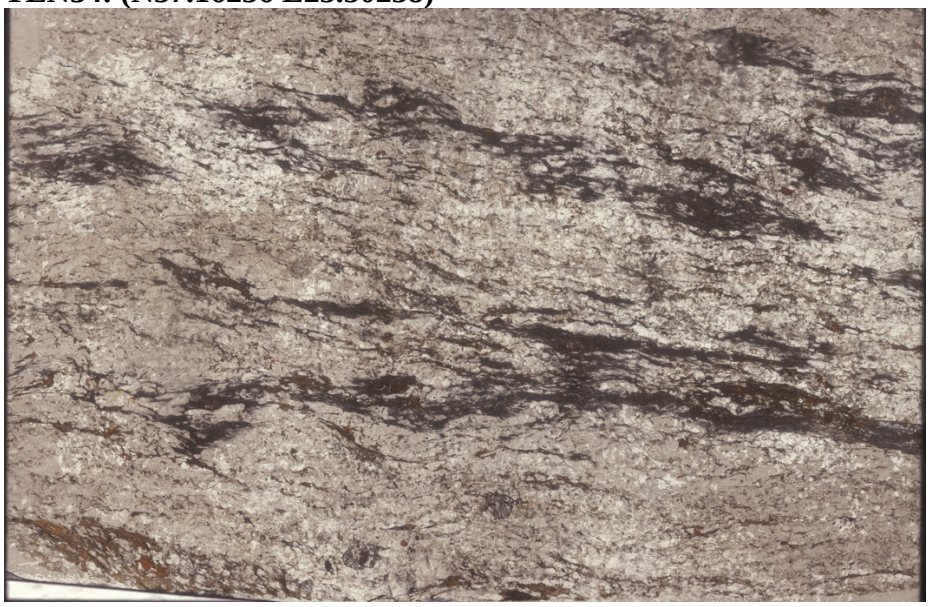

A sillimanite grade migmatite experienced muscovite dehydration melting, all muscovite has been consumed, sillimanite is fibrous but also prismatic and intergrown at sheaths within biotite, only quartz rich layers left and some of the biotite appears late. K-feldspar appears to overgrow plagioclase with numerous inclusions within it. Garnet has started to breakdown to biotite, and has some fluid rich inclusions. Most of the deformation appears to be concentrated within the sillimanite and biotite folia. Top-to-NNE shearing (S_3) is defined by biotite-sillimanite intergrowths, and is isoclinally folded tightly with fold axial cleavage sub-parallel to the lineation, indicating constriction perpendicular to the lineation at high grade.

TLN35: (N37.16228 E25.50452)

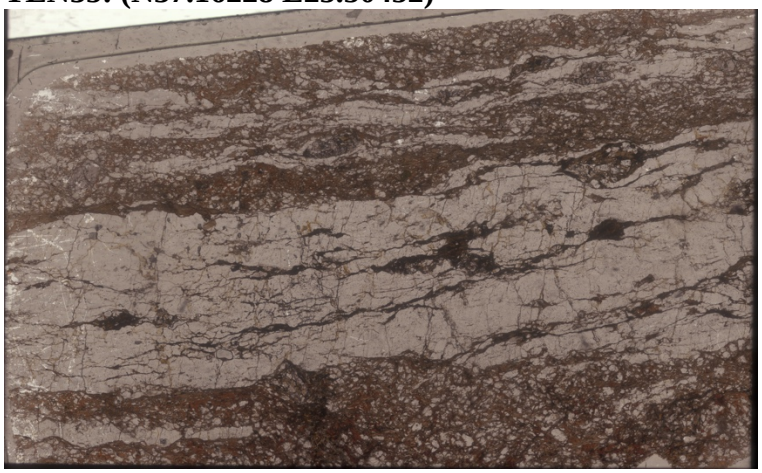

A sillimanite bearing migmatite that has experienced the muscovite dehydration melting reaction, characterized by distinct leucosomes and melanosomes. Melanosomes consist of peritectic sillimanite + biotite + plagioclase intergrowths, with some smaller garnets. Leucosomes dominantly quartzo-felspathic with some biotite folia and minor garnet. Garnets distributed in the leucosomes and are associated with some sillimanite and biotite. Coarse biotite and plagioclase intergrown and appear to pseudomorph a large porphyroblast potentially kyanite by the Carmicheal reaction scheme of kyanite to silliamite. There are domains of quartzo-felspathic material characterised by with high temperature grain boundary diffusion textures in quartz and undulose extinction in feldspar wrapping around the garnets. Quartz shows checker

board extinction and grain boundary migration textures exclusively indicating deformation at >650 °C. Garnets appear to show elongate geometries and sometimes show sun-tectonic almost snowball shapes that indicate garnet rotation during growth, however they have a post-tectonic rim that overgrows matrix elements, with asymmetry truncated around the core region that shows top to the left (south) sinstral shearing. However other shearing senses around smaller grains show top to the right fabrics. No muscovite is left, indicating it must have all been consumed during the partial melting process and probably crossed the muscovite dehydration melting in the sillimanite field. Resorption of some of the garnet, breaking down to plagioclase + biotite is not associated with shearing, indicating shearing must have occurred prior to garnet breakdown. There is only minor sillimanite intergrown with biotite, not really showing much foliation/ fabric. S_3 extensional fabric cross-cuts everything, indicating top to the right (north) shearing. Preservation of S_{2a} very tight fold defined by muddy, aluminium rich biotite layer. Sigma type porphroblasts/ boudins indicate conclusively top to the right shearing, with garnet porphyroblasts pre-tectonic with respect to the shearing.

Core Unit Mineral Proportions:

Sample	Grt	Ky	Sill	Bt	Ms	Rt	ilm	Plag	Kfs	Qtz
TLN2A	3.6%	3%	0%	11%	15%	0.6%	0.8%	27%	0%	31%
TL15	4.5%	4.5%	0%	18.5%	16%	0%	0.5%	31%	0%	25%
TL59	3.3%	0%	0%	12.3%	26.6%	0.9%	1.0%	24.5%	0%	31.4%
TL66	1.6%	0.6%	7.6%	18.2%	24.1%	0%	0.6%	21.2%	0.1%	26%
TLN18	0%	0%	0%	22%	1%	0%	1%	34%	4%	38%
TLN20A	0%	0%	3%	18%	1%	0%	1%	30%	15%	33%
TLN34	1.5%	0%	5%	20%	1%	0%	0.5%	26%	13%	34%
TLN35	2%	0%	2%	17%	0.5%	0%	0.5%	35%	0%	43%

3. Petrography and mineral chemistry:

3.1 Analytical Methods:

Compositional analyses were performed on a Cameca FX5-Fe electron microprobe with a tungsten tipped field emission gun at the Department of Earth Sciences, University of Oxford. Operating conditions involved an accelerating voltage of 15.0 keV corresponding to a current of 9 nA, a range of primary and secondary standards were used including andradite (Fe, Mg, Ca) TiO2, Mn metal, labradorite (Na, Al, Si) and sanidine (K) for major elements and synthetic standards for REE's. Garnet line profiles were collected using a consistent 10-micron step size across all garnets corresponding to between 100 and 200 analyses. High resolution garnet maps were acquired using a setup with a 15 keV accelerating voltage with a step size of 2 microns and a dwell time of 60 s.

Additional analyses were collected on a JEOL JS-840A scanning electron microscope (SEM) equipped with an Oxford Instruments Isis 300 energy-dispersive analytical system, and a LEO 535VP SEM equipped with an Oxford instruments Inca EDS system. Operating conditions comprised of a working distance of 15 mm on the JEOL and 19 mm on the LEO, an acceleration voltage of 20.0 kV and a corresponding current of 6.00 nA. Calibrations were performed every 120 min using a cobalt standard and a ZAF correction procedure provided by the JEOL and Inca software was applied. Compositional analyses were taken for 60 s, with multiple point analyses acquired to determine if any chemical heterogeneity occurred within or between grains. Anhydrous phase compositions were calculated to standard numbers of oxygen per formula unit (Deer et al., 1992), micas were recalculated to 11 oxygens, and chlorite to 28 oxygens. For hydrous mineral species, H_2O content was assumed to be present in stoichiometric amounts and, where relevant, the proportion of Fe_{3+}/Fe_{total} was calculated using AX (Holland, 2009) and amphibole vectors were calculated using the method of Holland and Blundy, 1994 using an in house excel spreadsheet.

A number of polished thin sections were analyzed for major elements and x-ray mapping was performed on a variety of scales; from entire thin section to major and accessory phase maps. Compositional profiles across garnets were determined on the JEOL by accumulating counts along a 256- channel line scan for approximately (25-30) minutes. The profiles were background-corrected and calibrated against up to six full point analyses taken at known positions along the profile in order to calculate mole fractions of garnet end members. On the LEO, garnet profiles were taken as equally spaced individual point analyses along a line traversing the garnets. Backscattered electron images of characteristic mineral associations, textures, compositional maps and line profiles are shown below for each sample.

Uncertainties on reported major elements were <1%. Scanning Electron Microscope imaging was also undertaken at the British Geological Survey UK, using a FEI Quanta 500 SEM. The SEM detectors were used to make element X-ray maps of whole thin sections (Al, Ca, Fe, K, Mg, Mn, Na, P, Si) Operating conditions were 15mm working distance and 0.6nA and 20kV beam conditions and the WDS spectrometer was used to collect maps of Y, Th, Ce, U, Yb zonation of monazites. X-ray maps were obtained for a range of major and trace elements using 15kV and 20nA beam conditions.

Full analytical data for all samples including ferric iron re-calculations are presented in the supplementary excel database S1.

3.2 Mineral Chemistry

3.2.1 Micas:

White mica chemistry varies spatially from a high-deep structural level of the Naxos Metamorphic Core Complex. In particular, they fall into 3 different populations: High Si (>3.4 p.f.u.) white mica is diagnostic of phengitic compositions which are diagnostic of higher pressure metamorphic environments are solely found in Zas Unit samples (see right hand side of diagram), whereas no analysed white mica from the Koronos or Core Units give any evidence for this composition. There is also high Na micas (>0.8 p.f.u.) from the Zas Unit which represent paragonite mica again associated with high-pressure conditions (see top left of plot below). Then there is another group to the bottom left of the plot with lower Si p.f.u. and overall smaller number of Mg, Fe_{2+} an Na p.f.u. representative of high-grade white mica associated with the amphibolite-facies.

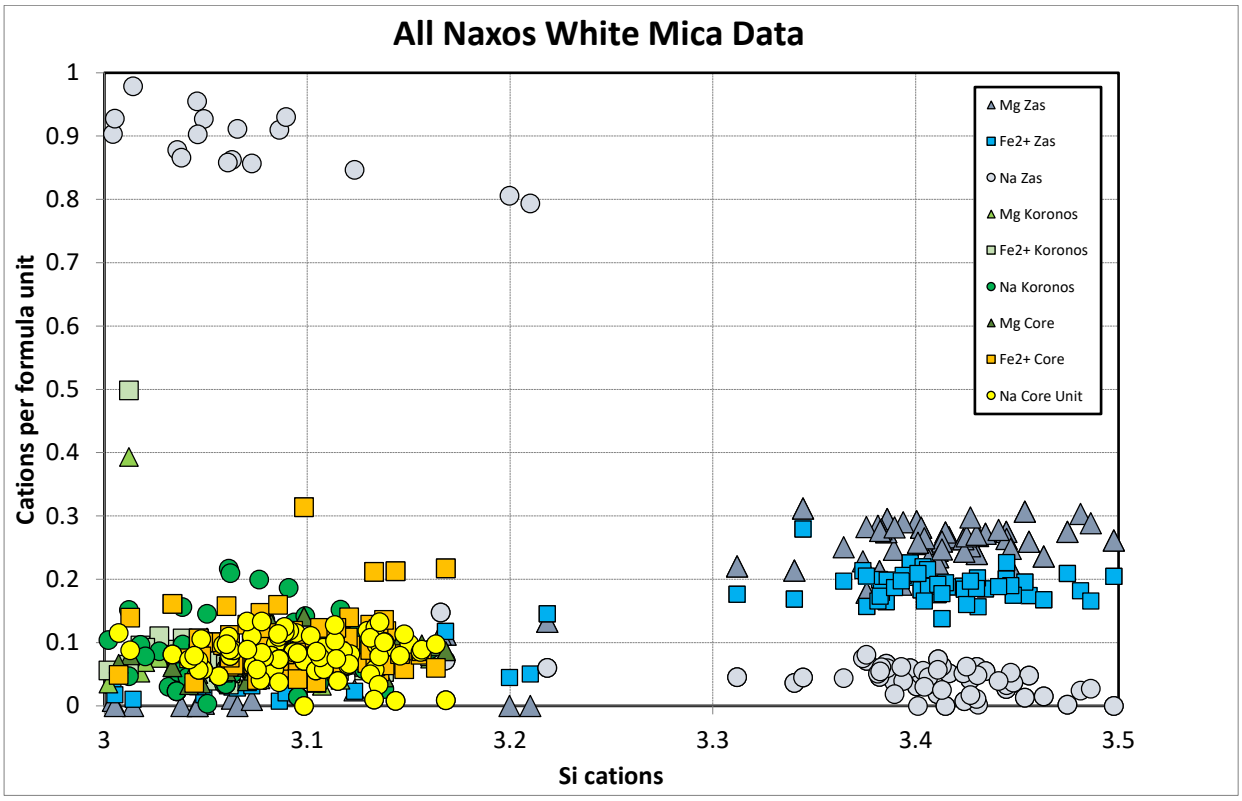

Figure 3.2.1.1 White mica plot of cations per unit formula vs Si cations per unit formula (for 11 oxygens)

Biotite chemistry shows similar patterns to the white mica data in that higher Ti values are seen within the Core and Koronos Units versus lower Ti values seen in analysed biotites from the Zas Unit. Zas Unit biotites also tend to have larger Mg numbers compared to the structurally deeper units. Together this implies that the Zas Unit didn't obtain as high temperatures and at the deepest levels there is no systematic change in biotite composition presumably due to equilibration at high temperature.

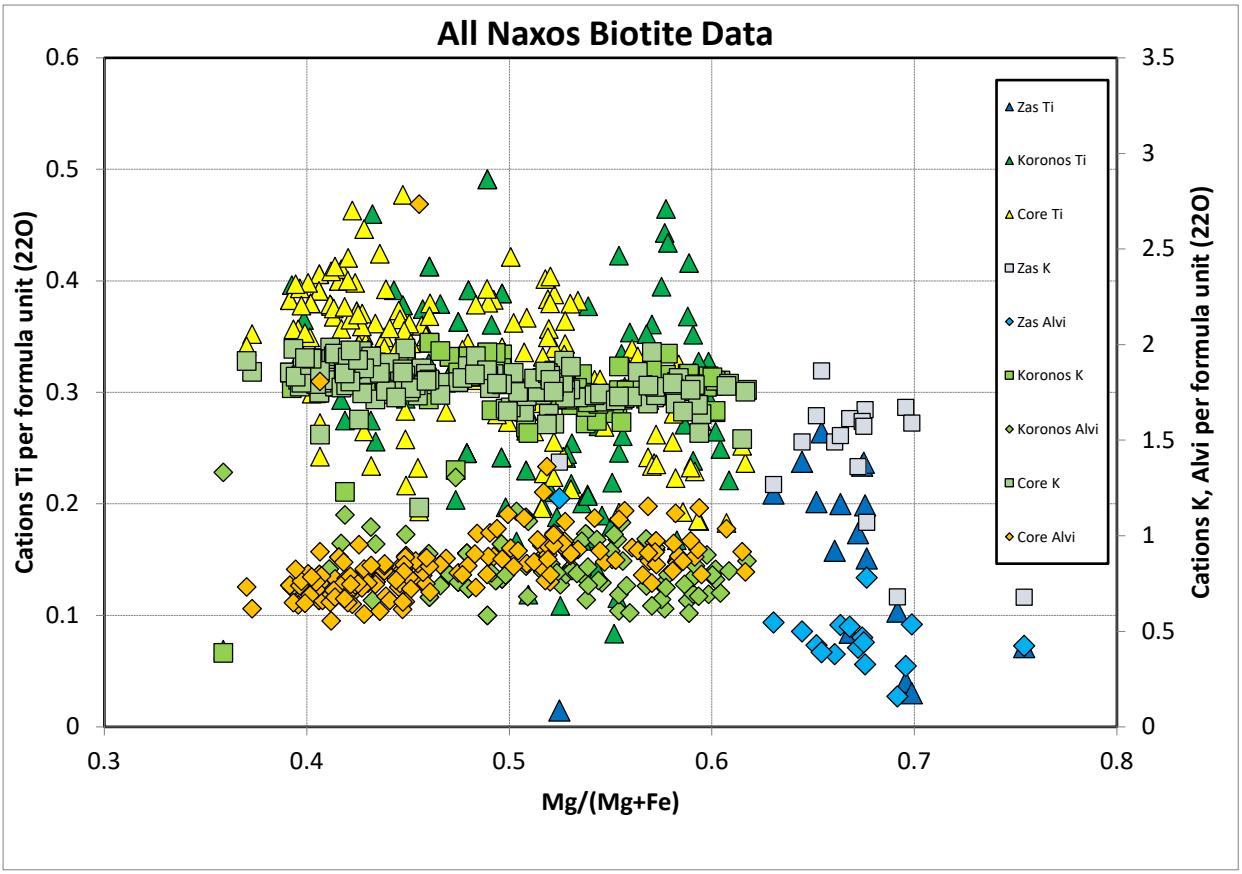

Figure 3.2.1.2 Biotite cations per unit formula for the Zas, Koronos, and Core Units

Amphiboles (Zas Unit)

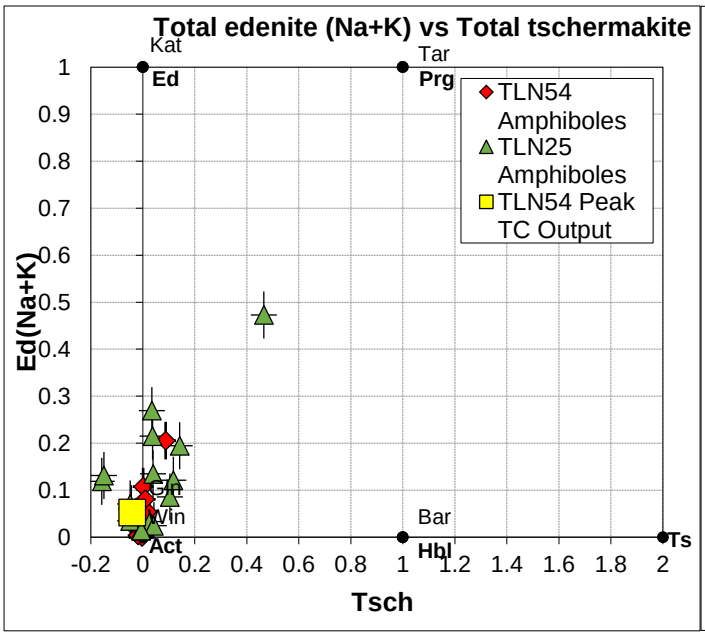

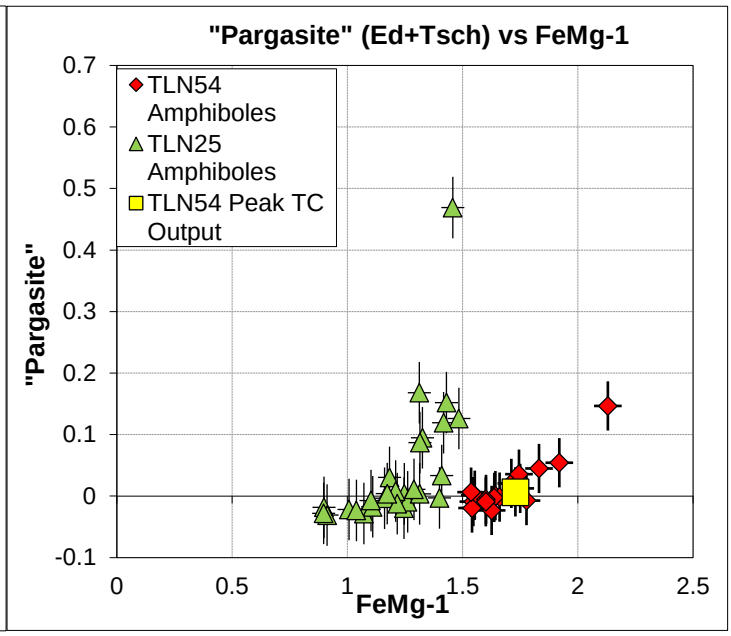

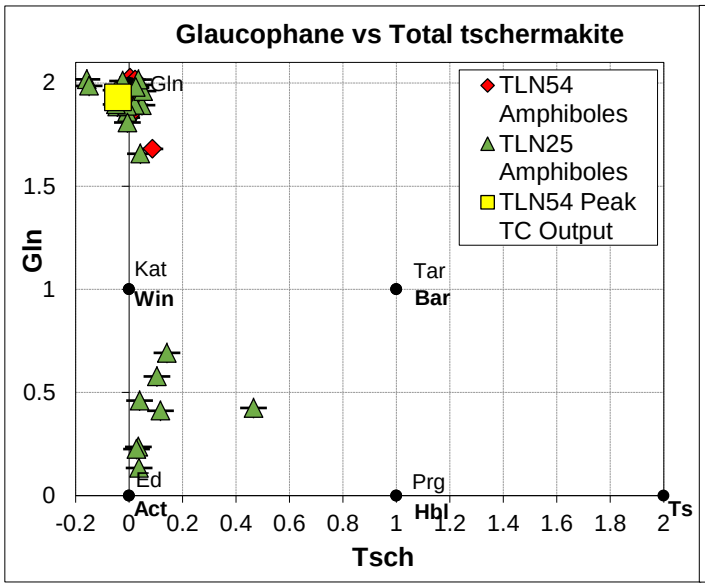

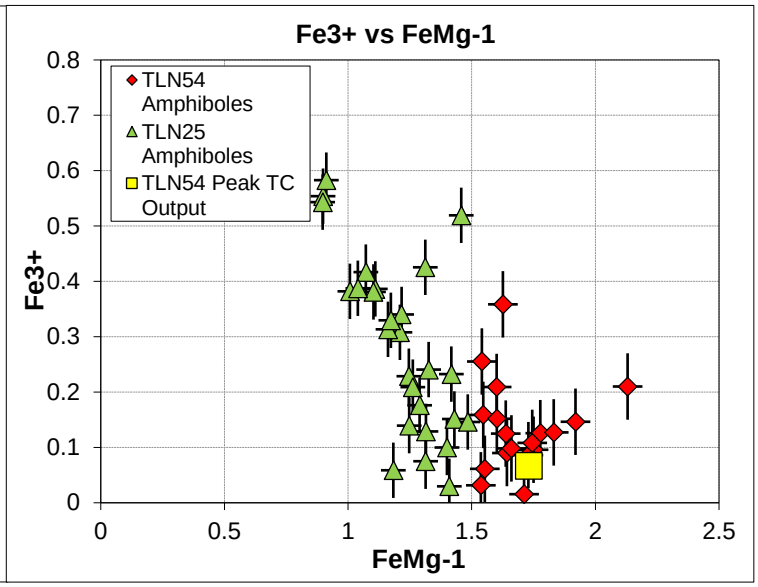

Amphibole compositions where recalculated for ferric iron following the method of Holland and Blundey, 1994. Within the Zas Unit, amphibole in samples TLN54 and TLN25 vary between glaucophane and actinolite compositions, with varying Fe_{3+}, low tschermakite (around 0) and low total edenite compositions. Glaucophane compositions vary between 0.1 and 2 with a major cluster at around 1.8-2.0 which we interpret to represent peak M_1 conditions. TLN25 has inclusions of glaucophane within epidote but matrix amphibole shows a spectrum of amphibole compositions from actinolite to winchite. Modelled amphibole results for sample TLN54 are plotted in the yellow box representing peak conditions of 14.5 kbars at 470 °C.

3.3 Zas Unit

3.3.1 TLN25

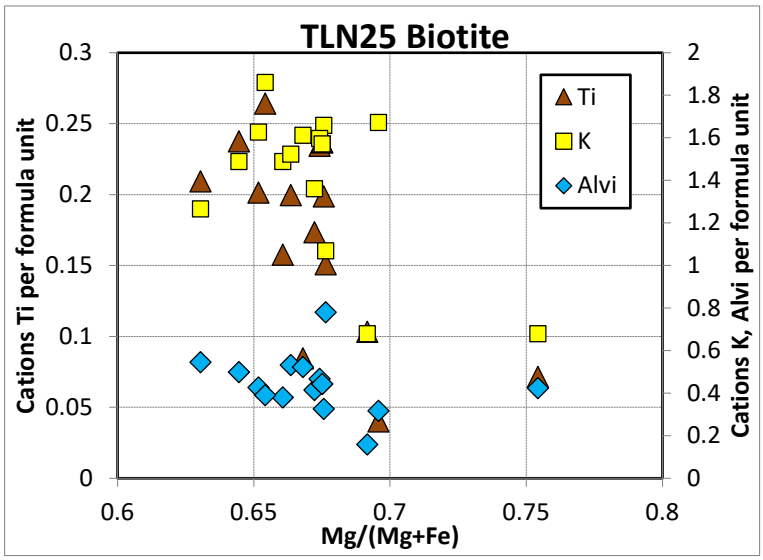

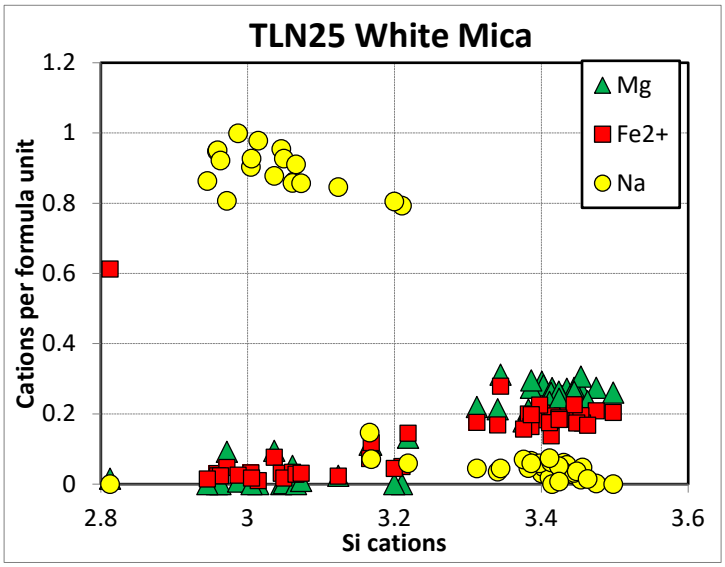

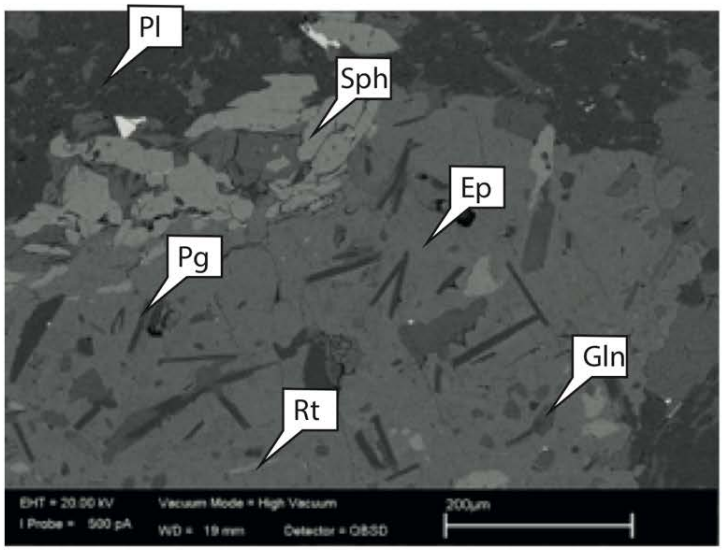

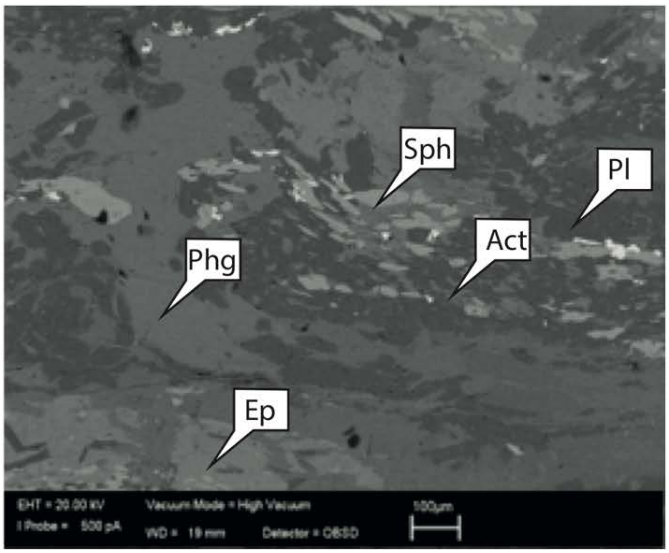

Figure 3.3.1.1 Representative backscatter electron images of TLN25 showing Left) Glaucophane, paragonite and rutile inclusions in epidote Right) Greenschist facies minerals, sphene actinolite and epidote are isoclinally folded with an S_2 crenulation, suggesting compression occurred at upper greenschis- facies conditions.

3.3.2 TLN26

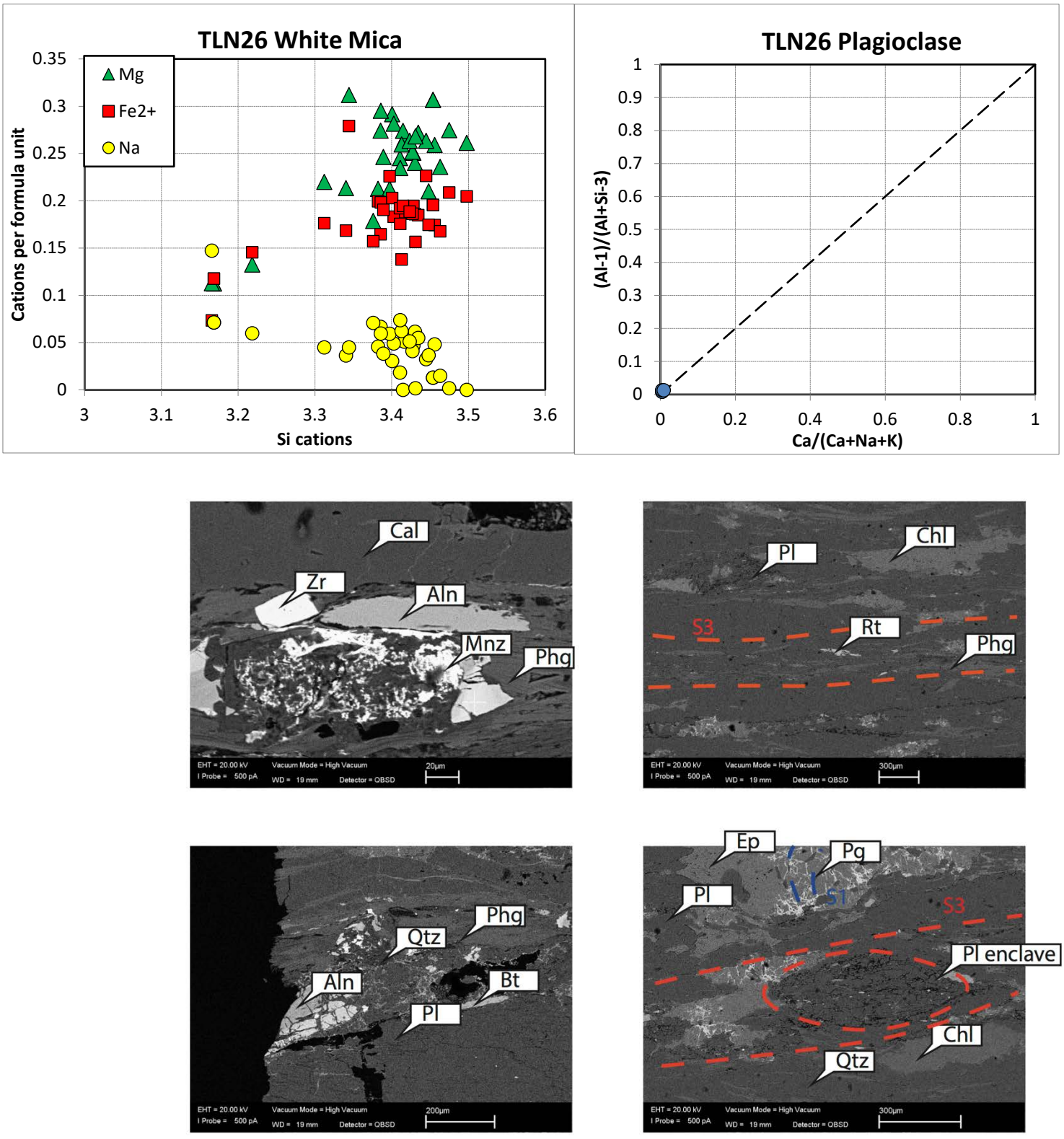

Figure 3.3.2.1 Representative back-scatter electron images of TLN26 retrogressed HP calc-schist showing remnants of high-pressure mineral assemblages that have been overprinted by strong greenschist facies retrogression. Allanite is preserved and aligned parallel to the pervasive S_3 fabric and is found partially breaking down to monazite and kyanite. Pargonite is preserved as inclusions in epidote as a discordant fabric to greenschist facies shearing.

3.3.3 TLN54:

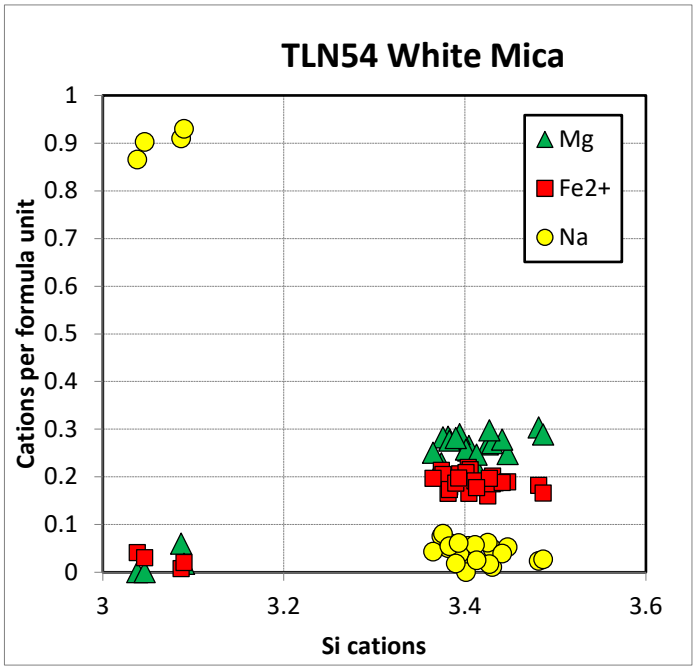

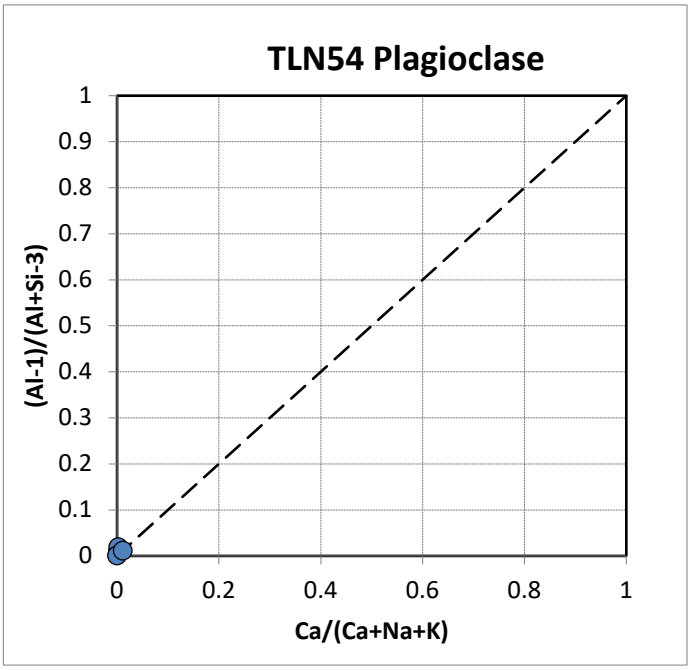

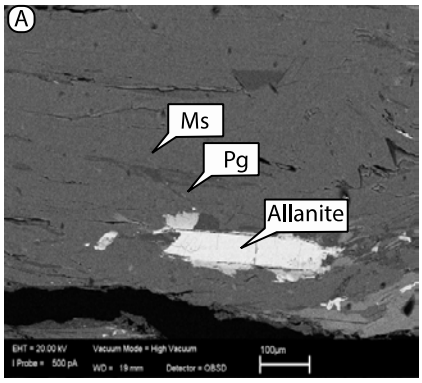

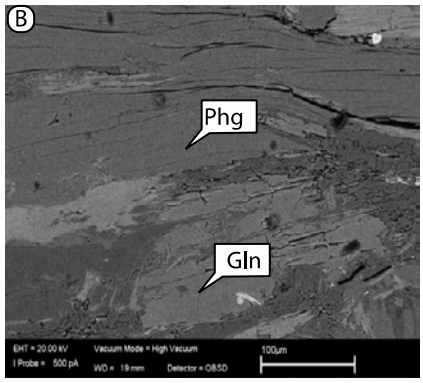

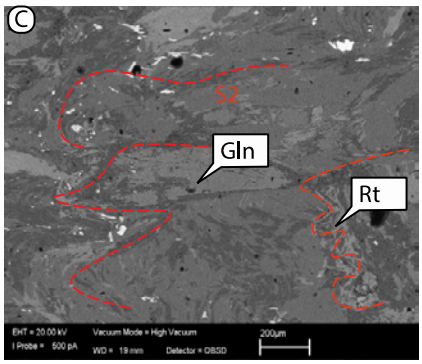

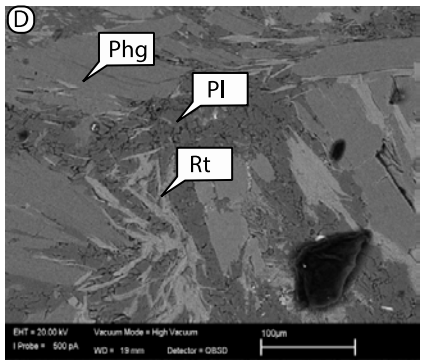

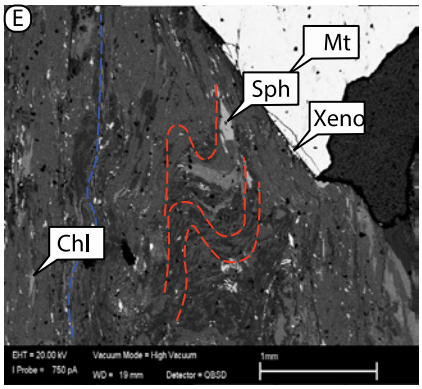

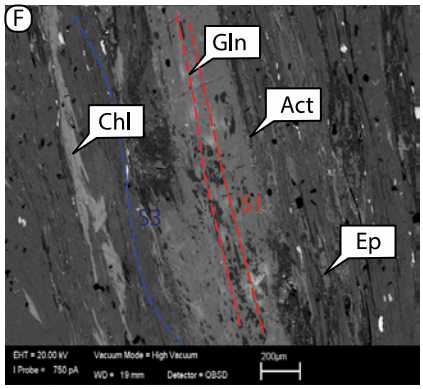

Figure 3.2.3.1 Representative SEM backscattered electron images for sample TLN54, showing the major phases and their relationships to deformation microstructures. S_1 Pre-Syn tectonic with glaucophane. S_2 crenulation cleavage, deforms rutile needles and glaucophane and is pre-tectonic with respect to epidote. S_3 is greenschist facies top-to-NNE shearing with cross-cuts earlier fabrics.

3.4 Koronos Unit

3.4.1 TL67

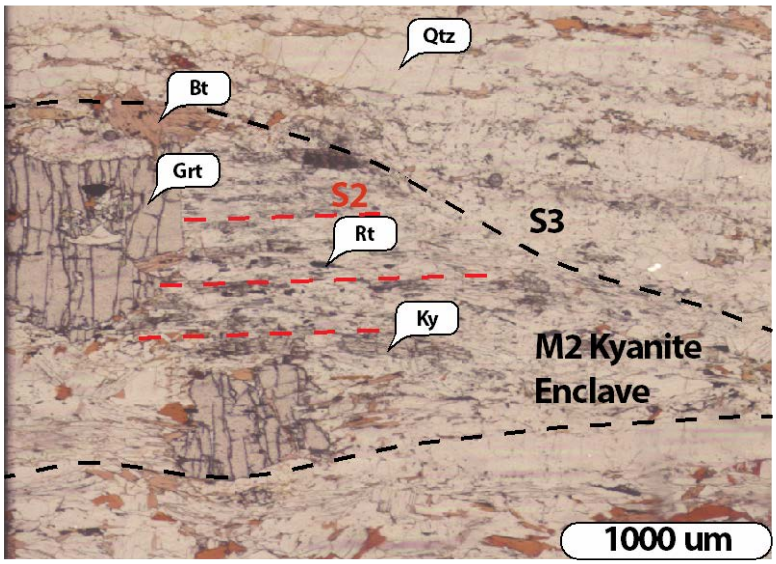

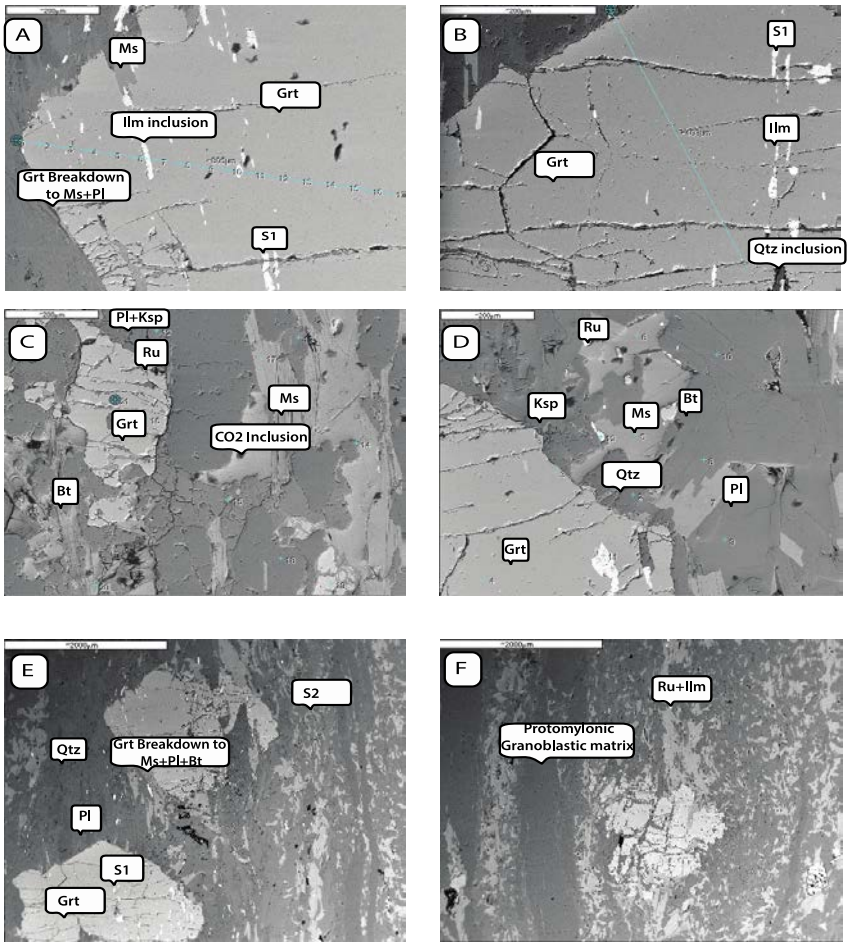

Figure 3.4.1.1: Zoomed in slide scan of TL67 and representative backscattered SEM images showing the peak M_2 Kyanite grade assemblage within plagioclase + muscovite + kyanite + garnet enclaves. Within the enclaves kyanite is aligned along S_2 that is oblique to the external S_3 top-to-NNE shearing fabric. Garnet rims clearly overgrow S_2 but are sheared by S_3 indicating they preserve the peak prograde history.

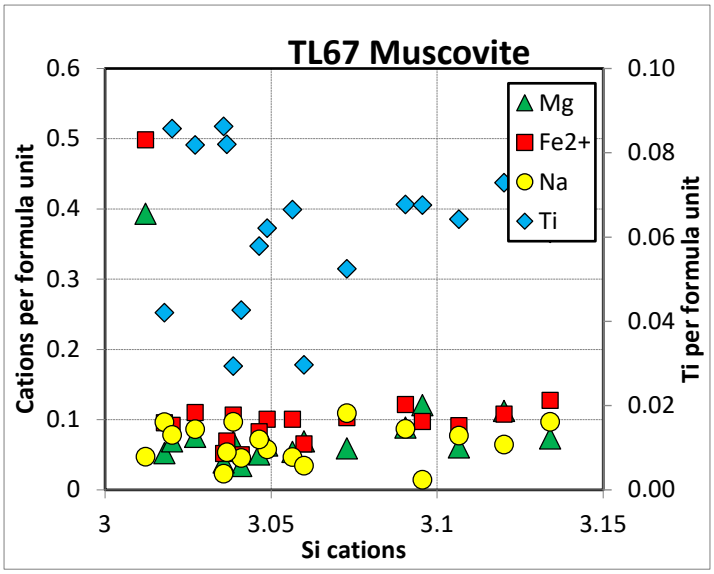
TL67 Muscovite
Cations per formula unit
Ti per formula unit
Si cations
Mg
Fe2+
Na
Ti
0.6
0.5
0.4
0.3
0.2
0.1
0
0.10
0.08
0.06
0.04
0.02
0.00
3
3.05
3.1
3.15

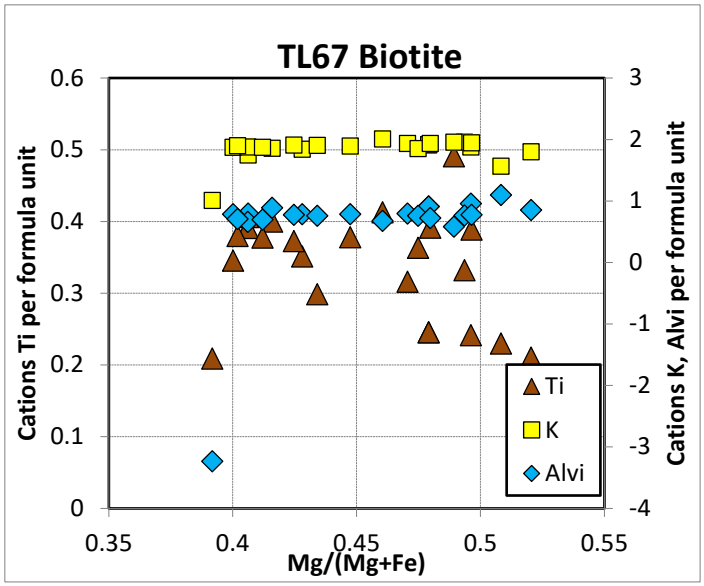
TL67 Biotite
Cations Ti per formula unit
Cations K, Alvi per formula unit
Mg/(Mg+Fe)
Ti
K
Alvi
0.6
0.5
0.4
0.3
0.2
0.1
0
3
2
1
0
-1
-2
-3
-4
0.35
0.4
0.45
0.5
0.55

Garnet Maps

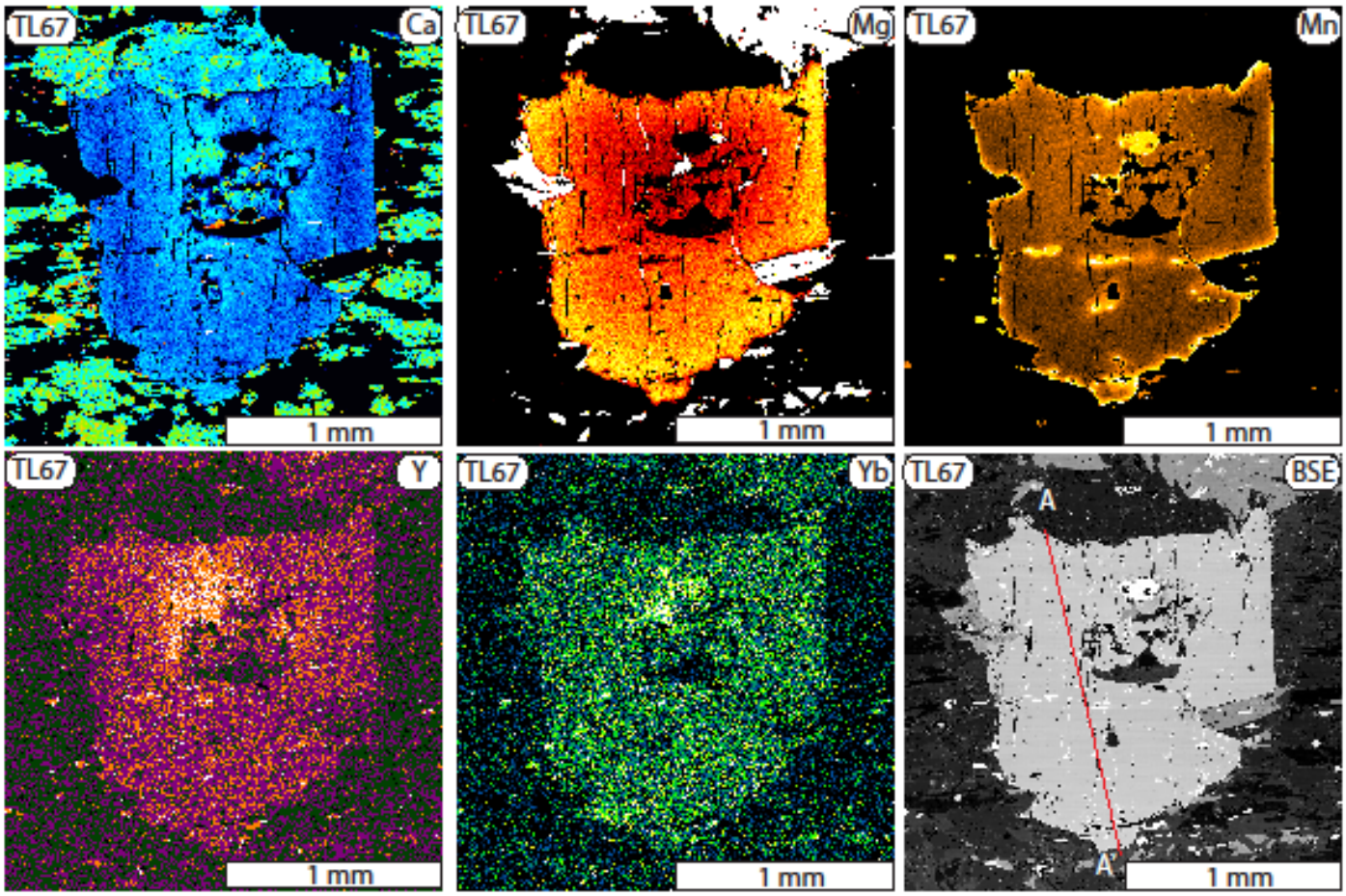
TL67
Ca
Mg
Mn
Y
Yb
BSE
A
A'
1 mm

Garnet line profiles

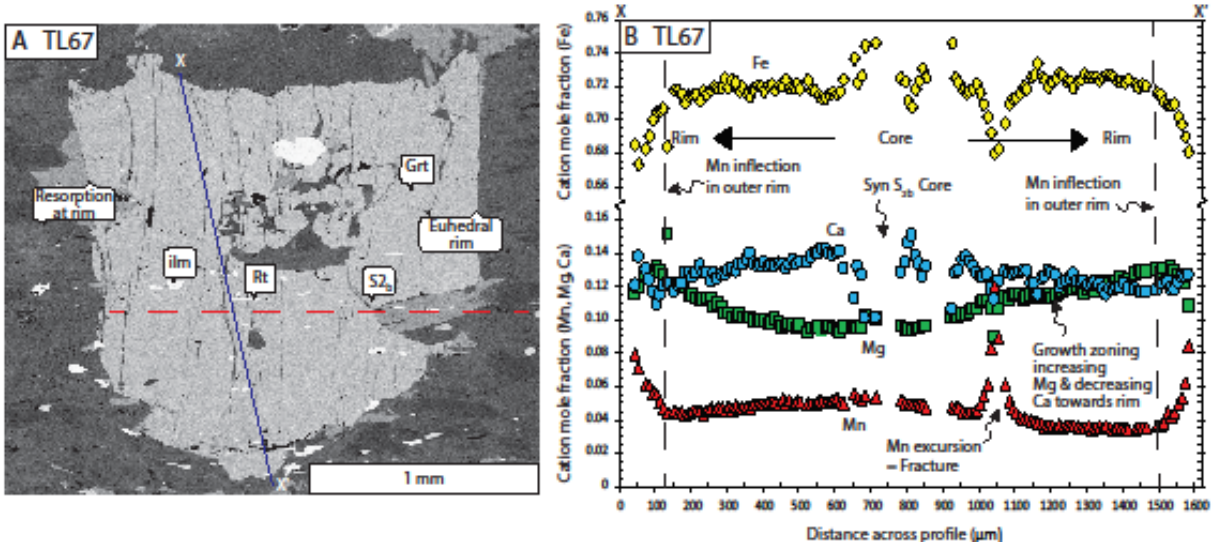

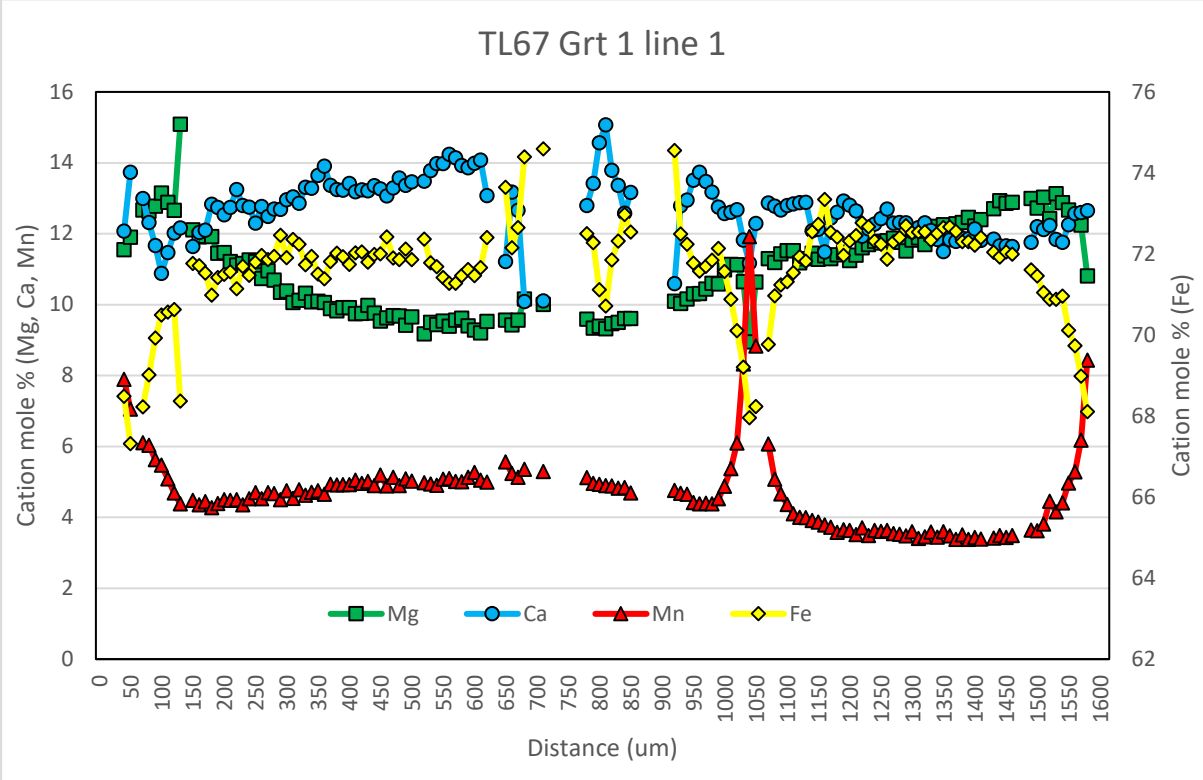

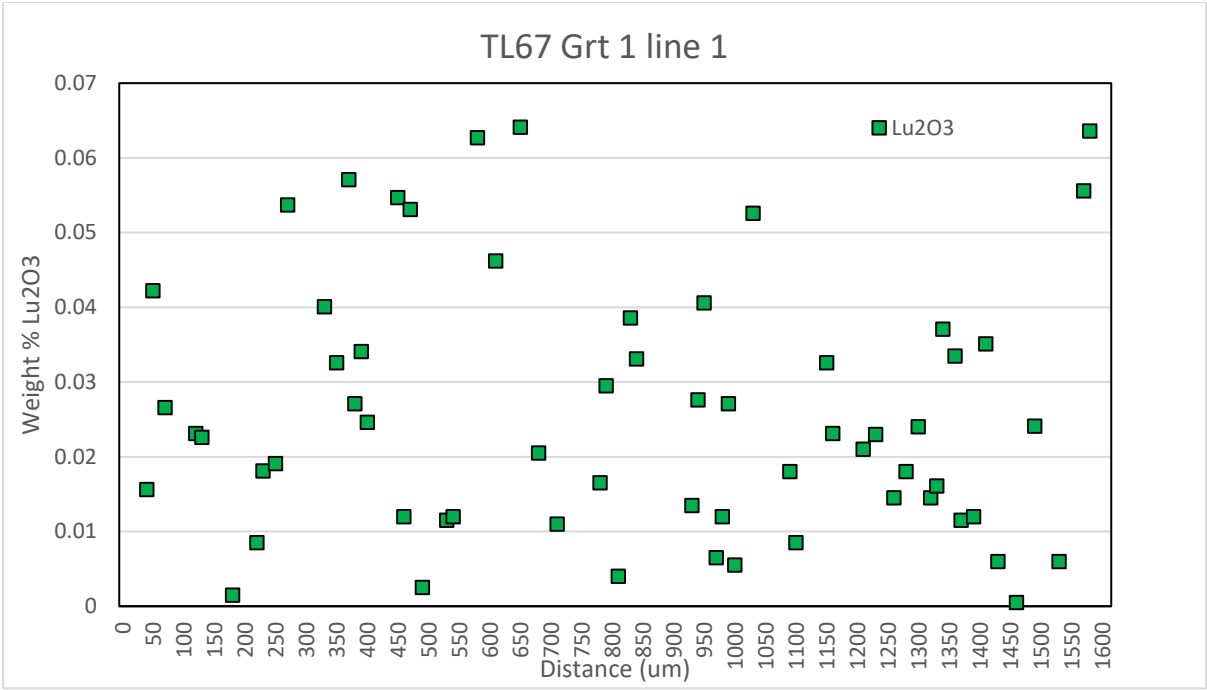
TL67 Grt 1 line 1
Lu2O3
Weight % Lu2O3
Distance (um)

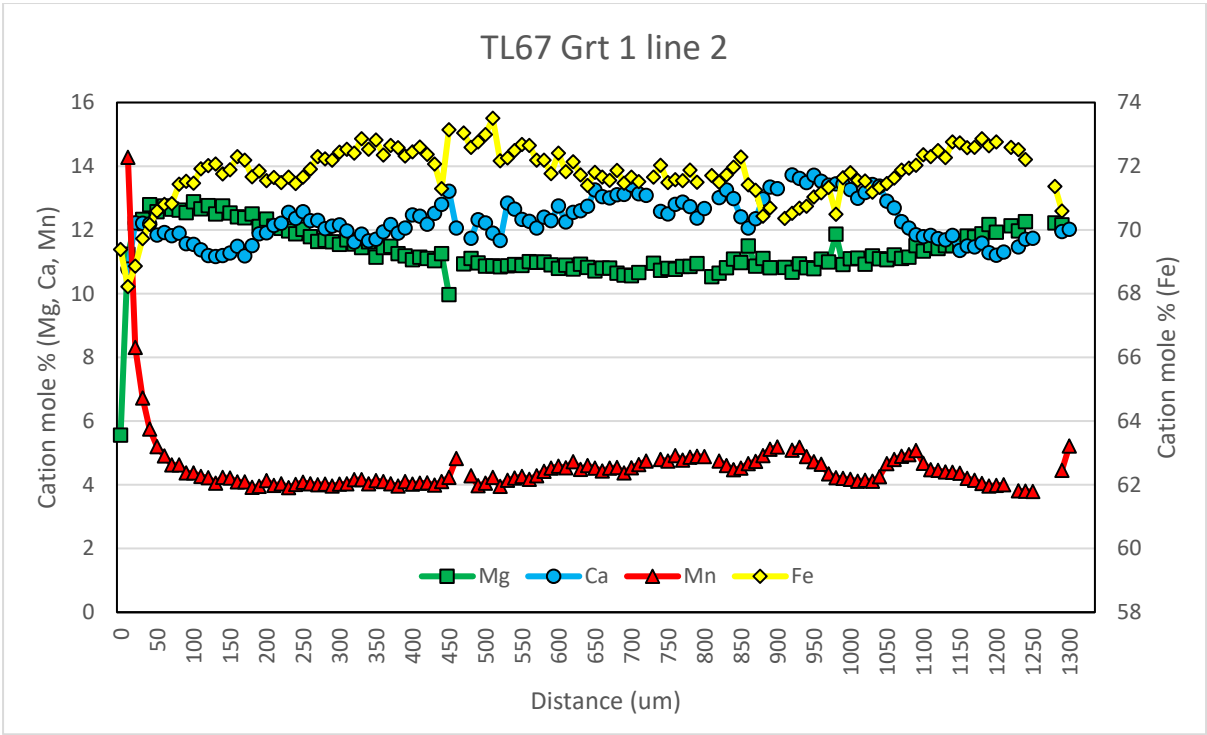
TL67 Grt 1 line 2
Mg
Ca
Mn
Fe
Cation mole % (Mg, Ca, Mn)
Cation mole % (Fe)
Distance (um)

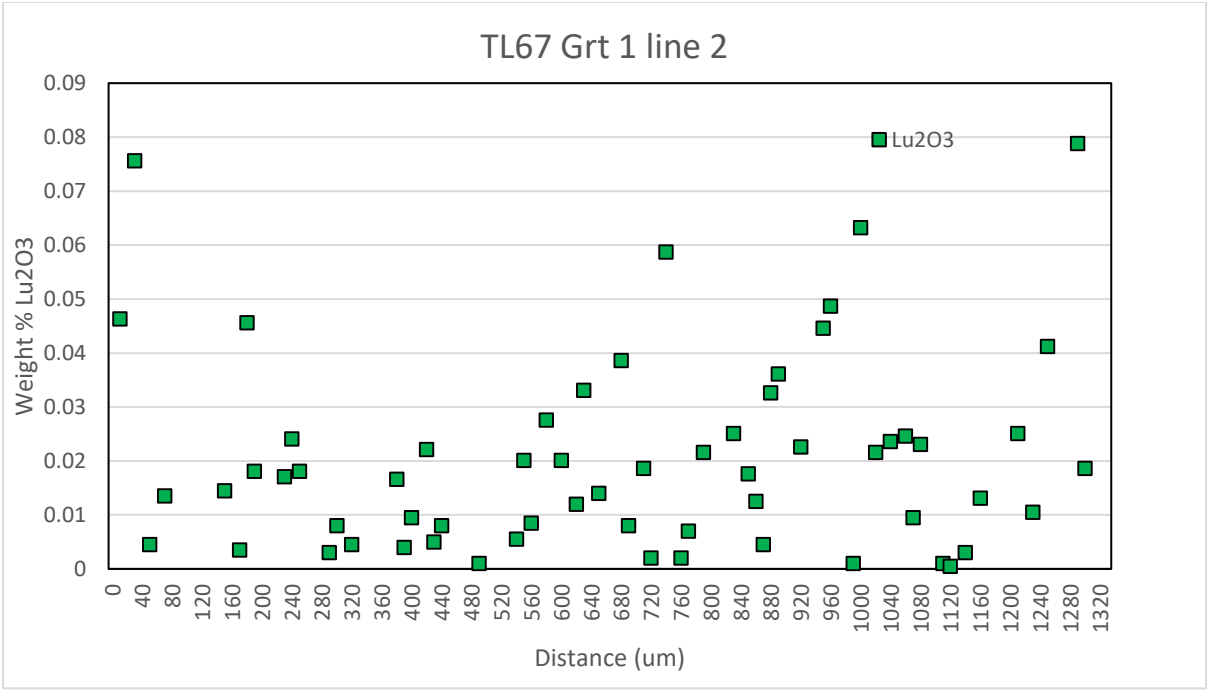
TL67 Grt 1 line 2
Lu2O3
Weight % Lu2O3
Distance (um)
0.09
0.08
0.07
0.06
0.05
0.04
0.03
0.02
0.01
0
0 40 80 120 160 200 240 280 320 360 400 440 480 520 560 600 640 680 720 760 800 840 880 920 960 1000 1040 1080 1120 1160 1200 1240 1280 1320

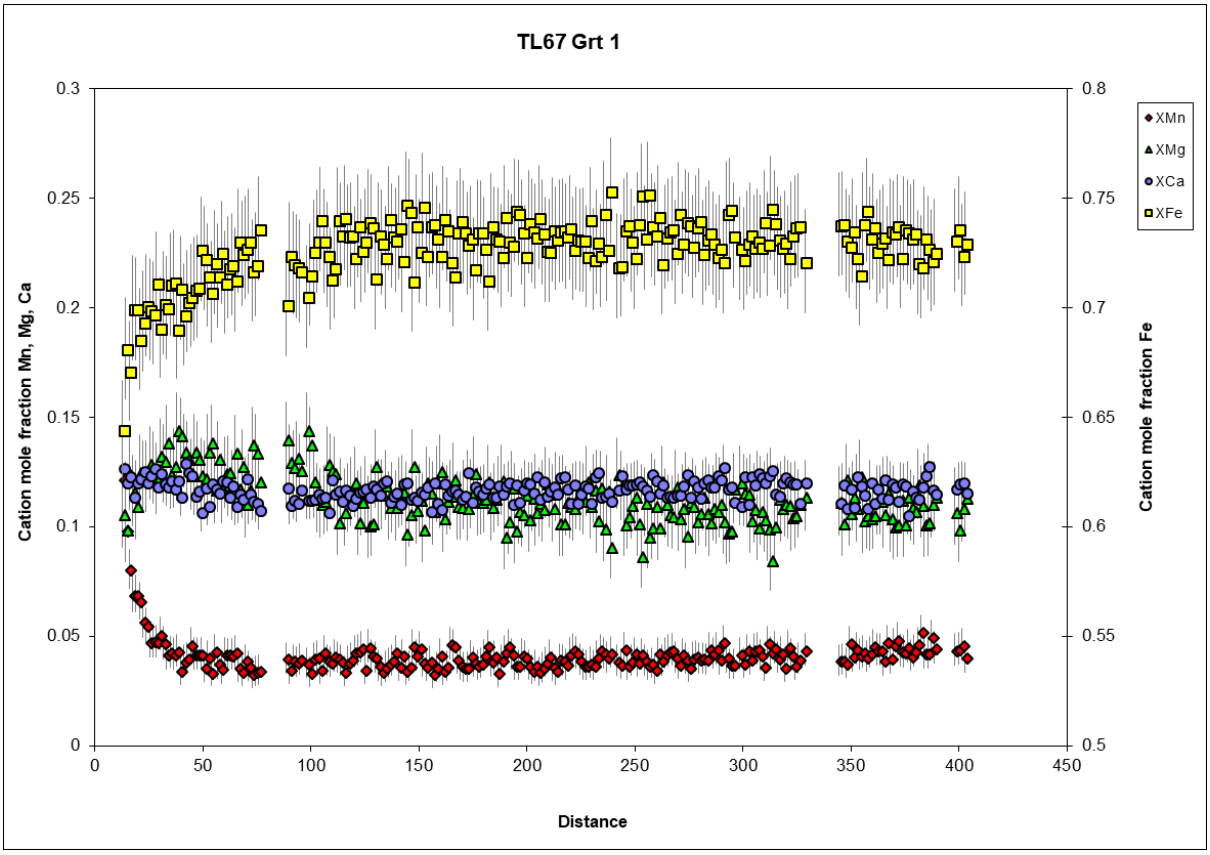
TL67 Grt 1
XMn
XMg
XCa
XFe
Cation mole fraction Mn, Mg, Ca
Cation mole fraction Fe
Distance
0.3
0.25
0.2
0.15
0.1
0.05
0
0.8
0.75
0.7
0.65
0.6
0.55
0.5
0 50 100 150 200 250 300 350 400 450

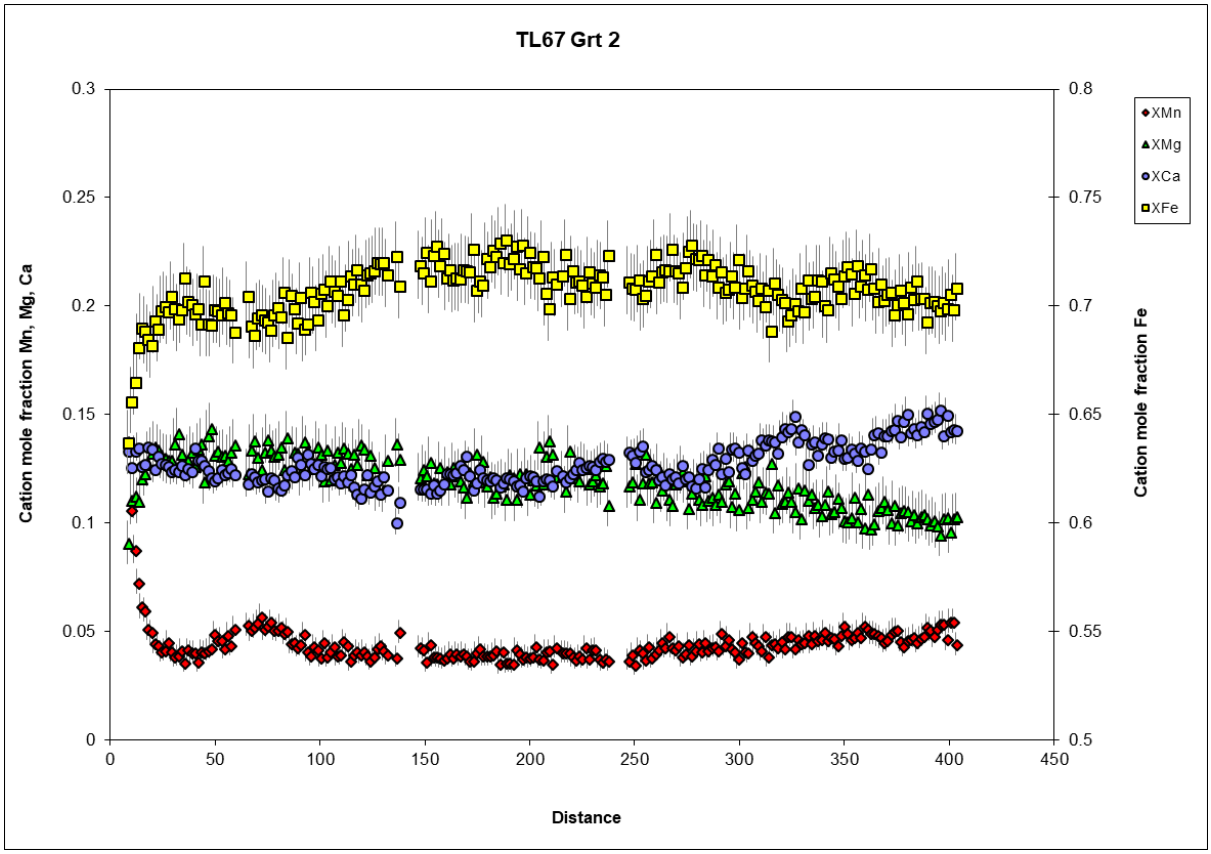
TL67 Grt 2
Cation mole fraction Mn, Mg, Ca
Cation mole fraction Fe
Distance
XMn
XMg
XCa
XFe
0.3
0.25
0.2
0.15
0.1
0.05
0
0.8
0.75
0.7
0.65
0.6
0.55
0.5
0
50
100
150
200
250
300
350
400
450

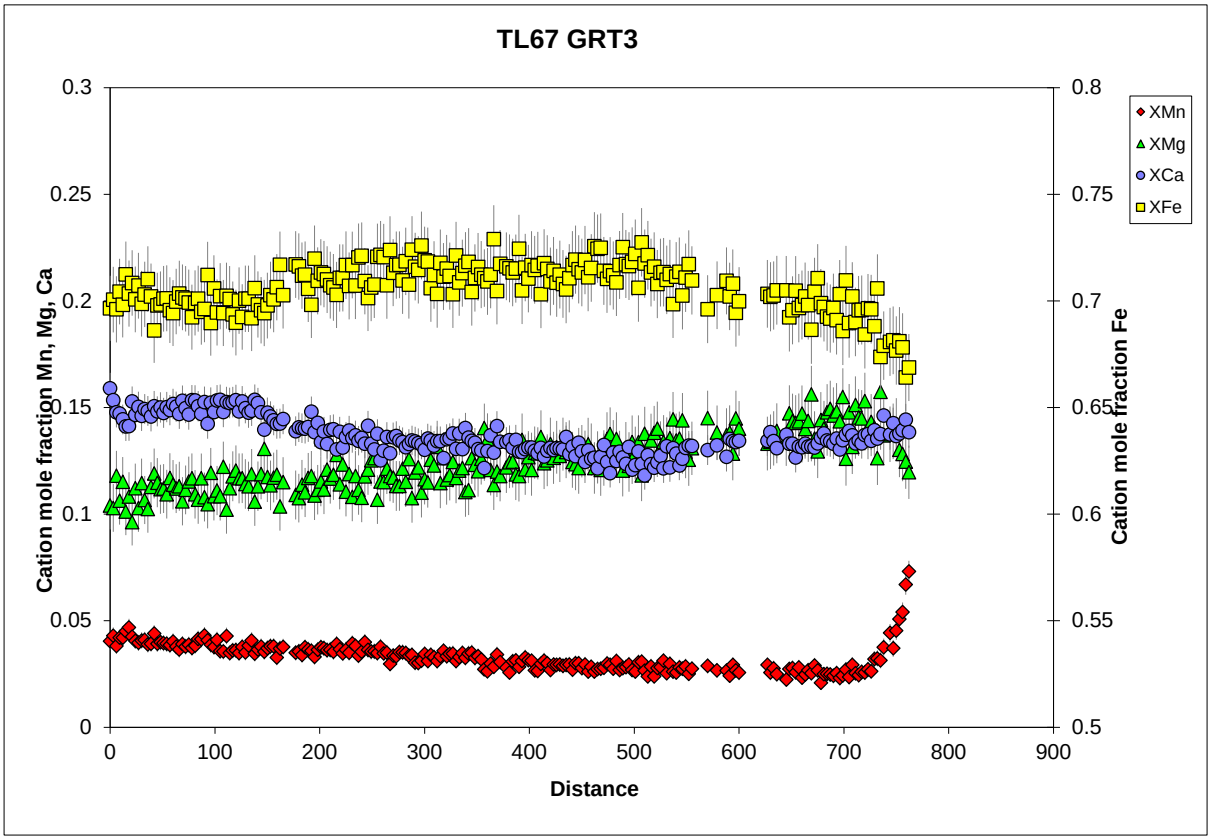
TL67 GRT3
Cation mole fraction Mn, Mg, Ca
Cation mole fraction Fe
Distance
XMn
XMg
XCa
XFe
0.3
0.25
0.2
0.15
0.1
0.05
0
0.8
0.75
0.7
0.65
0.6
0.55
0.5
0
100
200
300
400
500
600
700
800
900

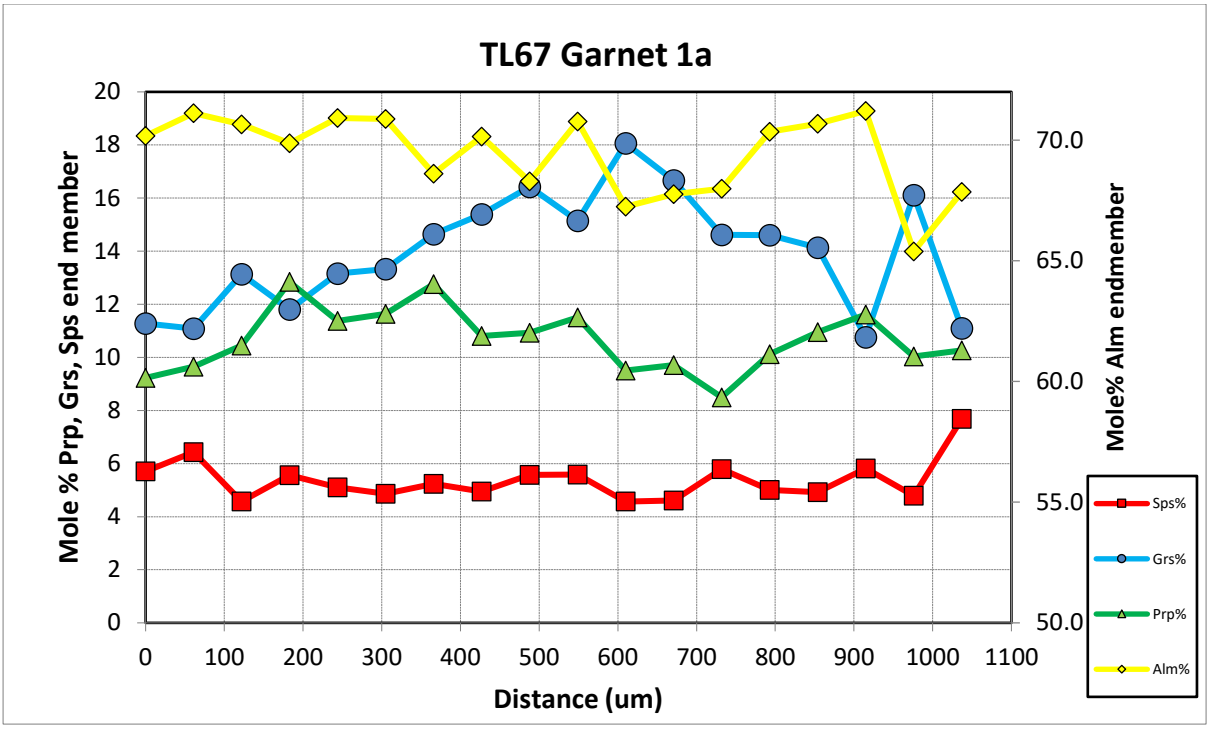
TL67 Garnet 1a
Mole % Prp, Grs, Sps end member
Mole% Alm endmember
Distance (um)
Sps%
Grs%
Prp%
Alm%

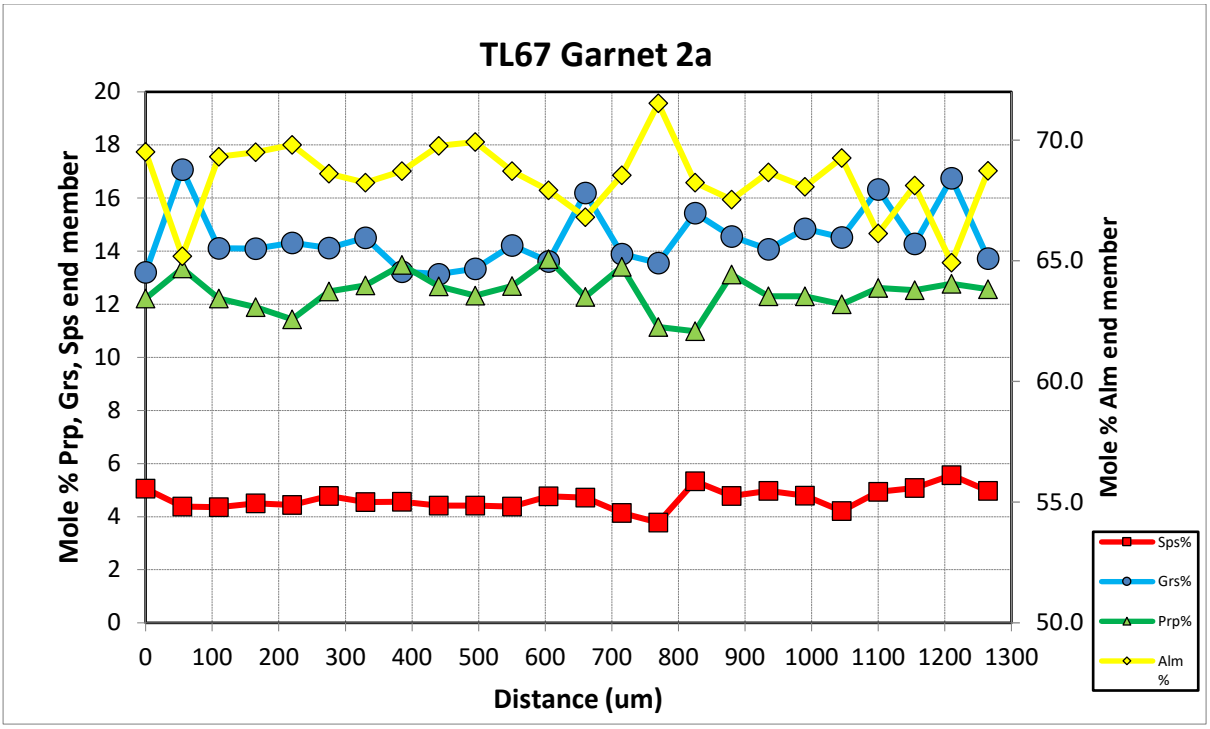
TL67 Garnet 2a
Mole % Prp, Grs, Sps end member
Mole % Alm end member
Distance (um)
Sps%
Grs%
Prp%
Alm %

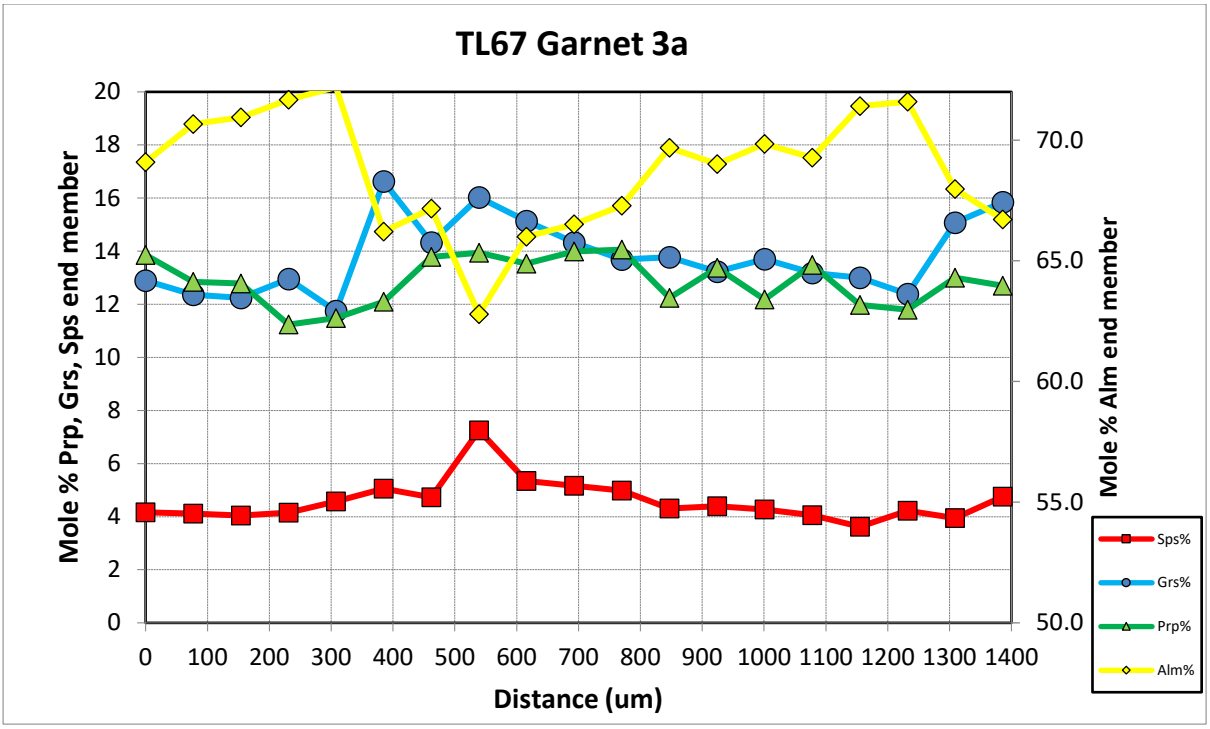

Garnet profiles show a mixture of prograde zoning that is affected by re-equilibration and diffusion with a classic diffusion closure profile with a kick of Mn at the rim reflecting resorbtion. Garnet cores are associated with the highest grossular at around 16% but varying between 14-18% with 12-14% pyrope. At the rim there is a kick of Pyrope to around 14-15% with a decrease in grossular to around 12-13% followed by a slight increase to around 13%. We interpret this increase in pyrope towards the rim as peak conditions that overgrows the prograde M_2 kyanite grade foliation (S_{2a} and S_{2b}) at around 10 kbars 670 °C.

3.4.2 TLN16

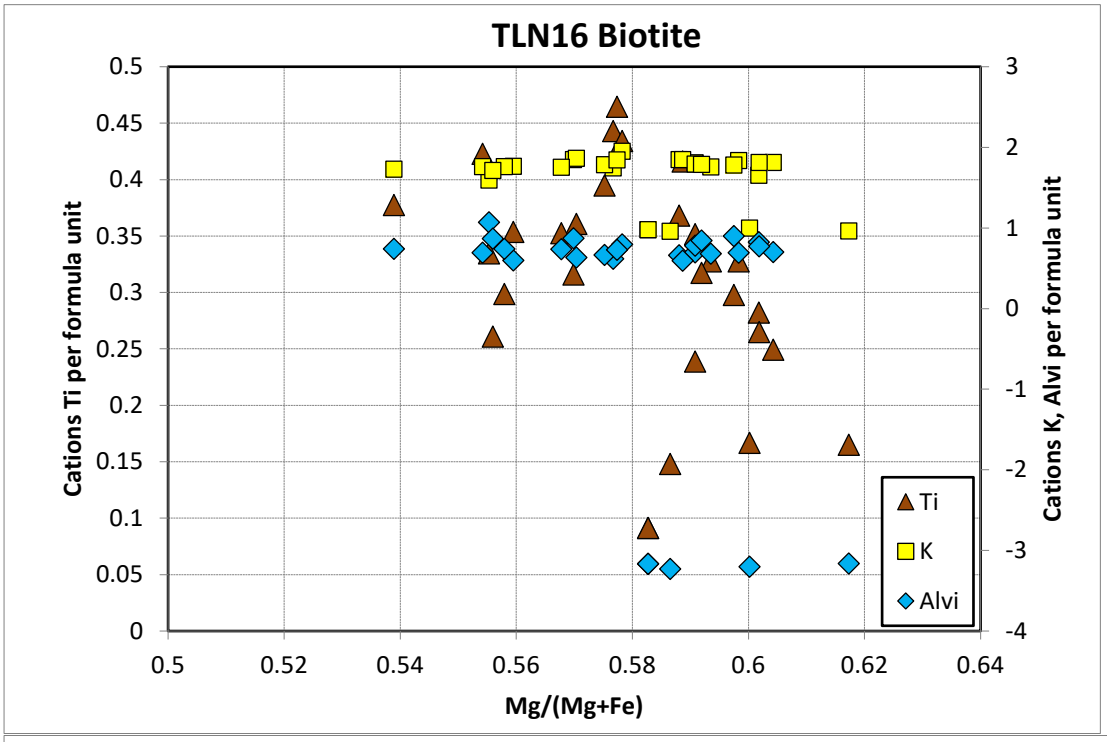
TLN16 Biotite
Cations Ti per formula unit
Cations K, Alvi per formula unit
Mg/(Mg+Fe)
Ti
K
Alvi
0.5
0.45
0.4
0.35
0.3
0.25
0.2
0.15
0.1
0.05
0
3
2
1
0
-1
-2
-3
-4
0.5
0.52
0.54
0.56
0.58
0.6
0.62
0.64

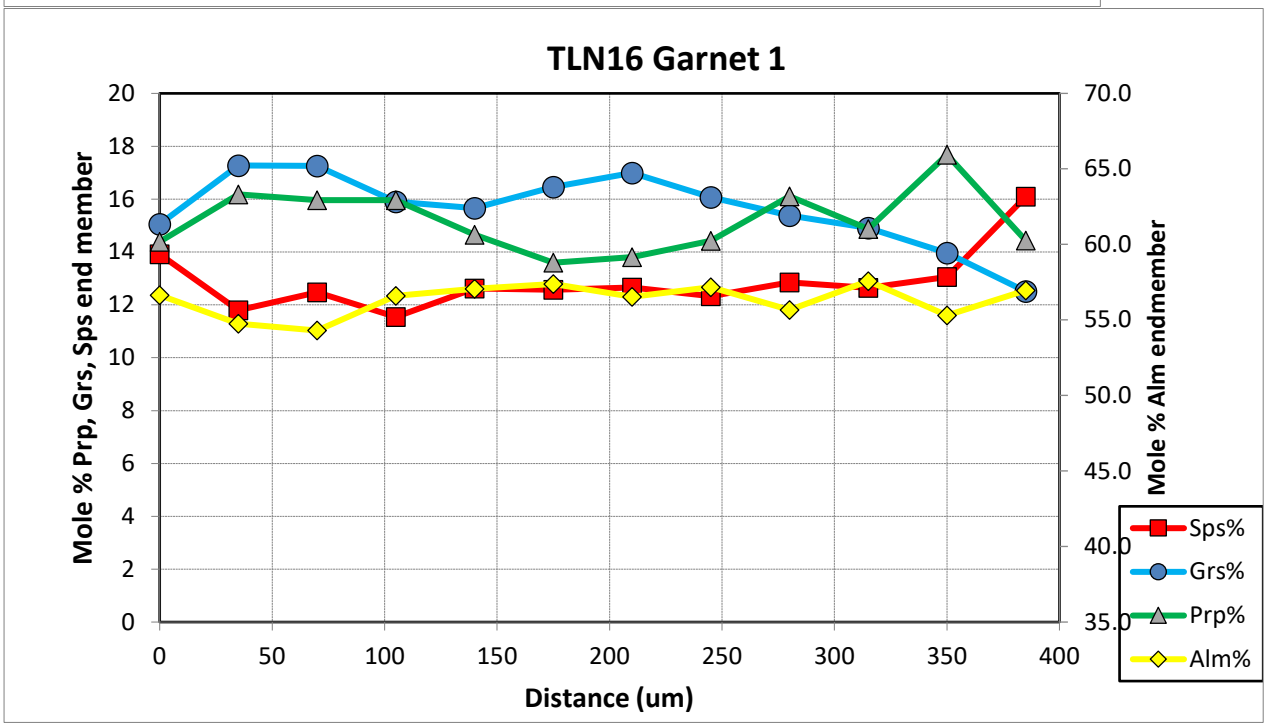
TLN16 Garnet 1
Mole % Prp, Grs, Sps end member
Mole % Alm endmember
Distance (um)
Sps%
Grs%
Prp%
Alm%
20
18
16
14
12
10
8
6
4
2
0
70.0
65.0
60.0
55.0
50.0
45.0
40.0
35.0
0
50
100
150
200
250
300
350
400

3.4.3 TLN21

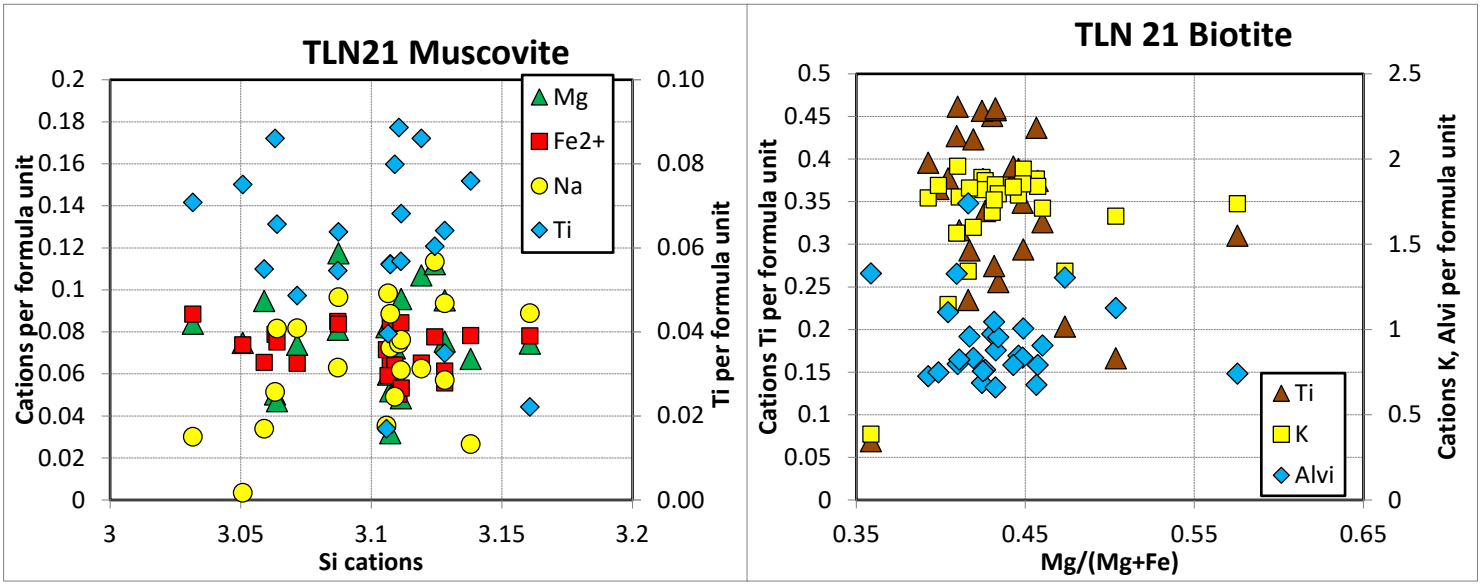

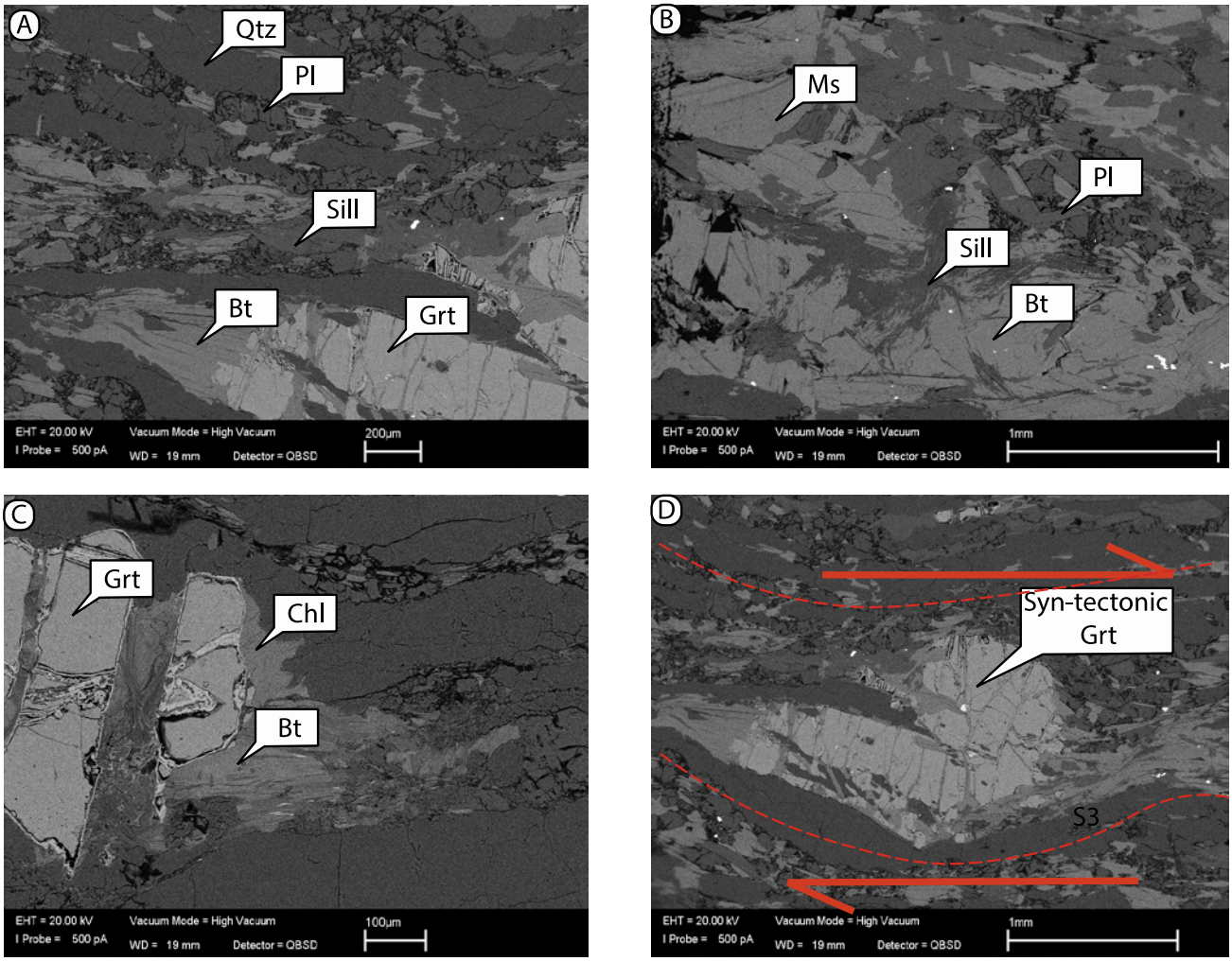

Figure 3.4.3.1TLN21 Representative backscattered SEM images with syn-tectonic garnet with respect to S_3 top-to-NNE shearing with M_3 sillimanite grade assemblage that is post-kinematic with respect to shearing.

Garnet line profiles

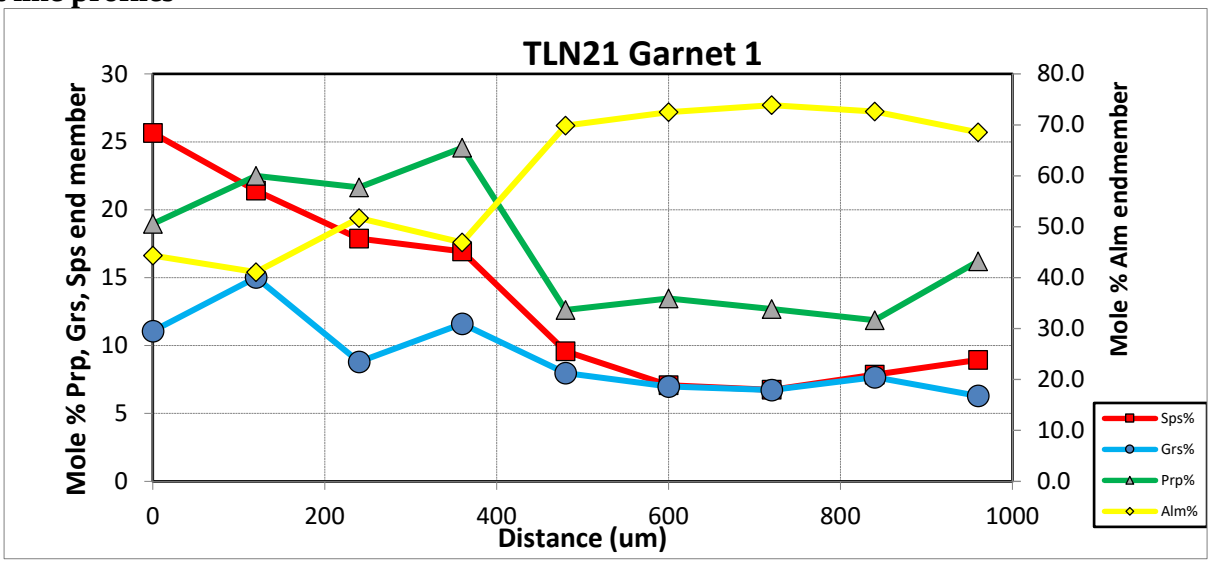

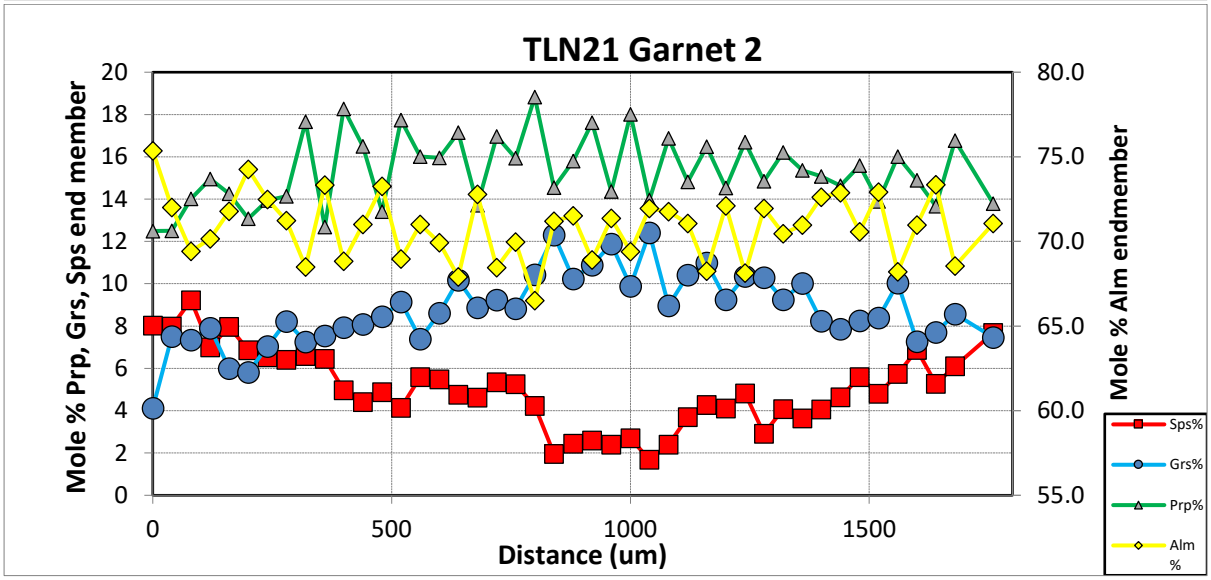

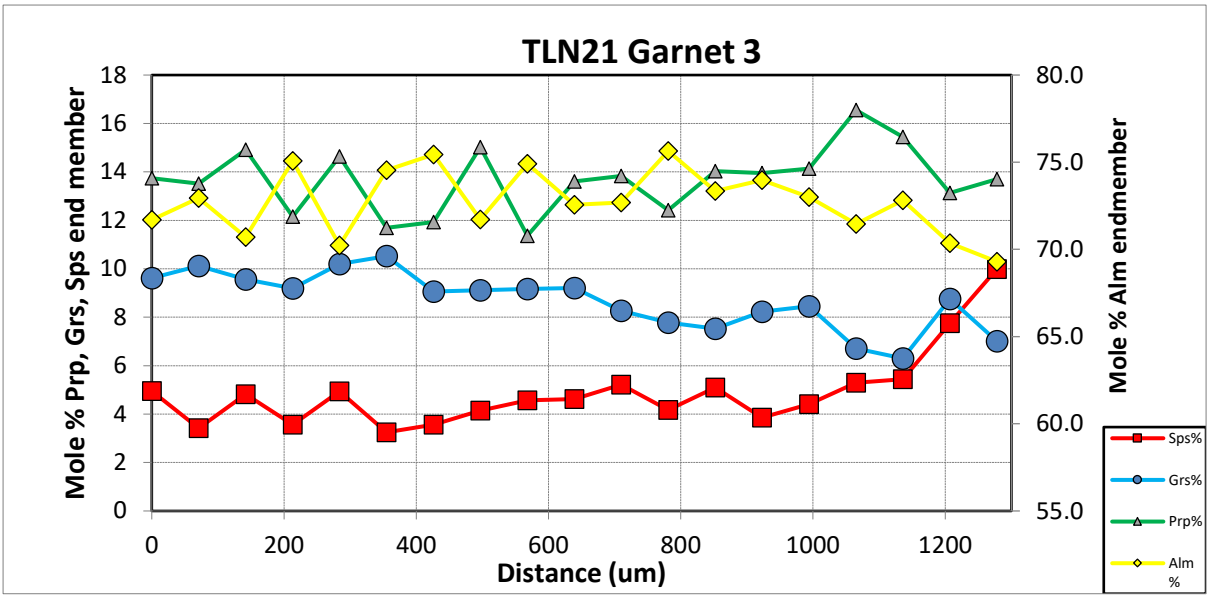

Garnet profiles show a systematic trend with not much change in Pyrope but decreasing grossular towards the rim. Pyrope has some variability but remains at between 13-17% from core to rim, whilst grossular decreases from around 12% to 7%. This is associated with decompression, with some garnet resorption as indicated by classic diffusion closure profiles of Mn increasing towards the rim. This decompression is associated with the transition from kyanite-sillimanite producing sillimanite-biotite intergrowths that cross-cut the S3 top-to-NNE shearing fabric. Static recrystallization and annealing at lower pressure conditions has coarsened the microstructure and hydration has resulted in secondary muscovite formation.

3.4.4 TLN22

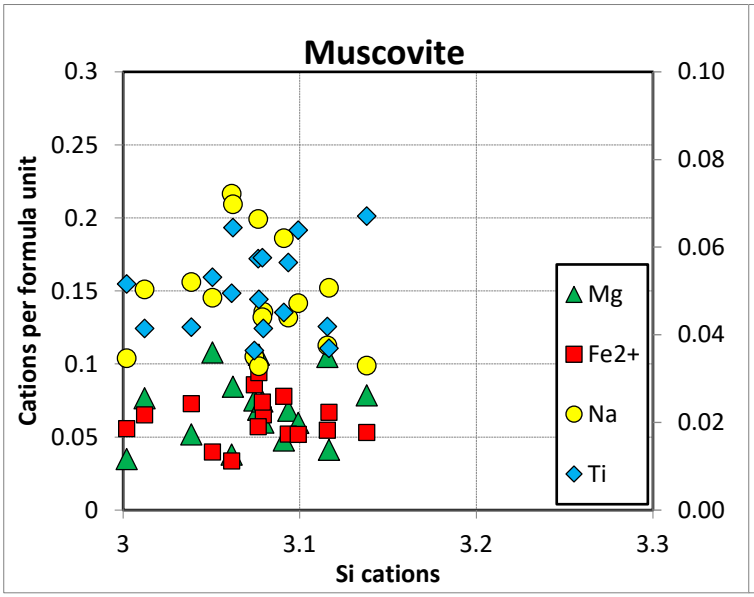

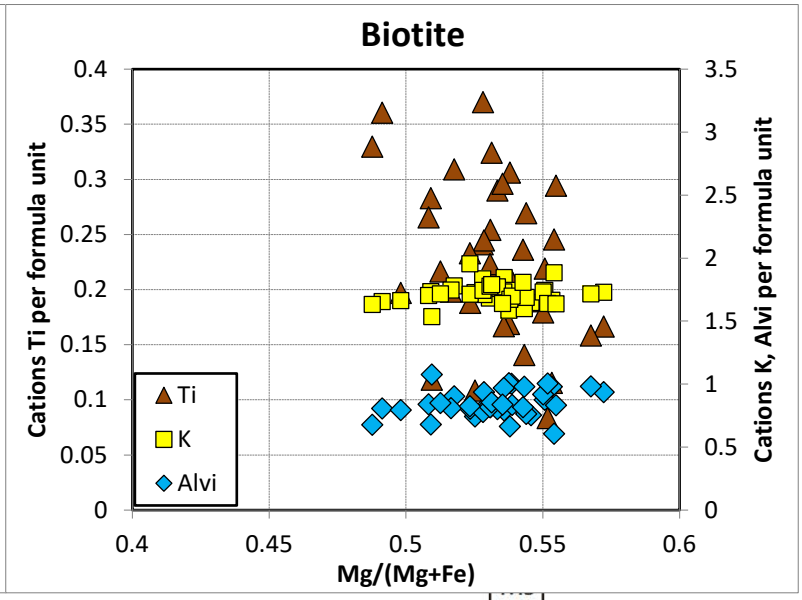

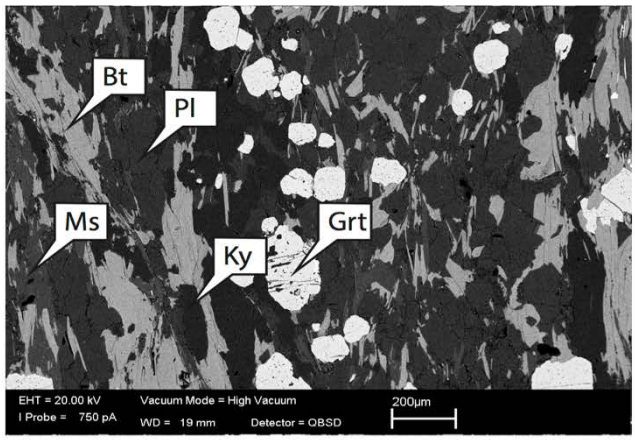

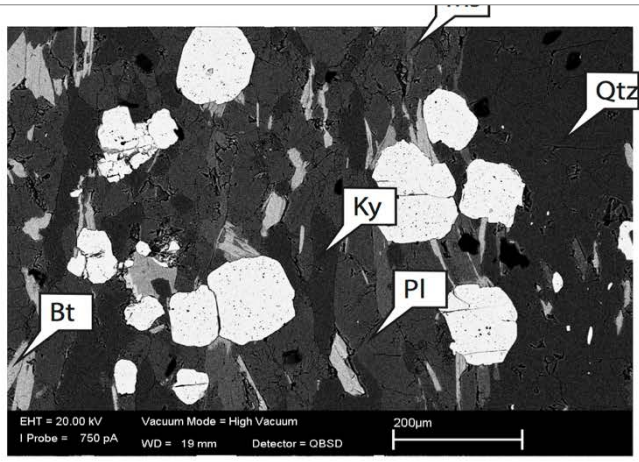

Figure 3.4.4.1: Representative SEM images of post-tectonic garnets with respect to the S_2 and S_3 fabrics. Kyanite is preserved as enclaves with muscovite + plagioclase that S_3 deforms around and garnet cores have a high concentration of fluid inclusions wheras their rims don't, indicating their rims formed as a separate garnet growth episode.

Garnet line profiles

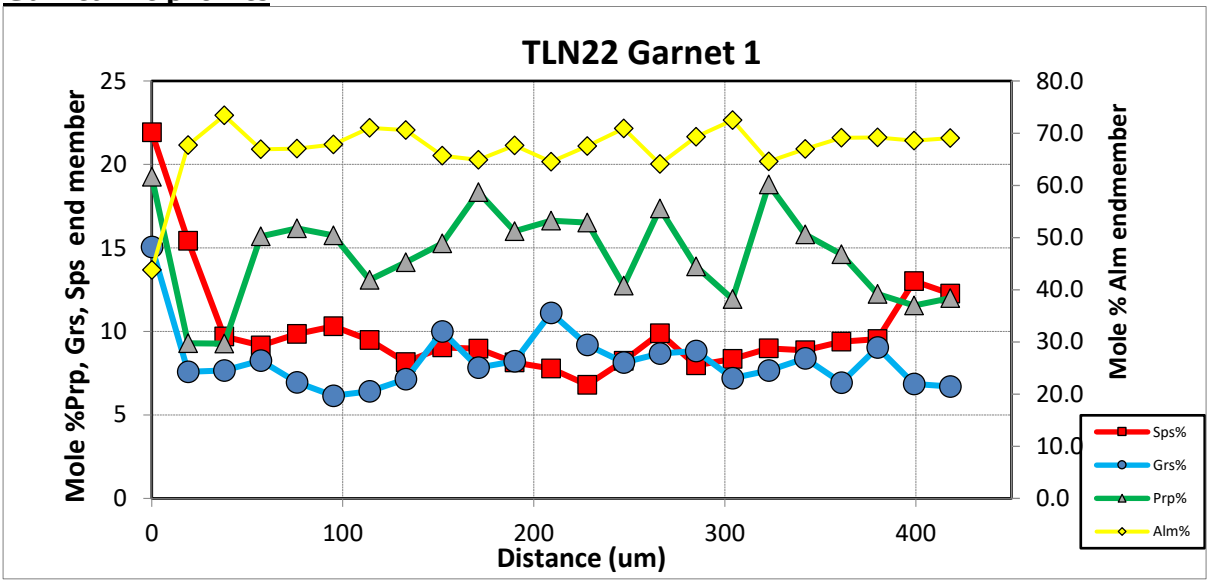

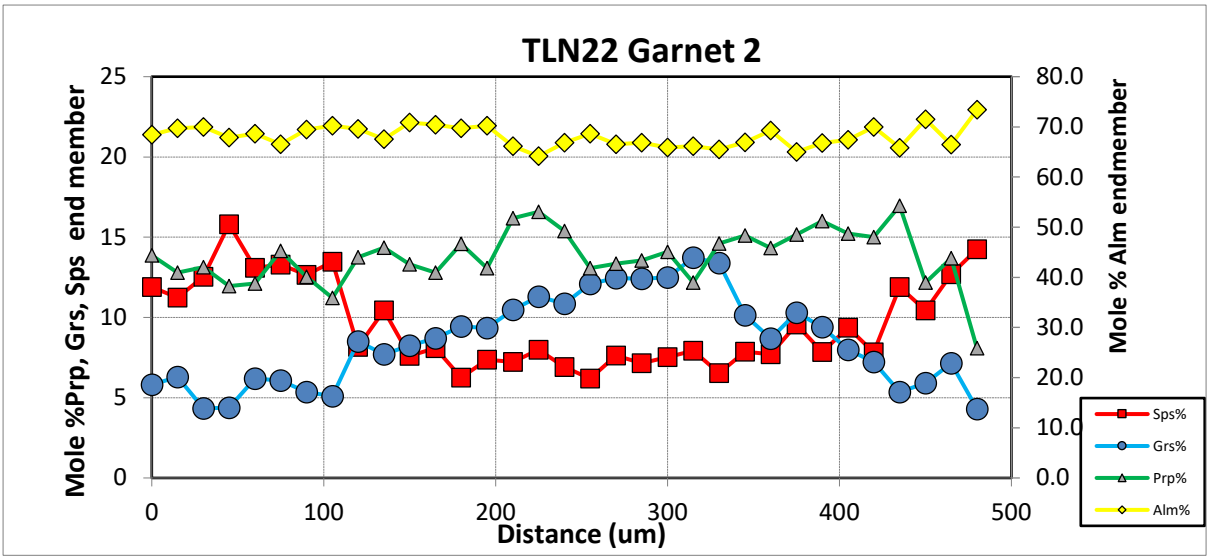

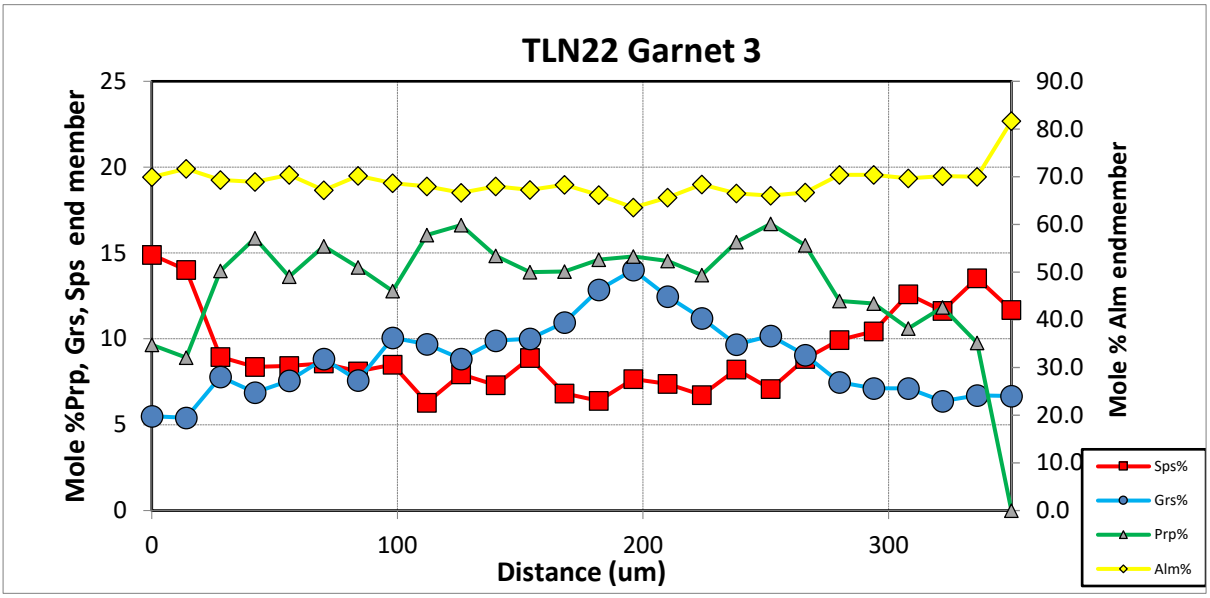

TLN22 garnet line profiles are taken from the small garnets which are inclusion rich and appear to be post-tectonic with the sheared and deformed matrix. These garnets are sometimes engulfed by kyanite but in other places overgrow kyanite suggesting they grew simultaneous to kyanite. They also sometimes appear as isolated fragmets of an older garnet porphyroblsast that has been resorbed and then had growth on the rims of these pre-existing fragments. Overall they preserve a variety of prograde growth zoning with irregular albeit systematic decreases in grossular from core (14-15 %) to rim (5-6%), (profiles 2 and 3) and pyrope has a slight increase towards the inner rim (16-17%) followed by a decrease towards the outer rim (9-12%), which we interpret as both an increase in pressure and temperature during garnet growth. There is a classic diffusion closure profile preserved in the spessartine content in all profiles characteristic of high-grade resorption. Lots of tiny garnets overgrows the shear fabric fabric, indicating late stage increases in garnet volume. Comparison with the pseudosection shows that slight isobaric heating following decompression would result in increases in garnet mode and decrease the volume of muscovite in the sample.

17TL75 Garnet Amphibolite

Garnet line profiles

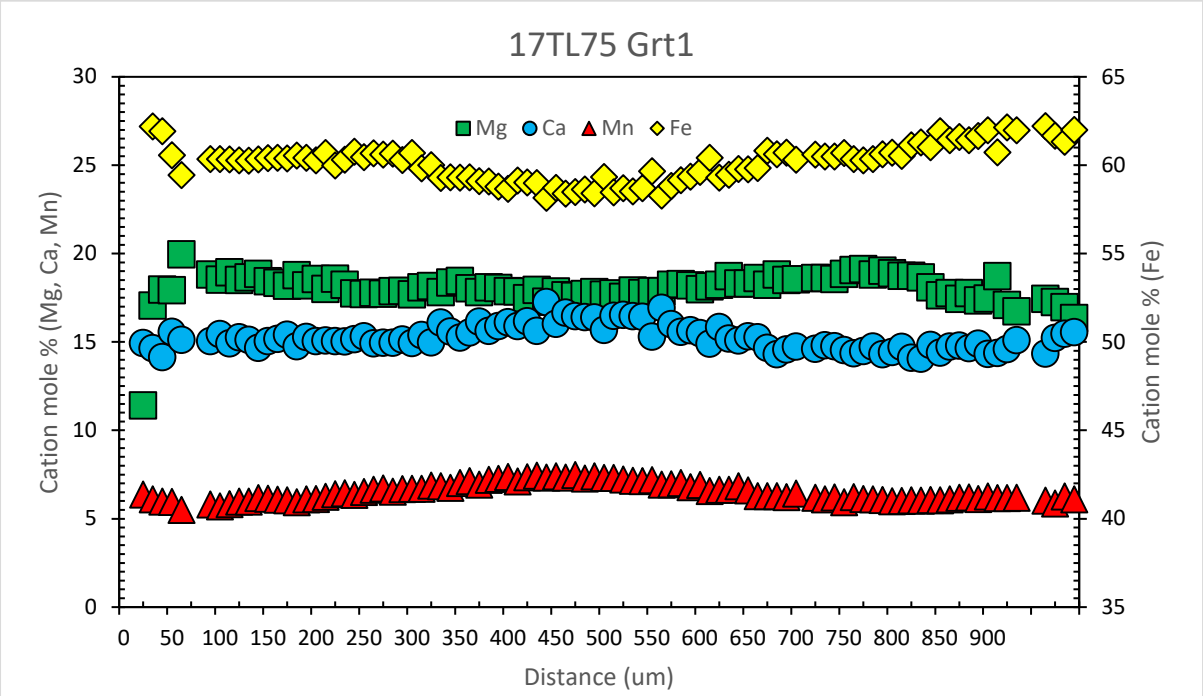

Garnet shows a homogenous flat profile with only an increase of ~1-2% Pyrope from core to rim (17% to 18-20%) associated with a slight decrease in Grossular (17% to 15%) and Spessartine (8% to 5%), due to diffusional re-equilibration. There is a slight inflection in Spessartine and Pyrope towards the outermost 50 microns of the rim that indicates the limited length scale of diffusional alteration of the original profile. We interpret this profile to represent a single stage of garnet growth at or near peak Barrovian metamorphic conditions.

Amphiboles

In 17TL75 Amphiboles are purely of high temperature origin plotting between a pargasite, hornblende and tschermakite composition and form a tight cluster in compositional space, with no data suggesting any belong to an earlier high pressure (M_1) origin. They have variable Fe3+ components between 0.3 and 0.65 as shown in the plots below. We interpret these amphiboles grew during peak M_2 upper amphibolite facies conditions, in equilibrium with garnet, a small degree melt phase and plagioclase with an anothite (x(Ca)) component of 0.3-0.35.

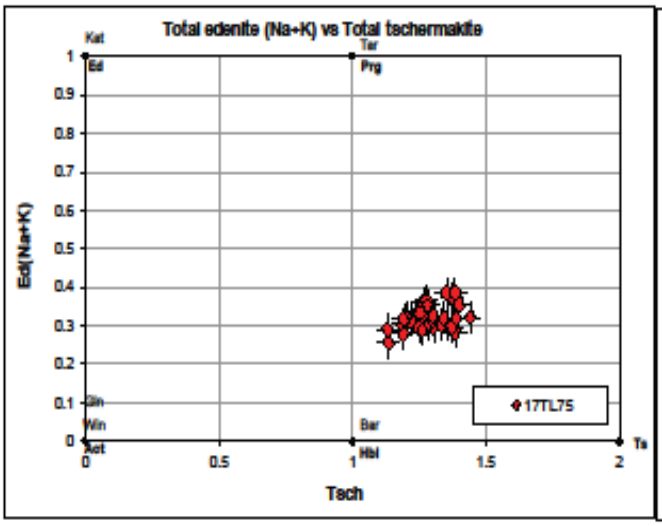
Total edenite (Na+K) vs Total tschermakite
Kat
Ed
Ter
Prg
Gln
Win
Act
Bar
Hbl
Ts
Ed(Na+K)
Tsch
17TL75

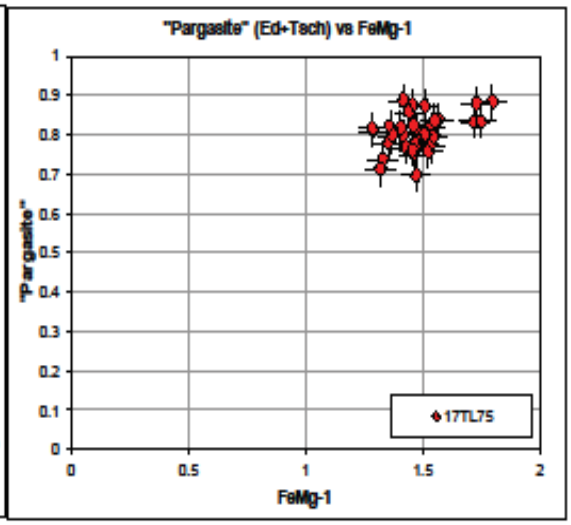
"Pargasite" (Ed+Tsch) vs FeMg-1
"Pargasite"
FeMg-1
17TL75

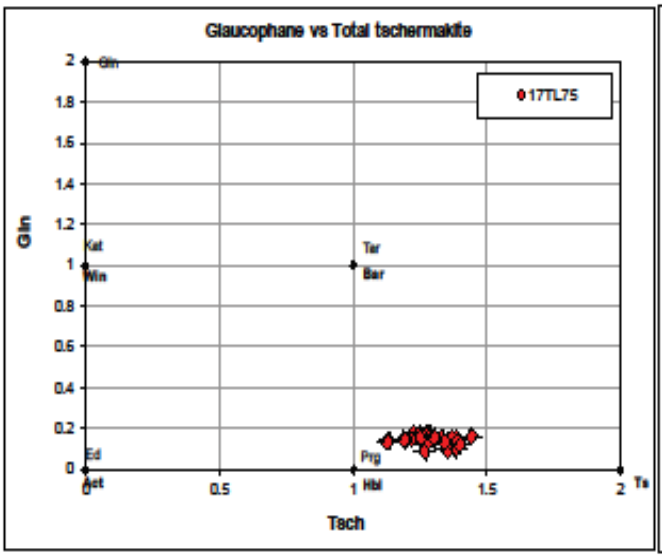
Glaucophane vs Total tschermakite
Gln
Kat
Win
Ter
Bar
Ed
Act
Prg
Hbl
Ts
Tsch
17TL75

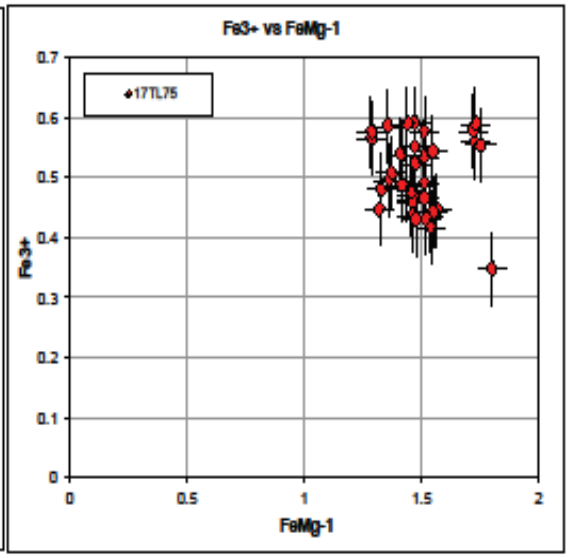
Fe3+ vs FeMg-1
Fe3+
FeMg-1
17TL75

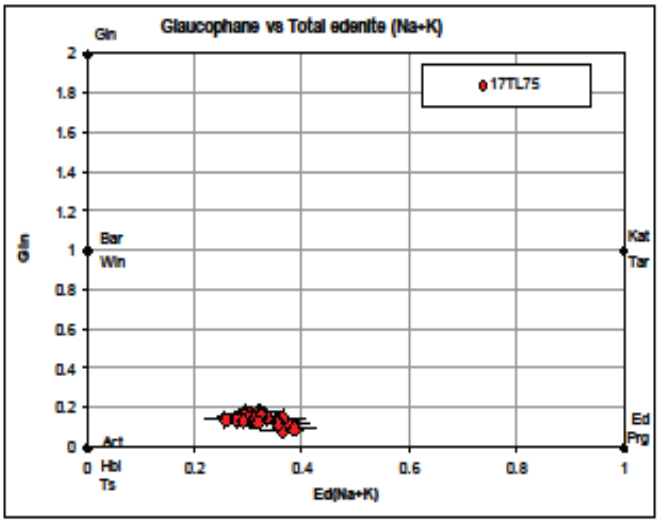
Glaucophane vs Total edenite (Na+K)
Gln
Bar
Win
Kat
Ter
Act
Ed
Prg
Hbl
Ts
Ed(Na+K)
17TL75

3.5 Core Unit

White mica, primary and secondary muscovites

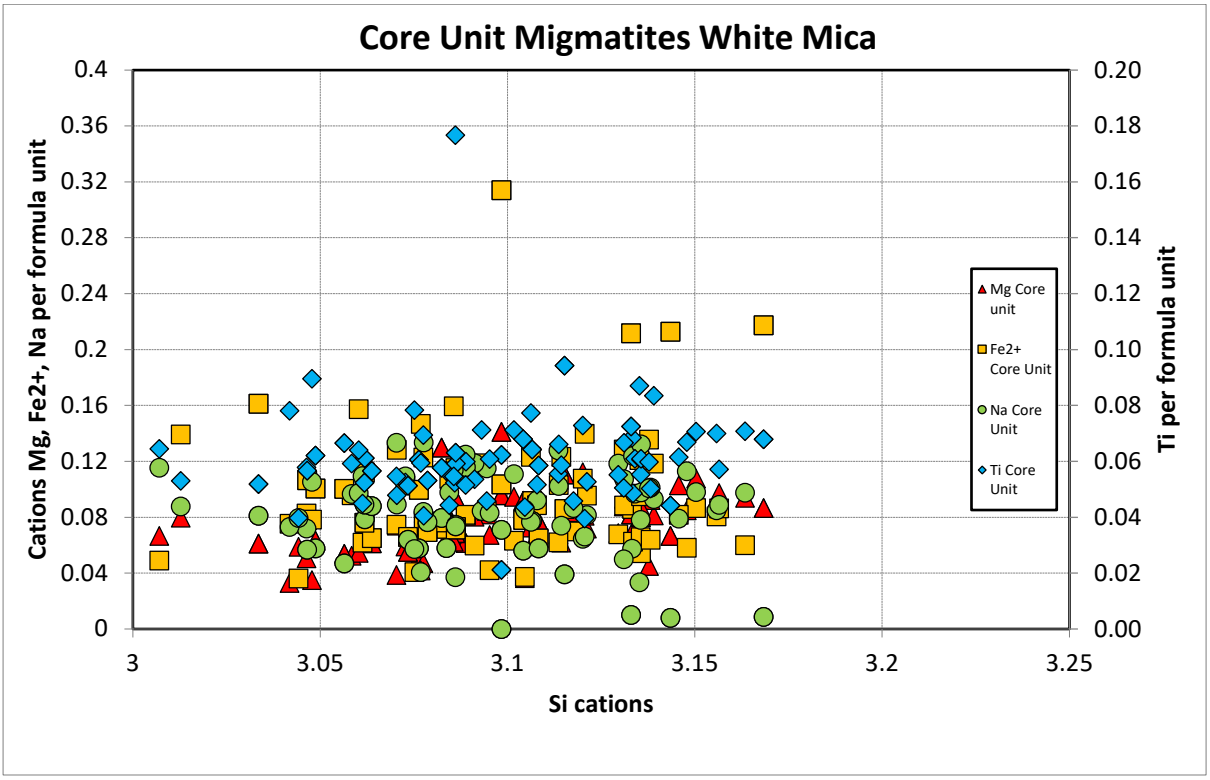

Figure 3.5.1 Core Unit white mica cations per unit formula (11 oxygens) plots against Si cations showing a range between primary muscovite and secondary consistent with the interpretation of kyanite grade hydrous melting is the dominant process and muscovite dehydration melting only occurred at deep structural levels.

White mica compositions from Core Unit show mild to moderate variation in cation end members and are clustered with overall Si of <3.17 p.f.u. and moderate to high amounts of Ti (0.04-0.10 p.f.u.) characteristic of high grade muscovite. Some inference into the temperature of mineral growth can be made with compositional characteristics of different mineral generations. Prograde muscovite commonly contains higher paragonite (Na) content than retrograde muscovite that has replaced K-feldspar (Evans and Guidotti, 1966; Ashworth, 1975). Generally, low Si content (<3.10 cpfu per 11-oxygens) combined with high Ti content (up to 0.08 cpfu) is characteristic of high-grade and magmatic muscovite (Miller et al., 1981; Guidotti, 1984). In all analysed samples, leucosome muscovite is low in Si and contains a moderate-high Ti content (~0.04-0.10), indicating that they formed during melt crystallization or retrogressively while still at high-temperature.

3.5.1 TL15

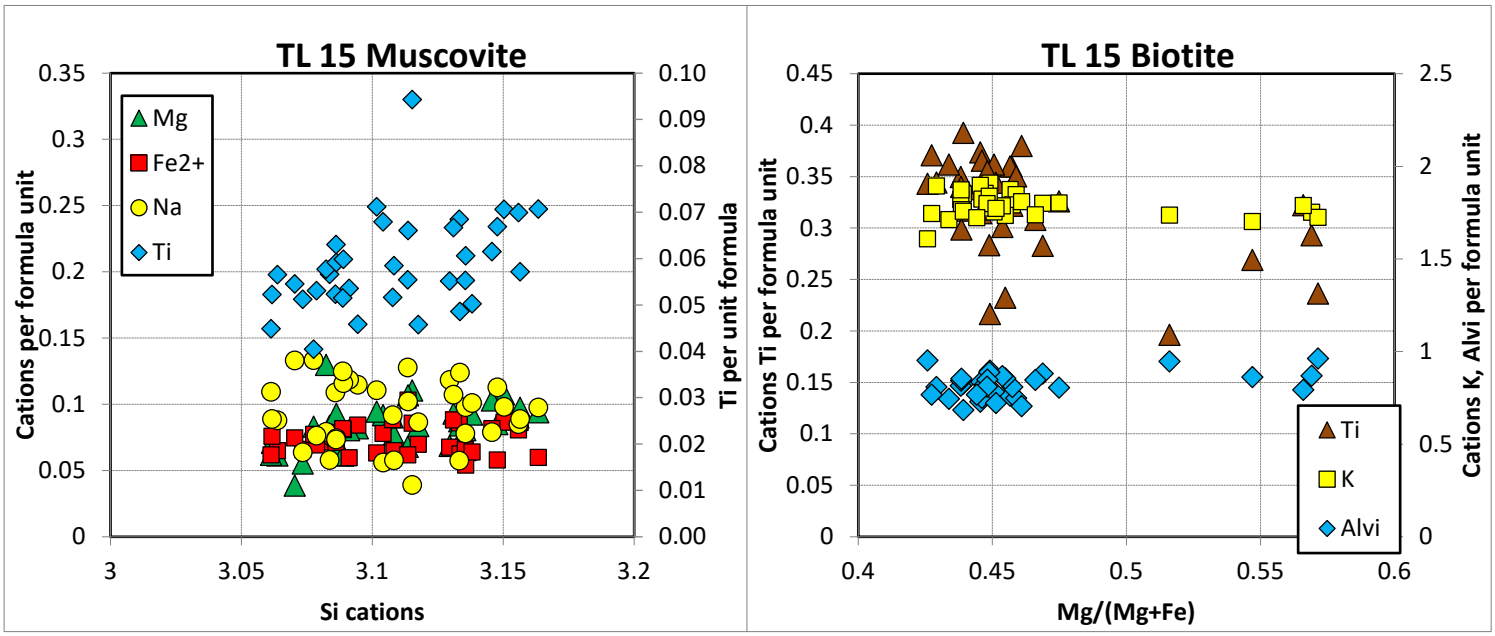

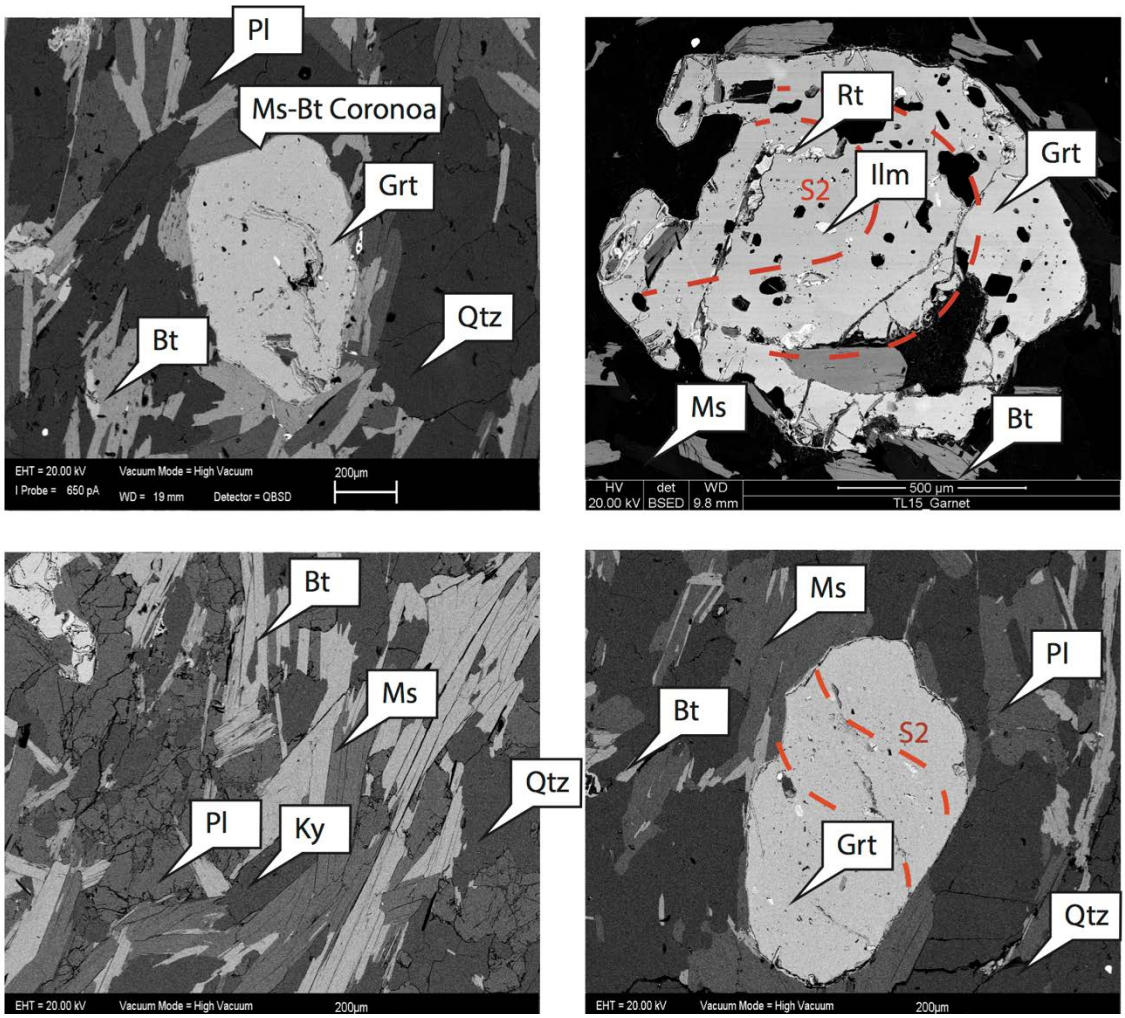

Figure 3.5.1.1 Representative SEM images of TL15 showing the preservation of an earlier S_2 fabric within garnet that is discordant to the external matrix fabric. Kyanite is folded with the S_3 foliation suggesting it was pre-tectonic with respect to upright F_3 folding. Some primary muscovite is preserved but not much indicating the rock never crossed the muscovite dehydration melting reaction.

Garnet Maps

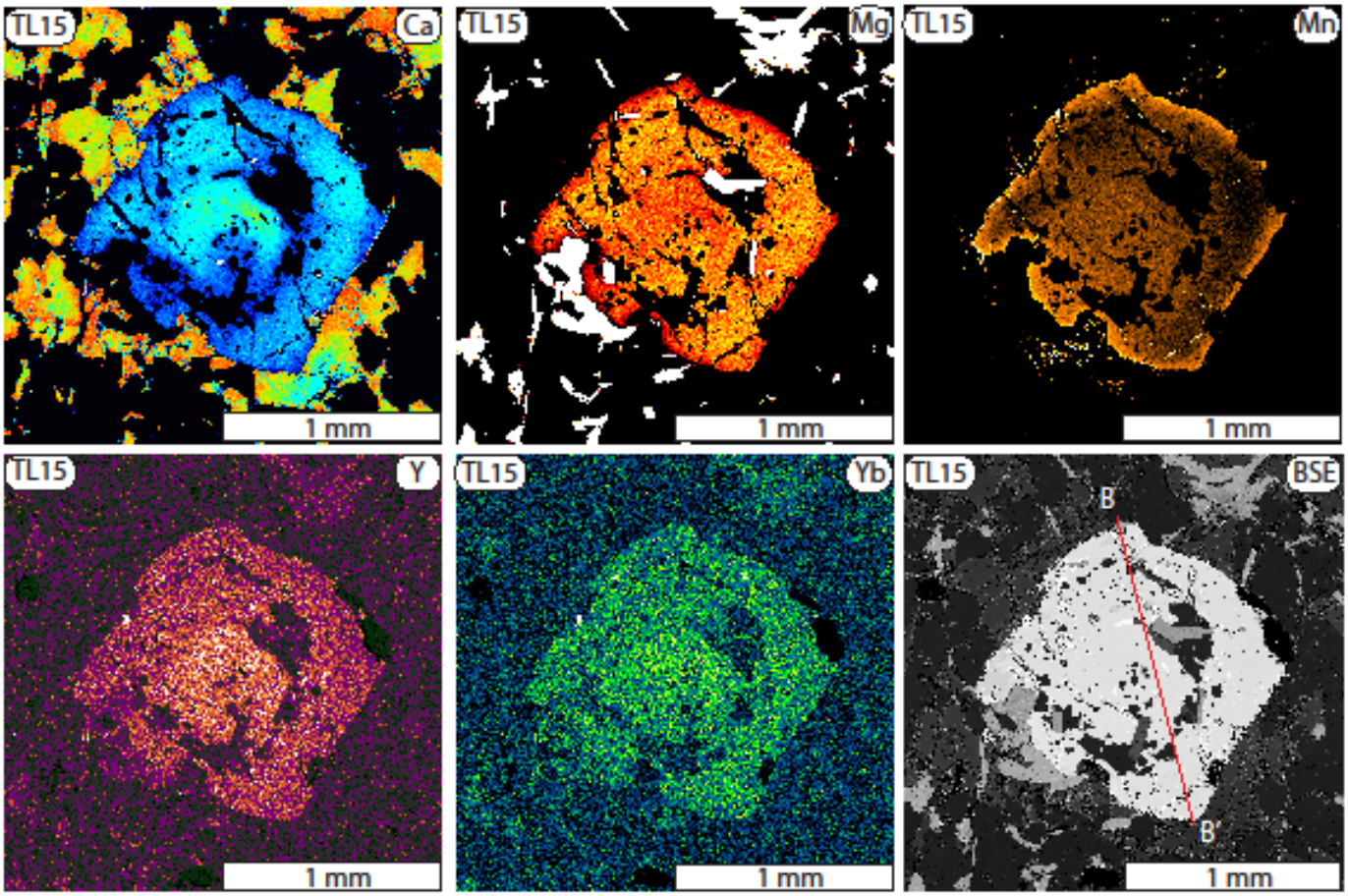

Garnet line profiles

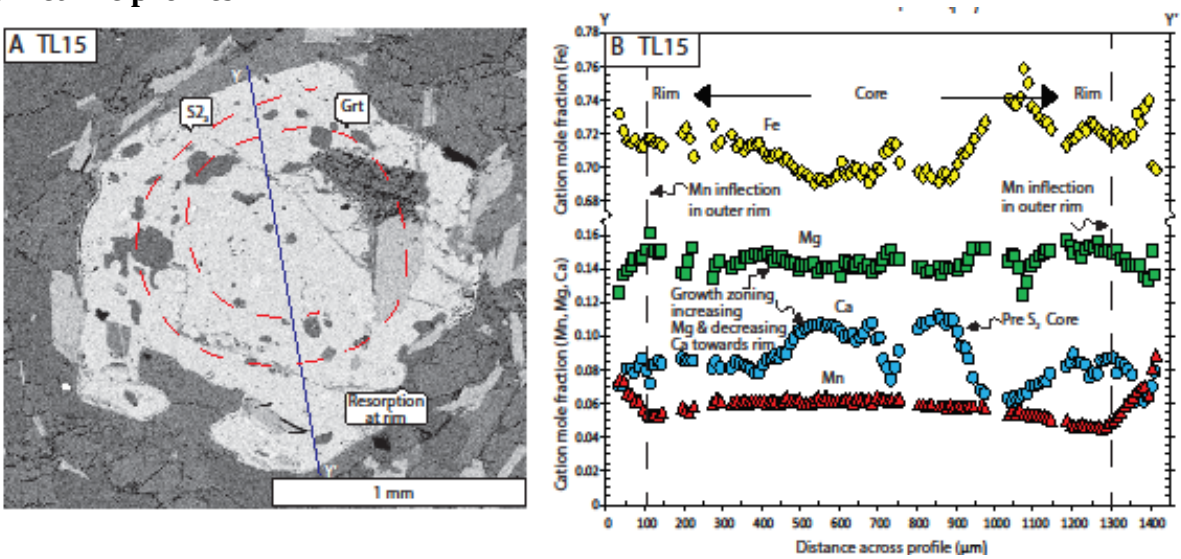

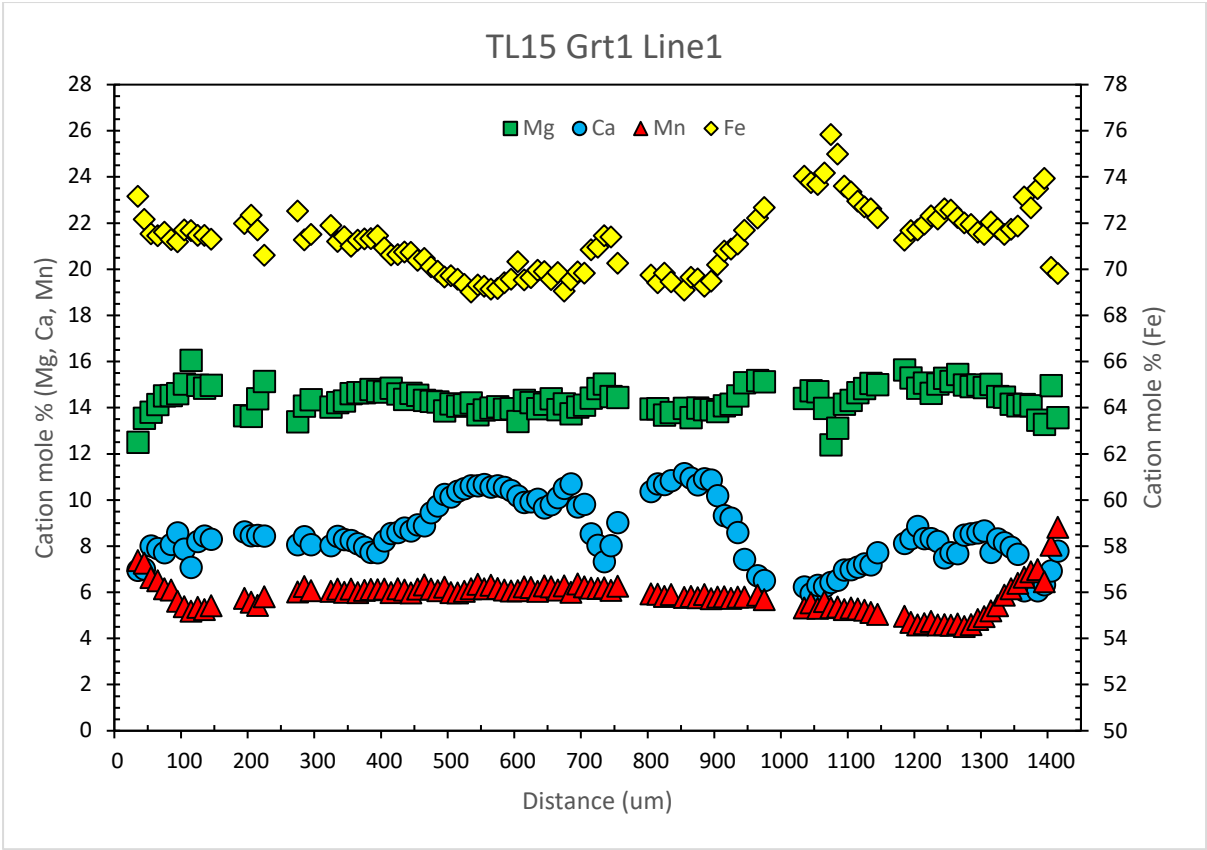
TL15 Grt1 Line1
Mg
Ca
Mn
Fe
Cation mole % (Mg, Ca, Mn)
Cation mole % (Fe)
Distance (um)

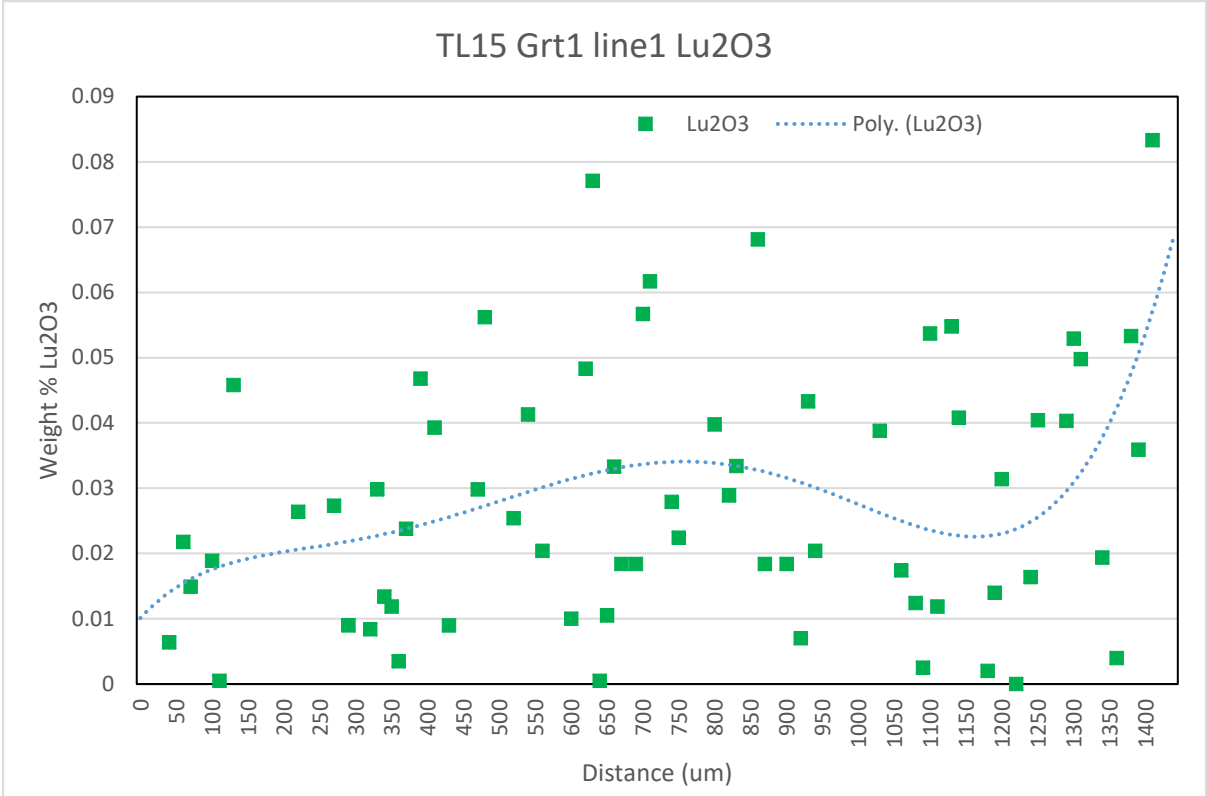
TL15 Grt1 line1 Lu2O3
Lu2O3
Poly. (Lu2O3)
Weight % Lu2O3
Distance (um)

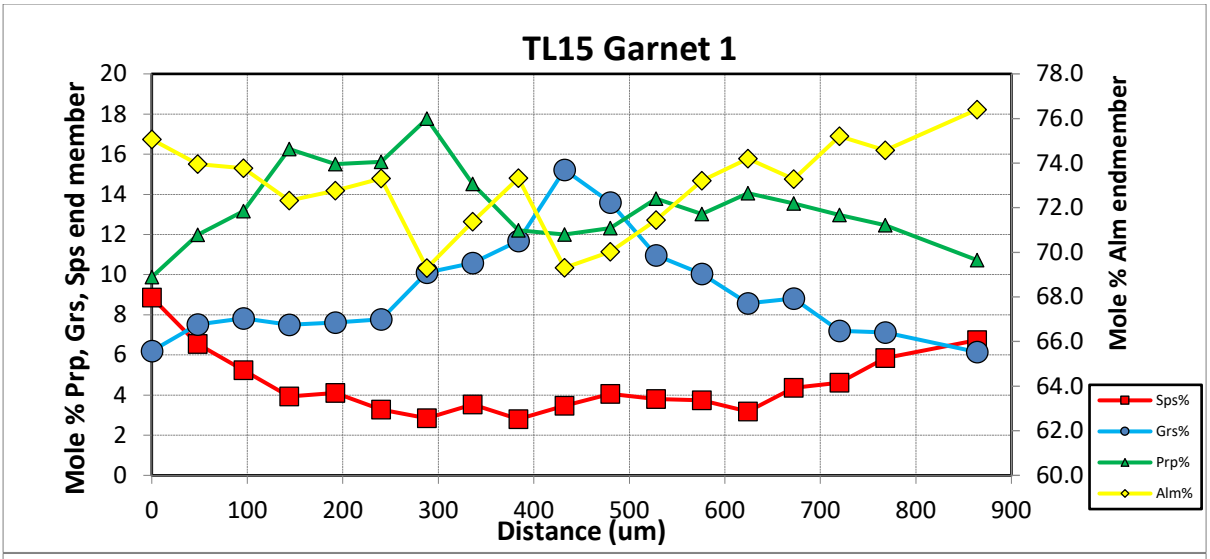

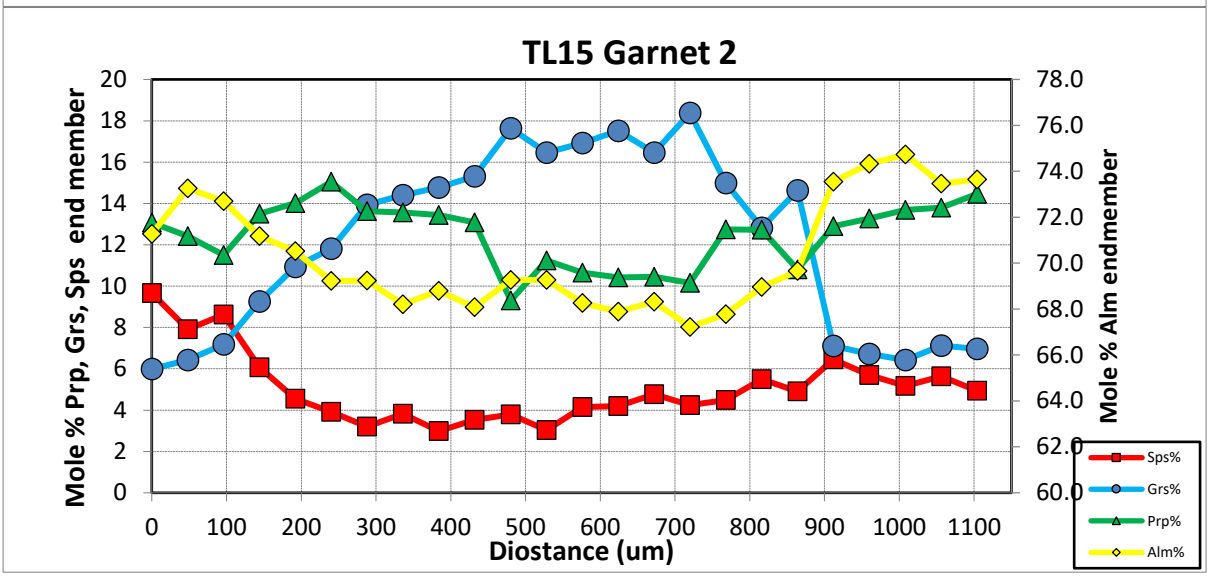

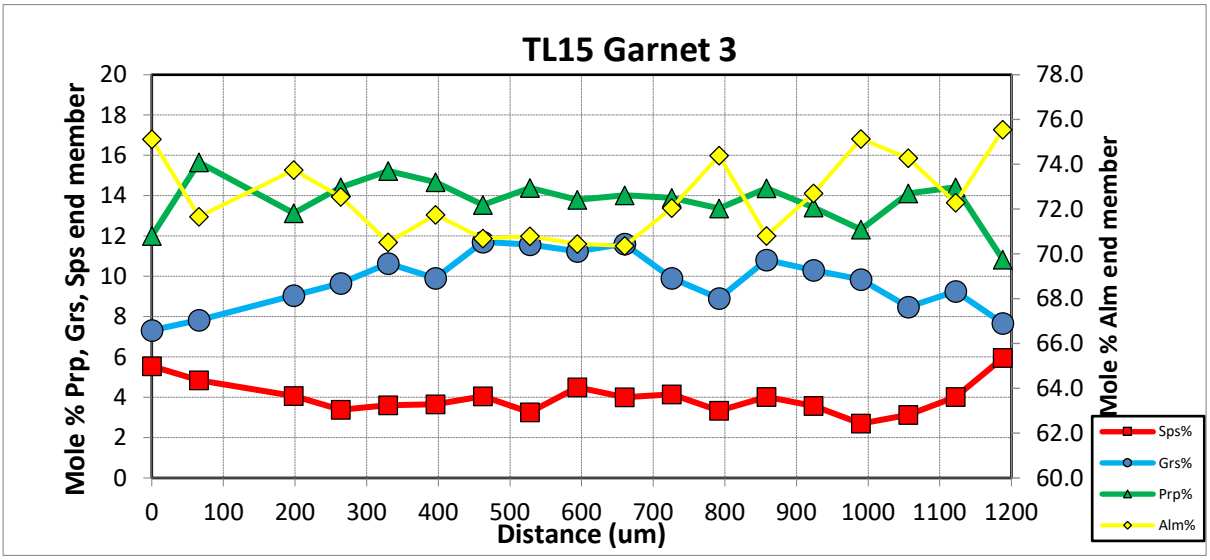

TL15 Garnet profiles show a mixture of flat homogenised profiles to preserving a central peak in Ca (grossular), that decreases towards the rim. This is interpreted as

preserving evidence of prograde metamorphism associated with increases in both pressure and temperature during garnet growth. There is an increase in Mg (pyrope) preserved in some profiles related to dominantly increases in temperature and a classic increase in Mn (spessartine) towards the rim indicative of garnet resorption at high grade.

3.5.2 TL66

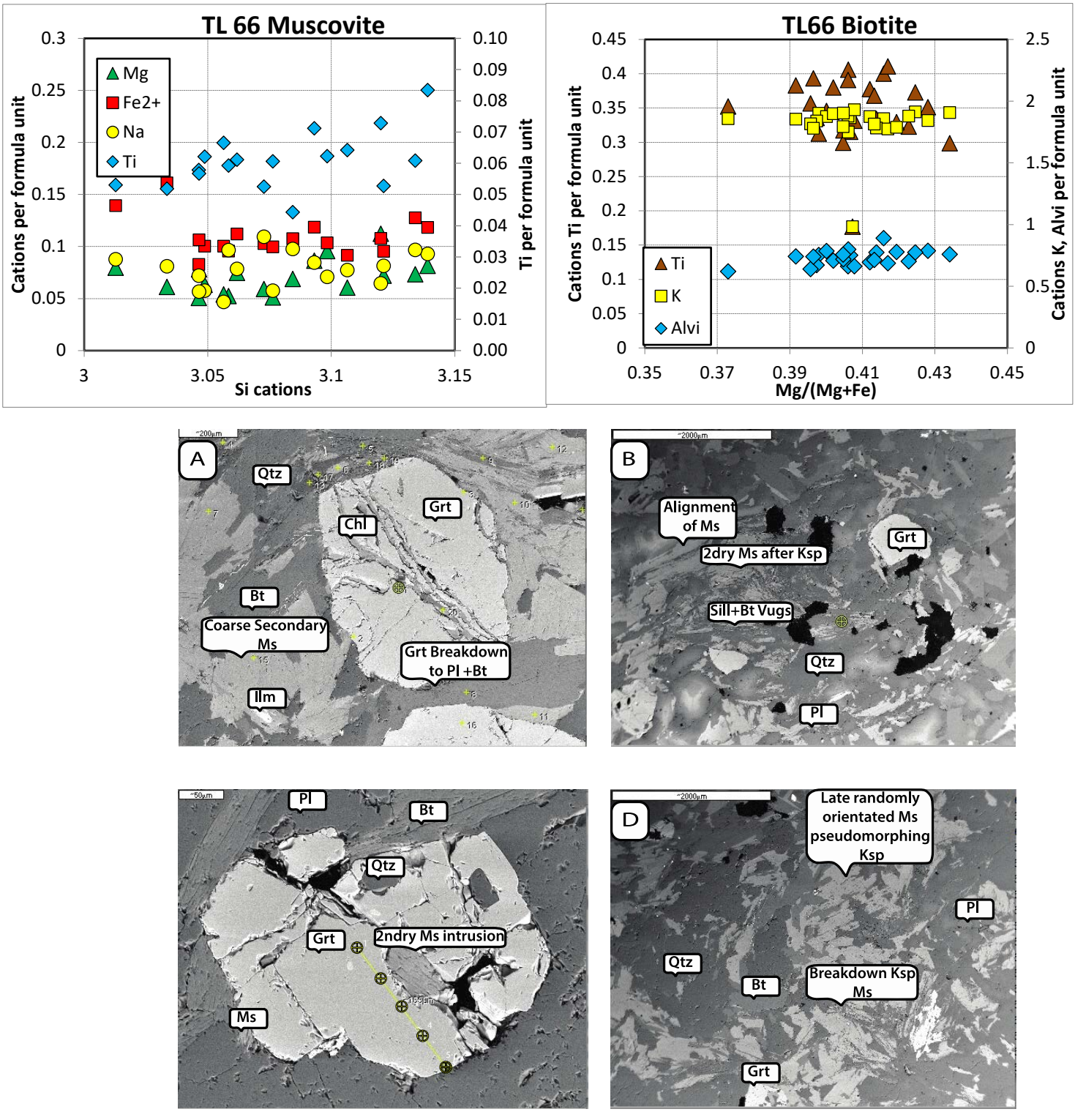

Figure 3.5.2.1 Backscattered SEM images of TL66 showing the intense cross cutting late secondary muscovite and resorption on garnet. Sillimanite+ biotite is defined with interstitial quartz in the melanosome that represents a "faserkiesel" texture, indicative of breakdown of muscovite and production of sillimanite during anatexis. Due to the intensity of coarse secondary muscovite and the lack of K-feldspar, it is likely that this rock crossed the muscovite dehydration melting reaction, however most of the melt remained in communication with the rock, reconverting k-feldspar to muscovite.

Garnet line profiles

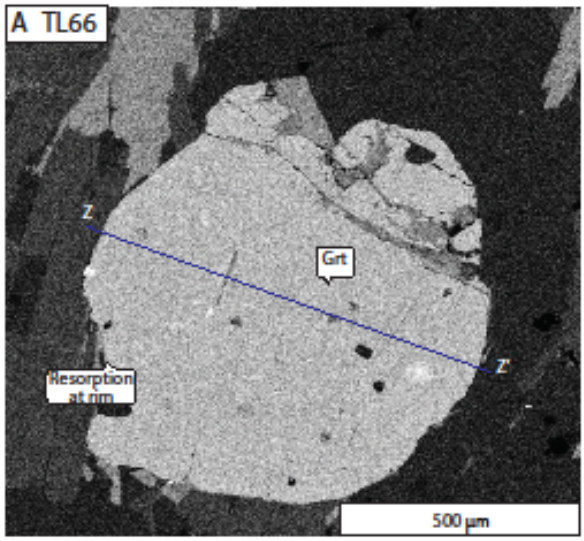

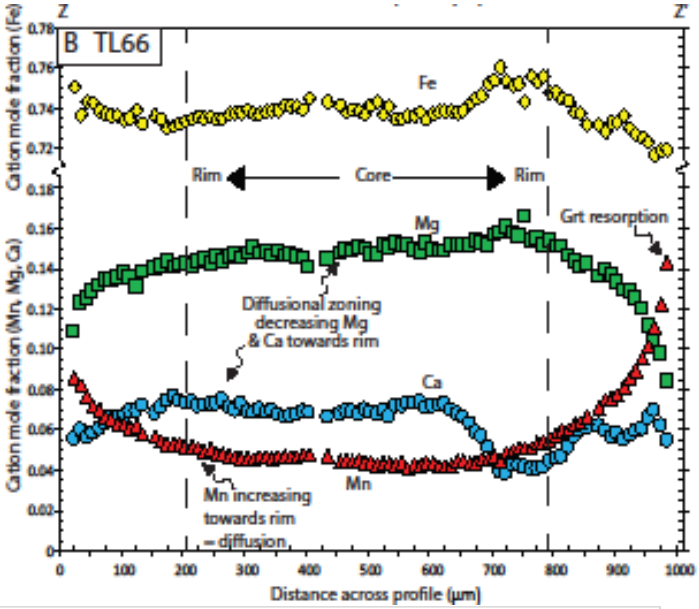

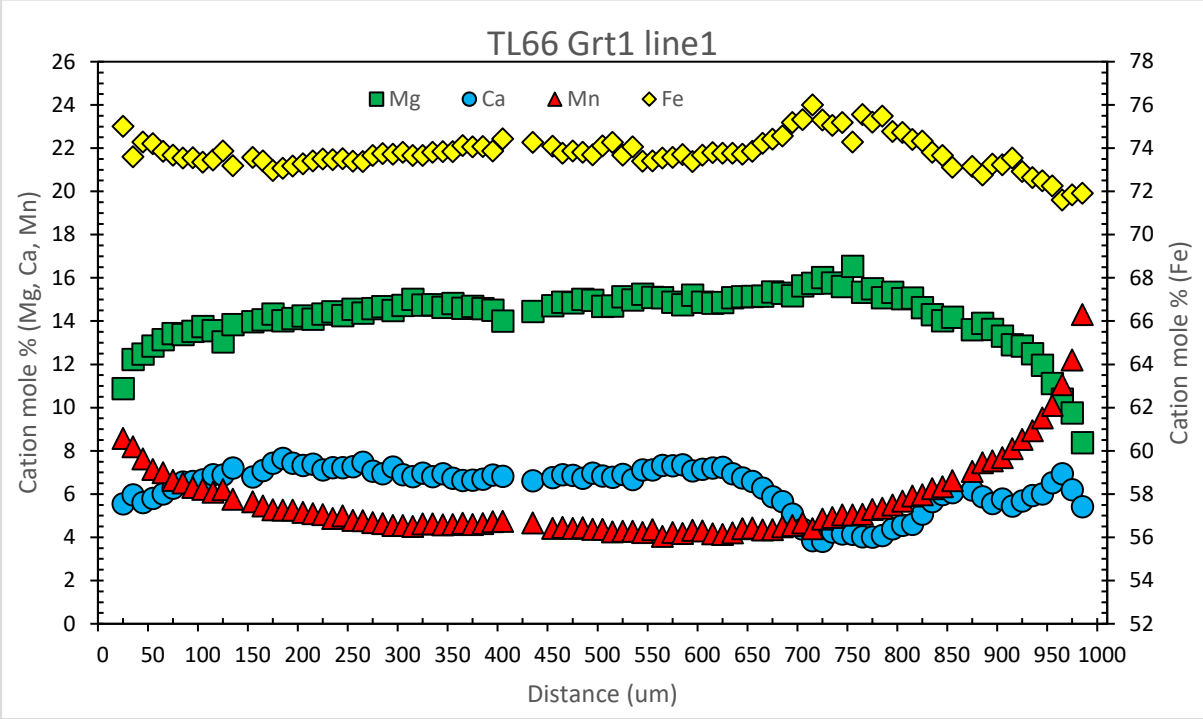

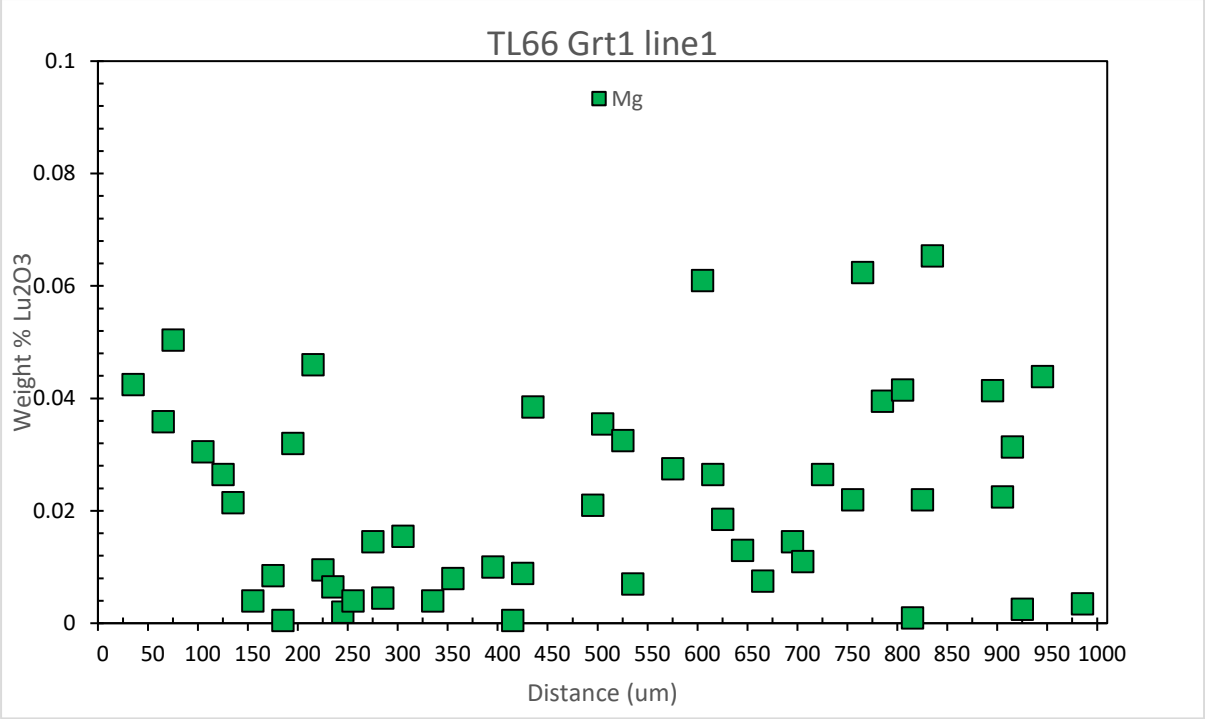
TL66 Grt1 line1
Mg
Weight % Lu2O3
0.1
0.08
0.06
0.04
0.02
0
0 50 100 150 200 250 300 350 400 450 500 550 600 650 700 750 800 850 900 950 1000
Distance (um)

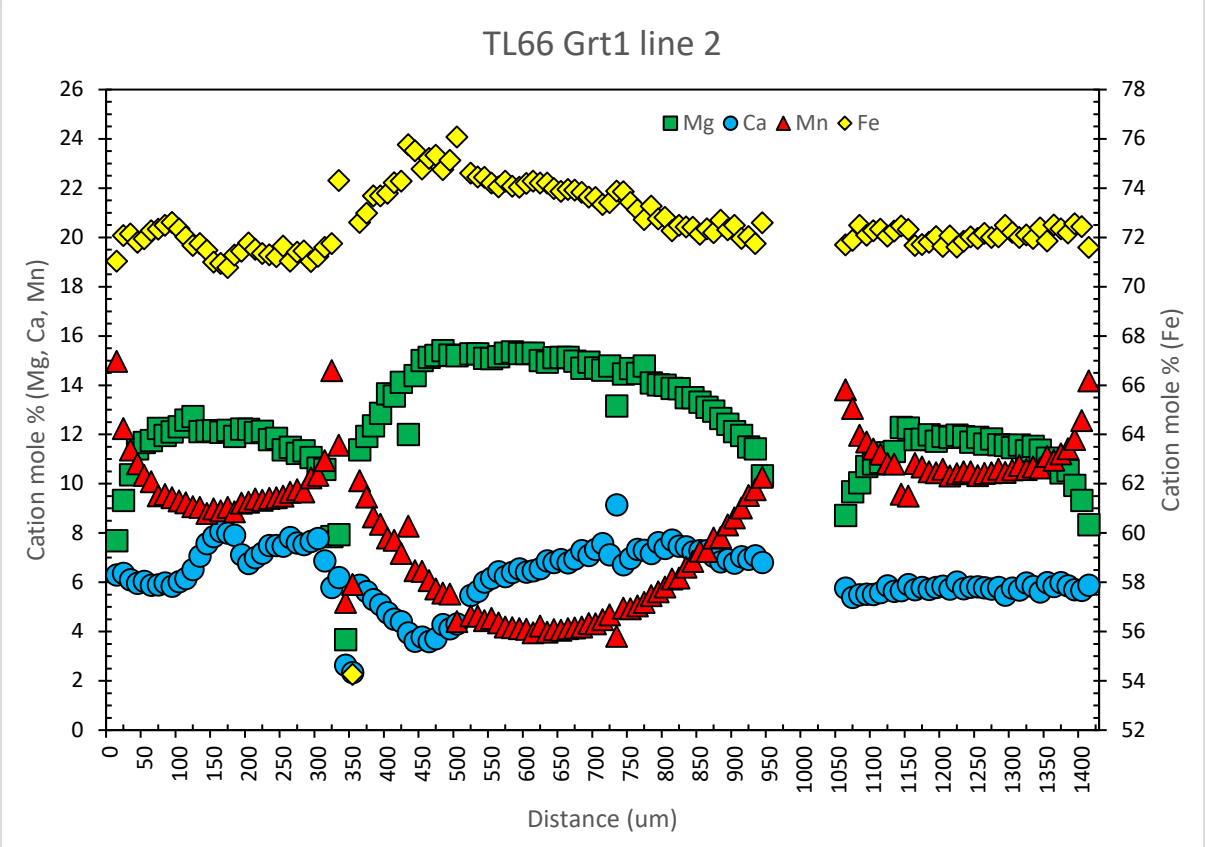
TL66 Grt1 line 2
Mg Ca Mn Fe
Cation mole % (Mg, Ca, Mn)
Cation mole % (Fe)
26
24
22
20
18
16
14
12
10
8
6
4
2
0
78
76
74
72
70
68
66
64
62
60
58
56
54
52
0 50 100 150 200 250 300 350 400 450 500 550 600 650 700 750 800 850 900 950 1000 1050 1100 1150 1200 1250 1300 1350 1400
Distance (um)

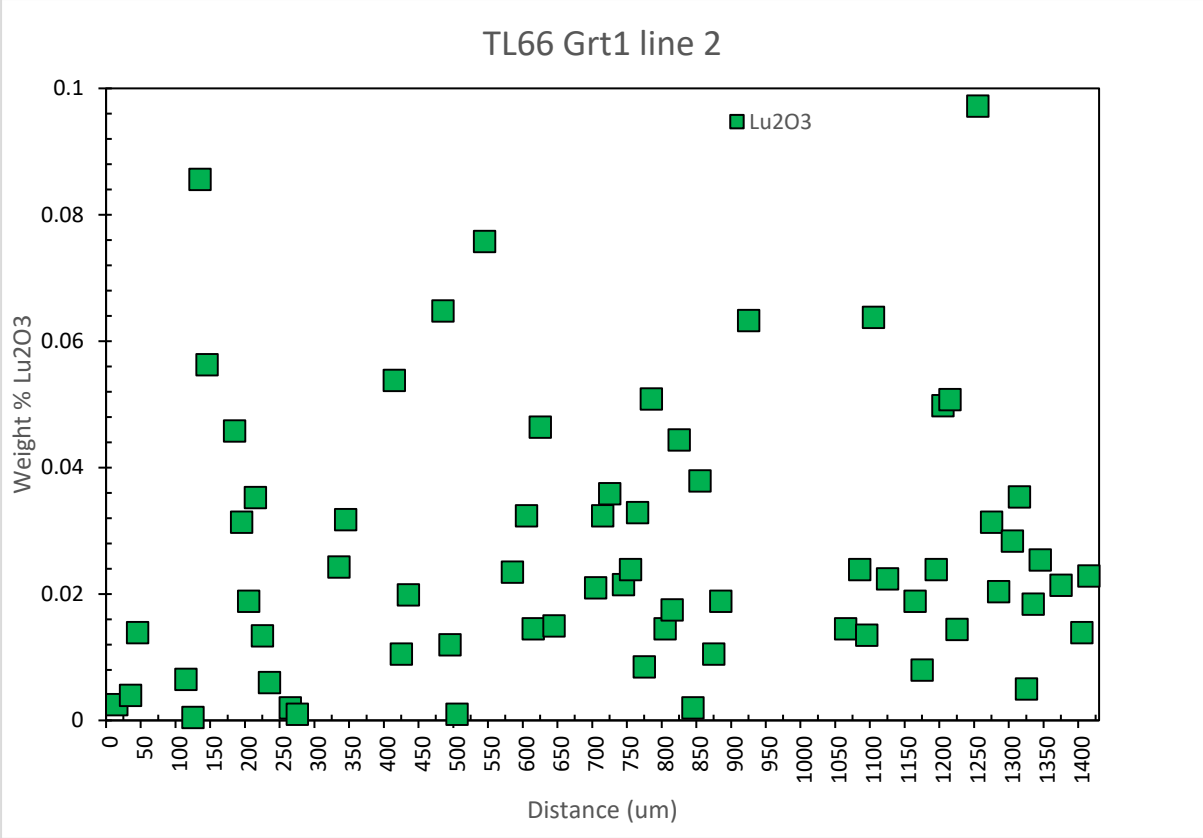
TL66 Grt1 line 2
Lu2O3
Weight % Lu2O3
0.1
0.08
0.06
0.04
0.02
0
0
50
100
150
200
250
300
350
400
450
500
550
600
650
700
750
800
850
900
950
1000
1050
1100
1150
1200
1250
1300
1350
1400
Distance (um)

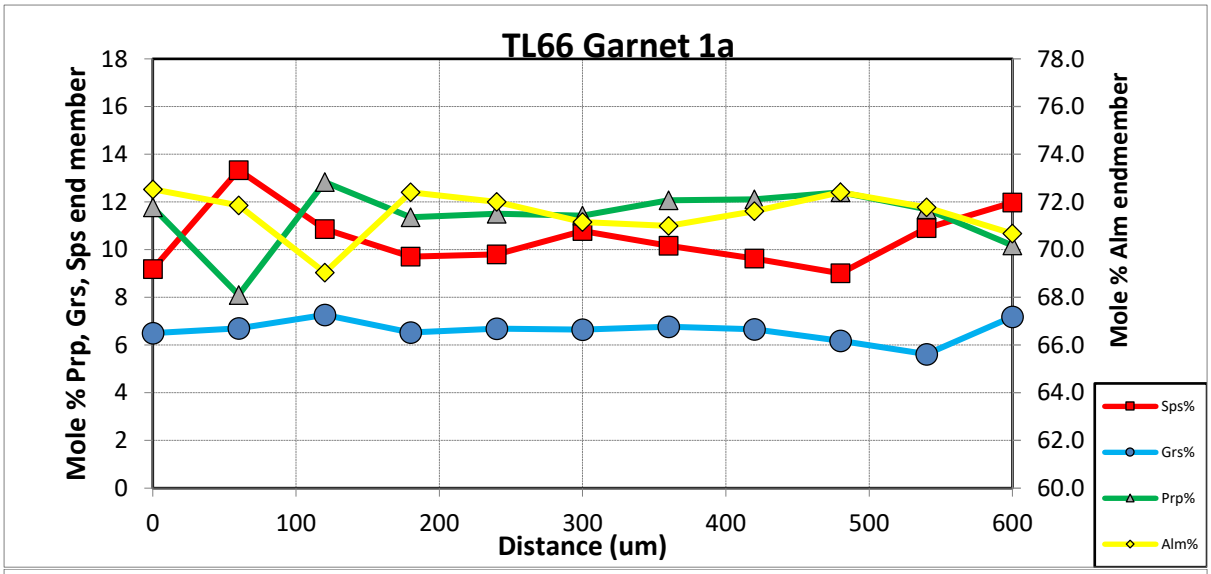
TL66 Garnet 1a
Mole % Prp, Grs, Sps end member
Mole % Alm endmember
Distance (um)
Sps%
Grs%
Prp%
Alm%

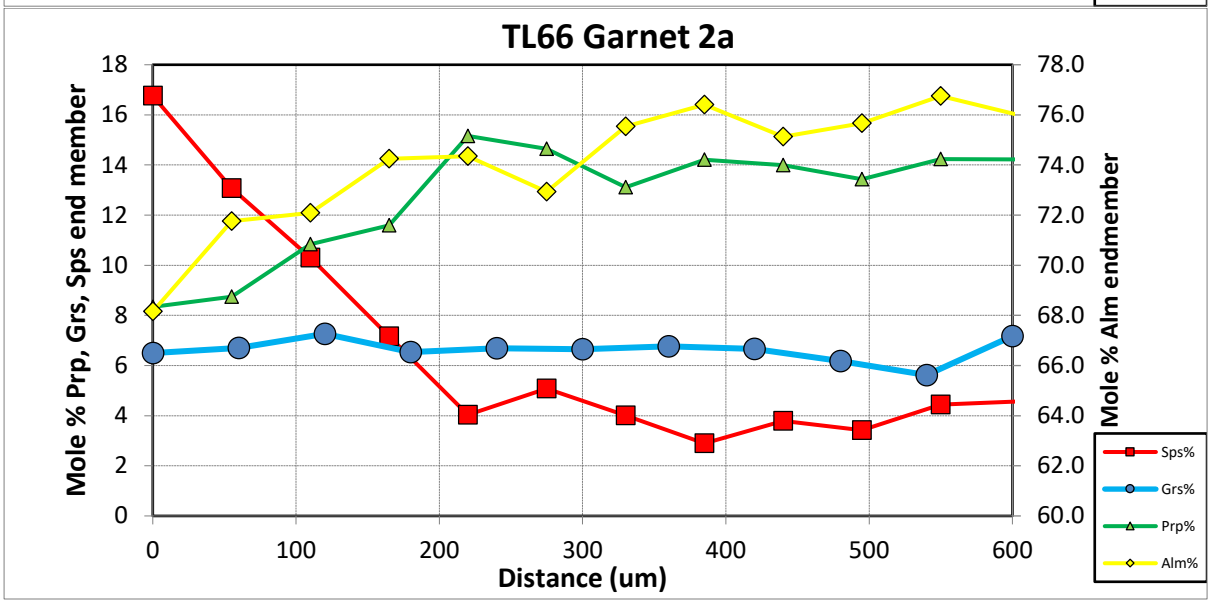
TL66 Garnet 2a
Mole % Prp, Grs, Sps end member
Mole % Alm endmember
Distance (um)
Sps%
Grs%
Prp%
Alm%

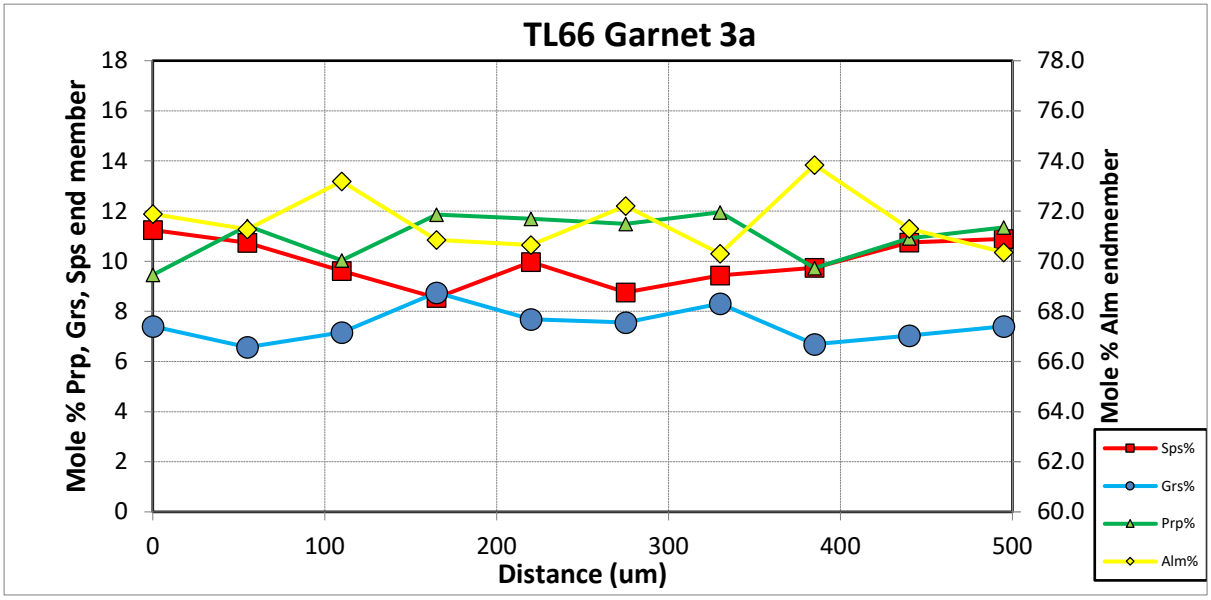
TL66 Garnet 3a
Mole % Prp, Grs, Sps end member
Mole % Alm endmember
Distance (um)
Sps%
Grs%
Prp%
Alm%

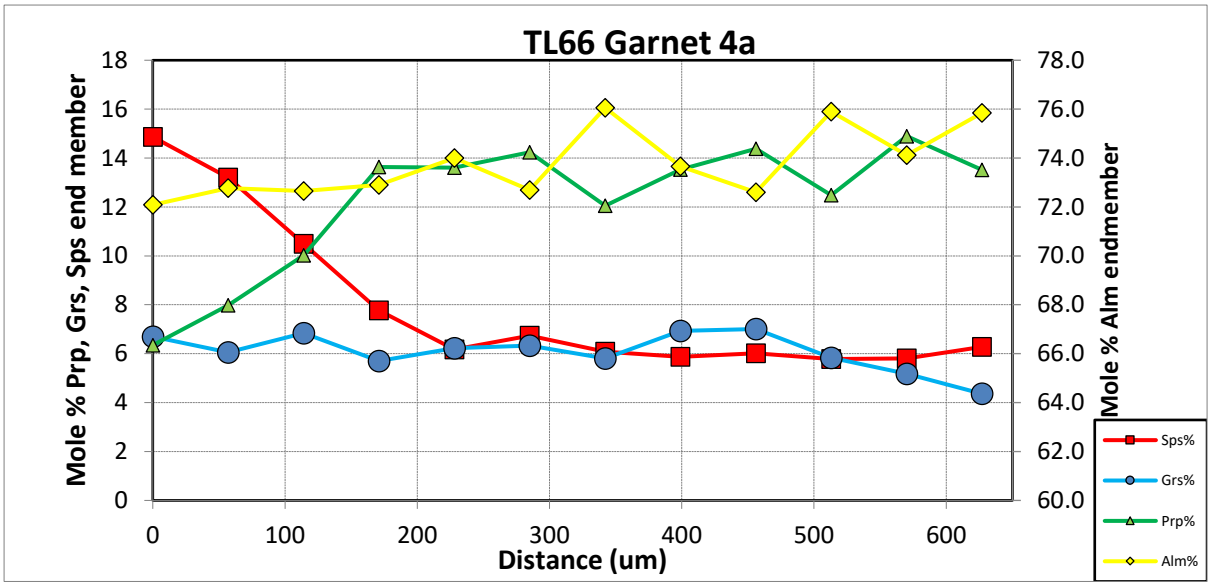
TL66 Garnet 4a
Mole % Prp, Grs, Sps end member
Mole % Alm endmember
Distance (um)
Sps%
Grs%
Prp%
Alm%

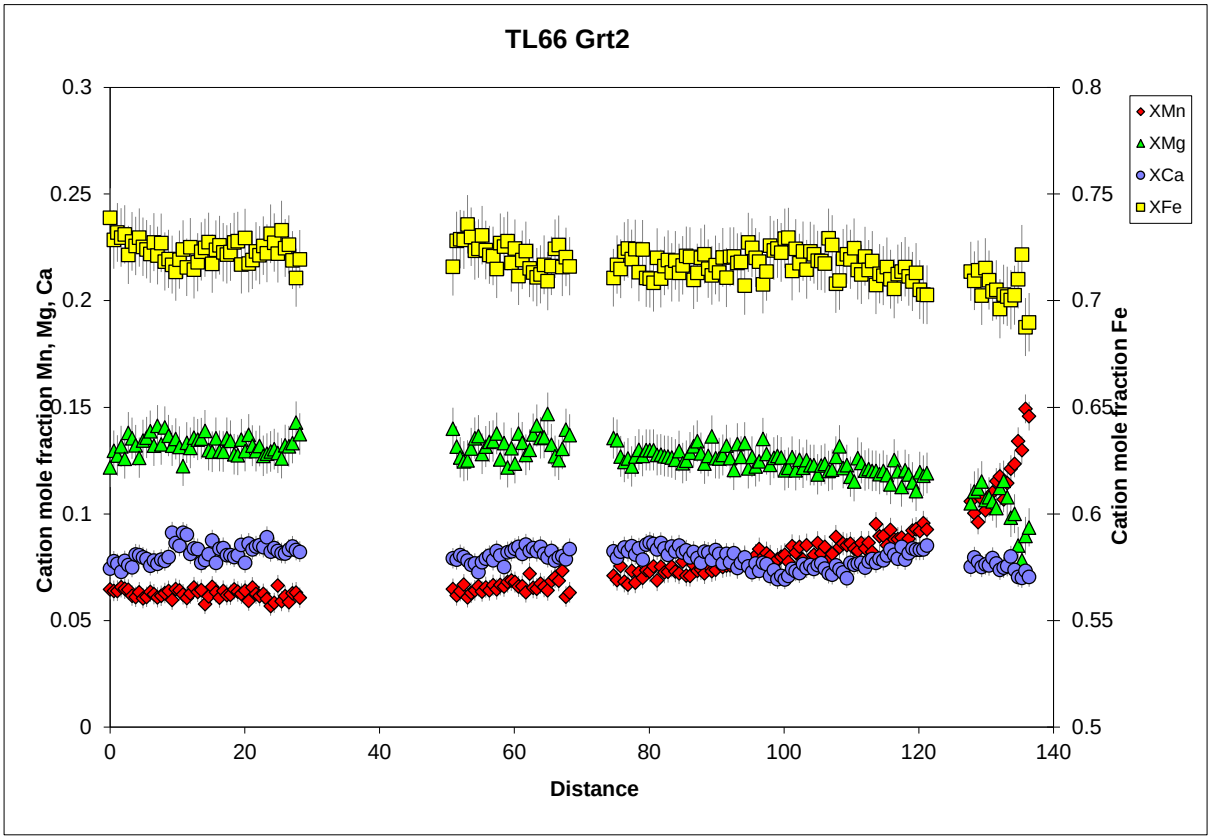
TL66 Grt2
Cation mole fraction Mn, Mg, Ca
Cation mole fraction Fe
Distance
XMn
XMg
XCa
XFe

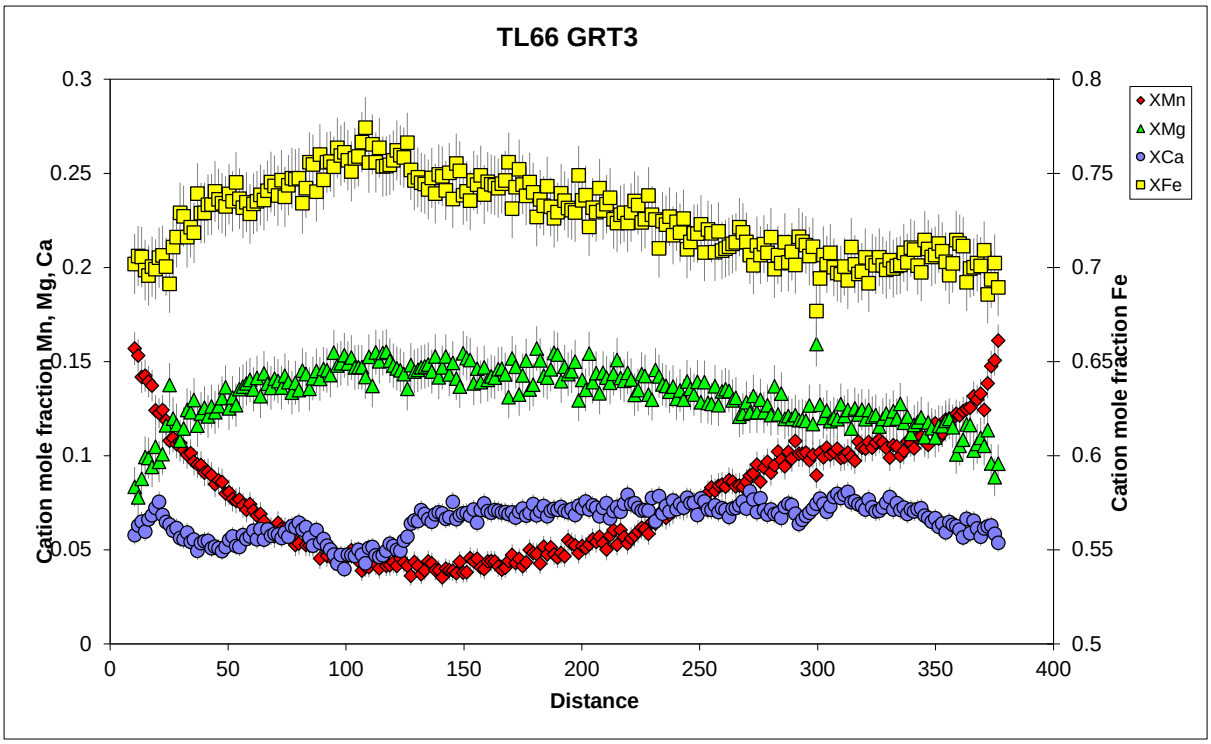

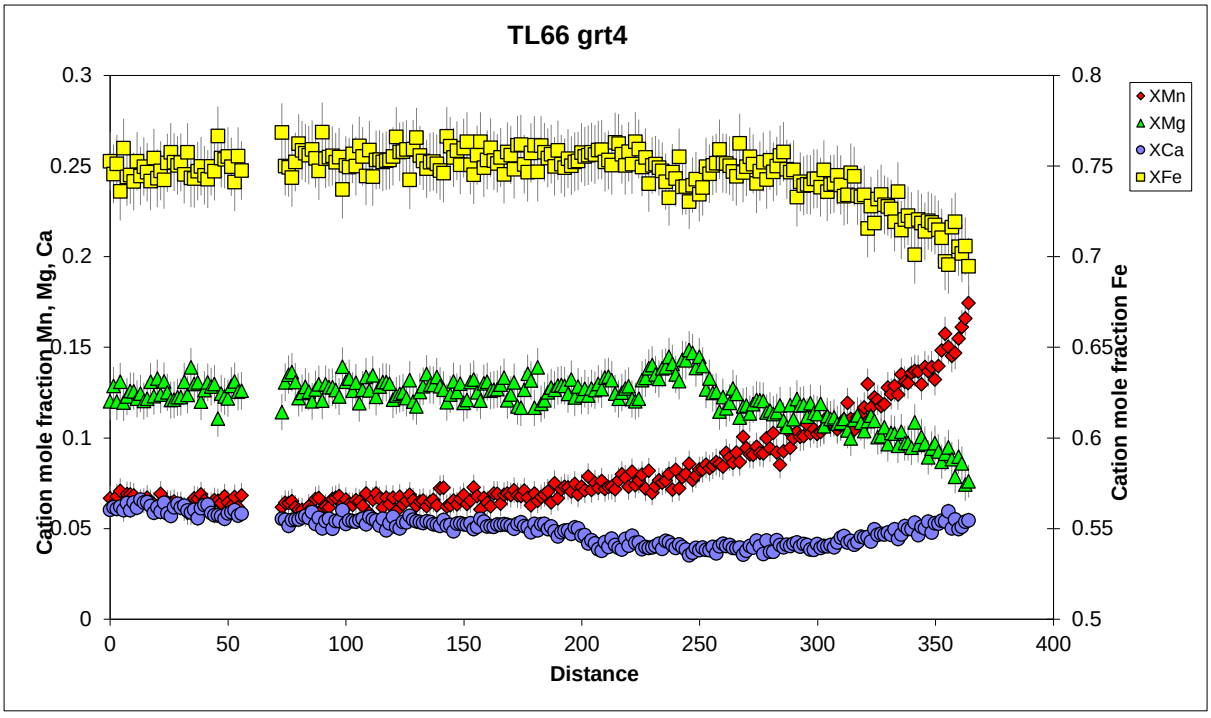

TL66 garnets show homogenization profiles from core to rim which we interpret as growth in the presence of melt and high temperatures. They show core values of 14-15% pyrope and ~ 8% grossular whilst at the rim pyrope decreases to ~8% whereas grossular remains constant or slightly decreases to around 6%. We interpret these patterns as decreases in pressure during garnet growth. Correlating garnet composition with the pseudosection suggests decompression from around 7 kbars to 5.5 kbars at ~720 °C.

3.5.3 TL59

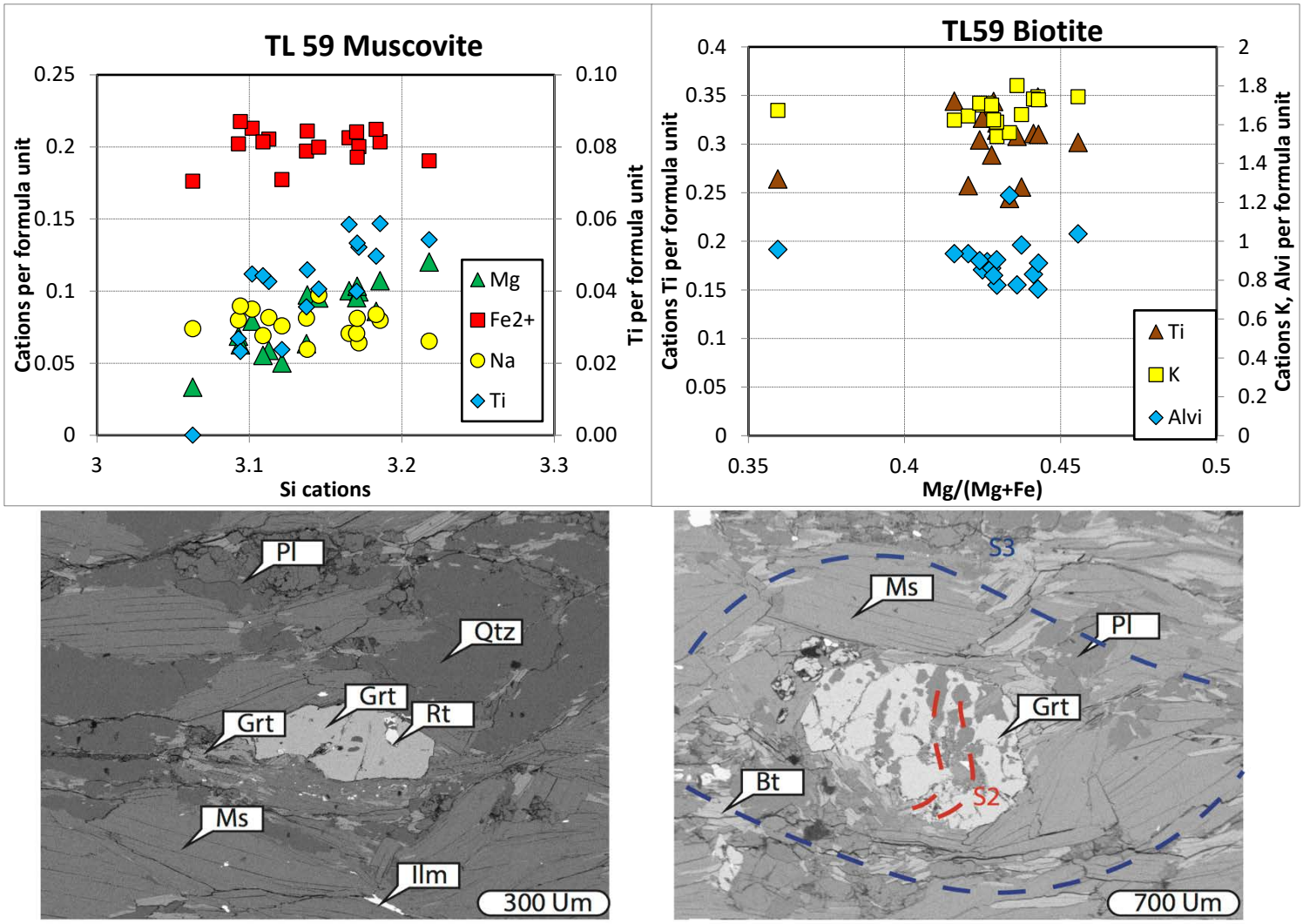

Figure 3.5.3.1SEM images of TL59, showing early S_2 inclusion trails discordant to S_3 and wrapped by coarse secondary muscovite. No kyanite within this sample although rutile inclusions can be preserved witin garnet suggesting this rock experienced M_2 kyanite grade conditions.

Garnet line profiles

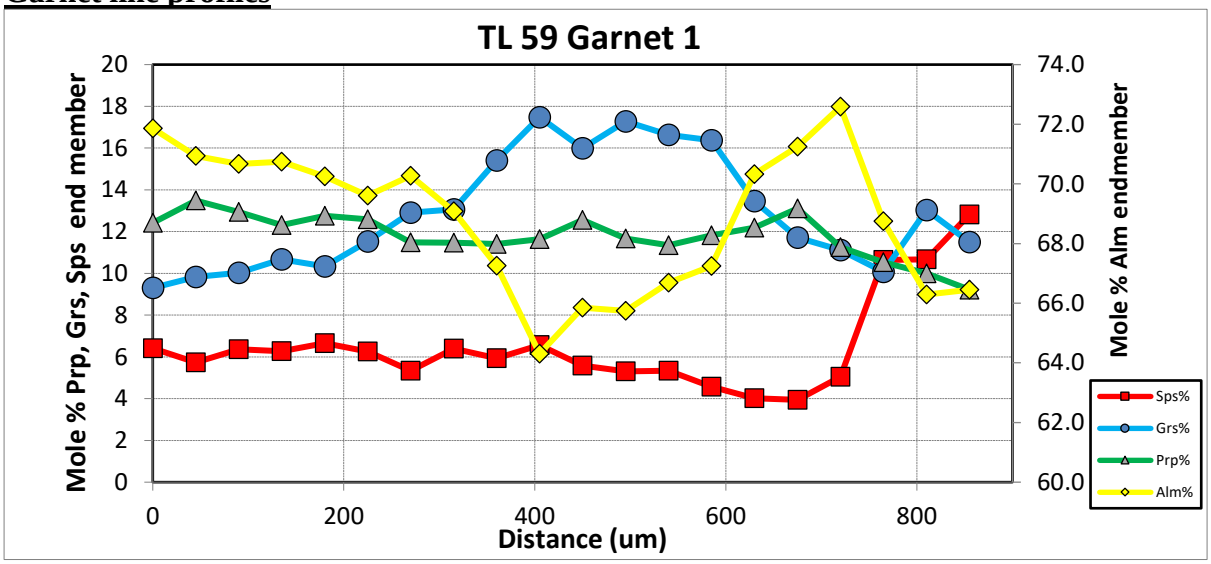

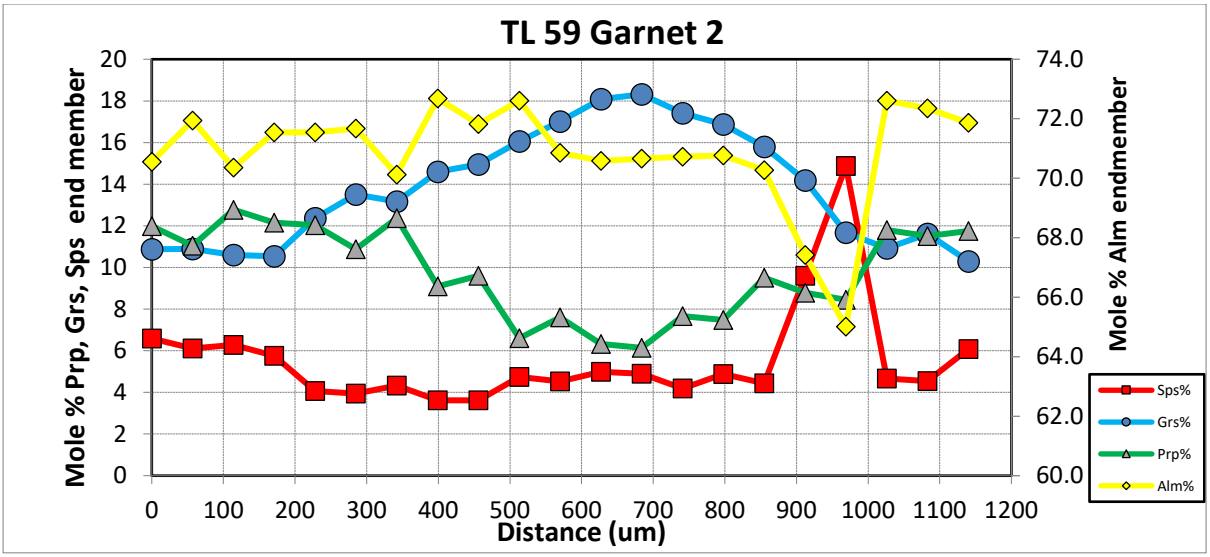

Garnets from sample TL59 preserve evidence for the prograde zoning patterns. Profile 2 represents a classic prograde zoning profile with a core high in grossular (18%) and low in pyrope (6%) with a systematic decrease in grossular and increase in pyrope towards the rim that has a composition of 10-11% grossular and 12% pyrope. Whereas Profile 1 shows rather uniform values of pyrope in the core and only a slight increase in pyrope followed by a decrease and almandine shows a systematic increase towards the rim. Spessartine in both garnets shows an irregular profile with an overall increase towards the rim but spikes in Mn within garnet interior is due to internal fractures resorbing some garnet.

3.5.4 TLN18

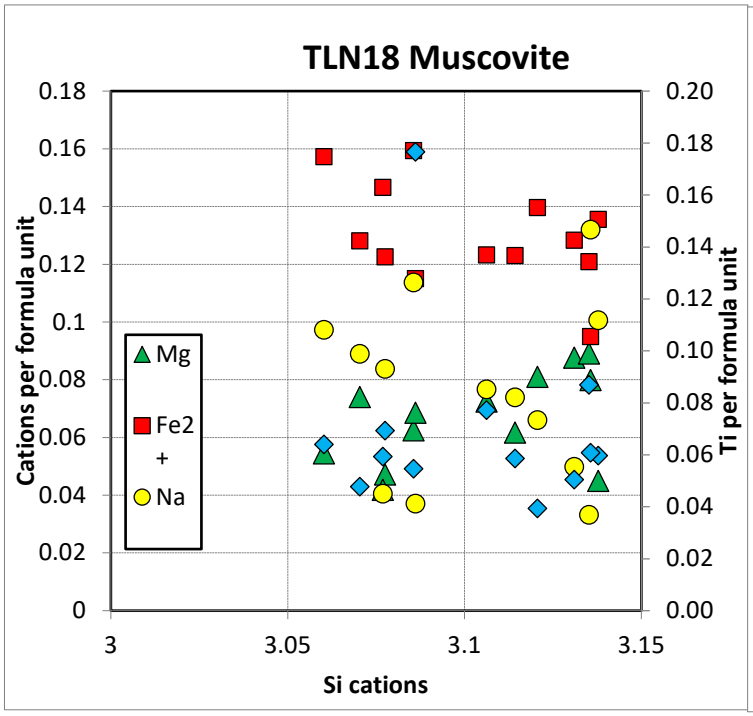

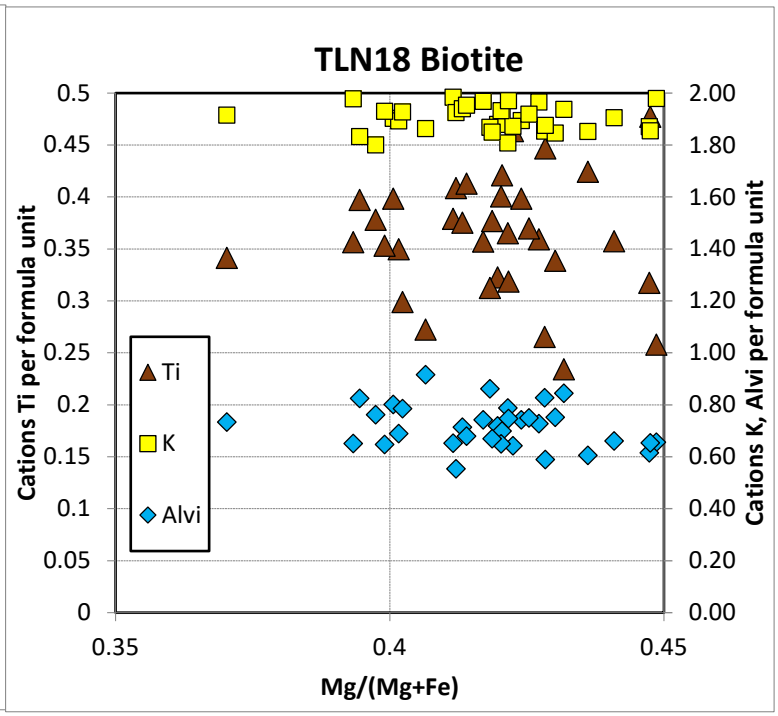

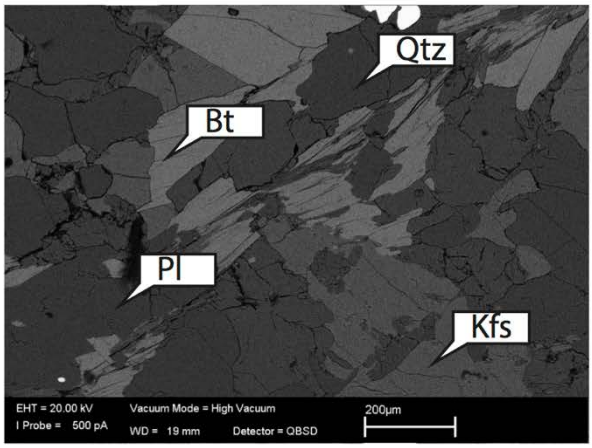

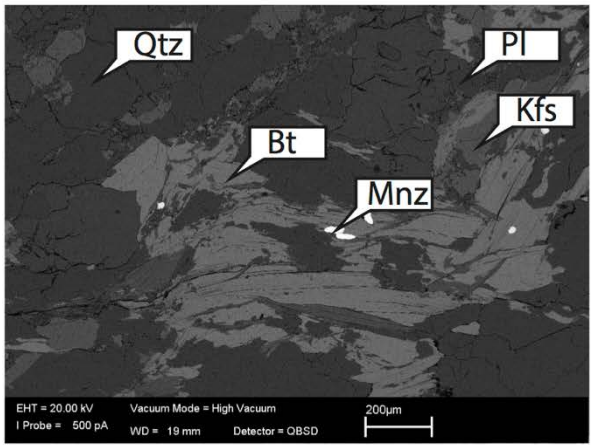

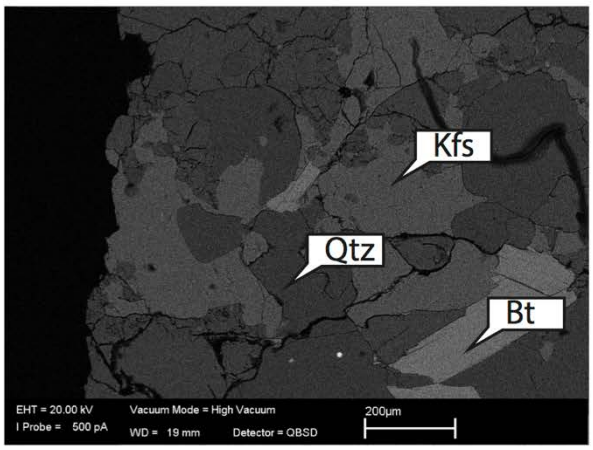

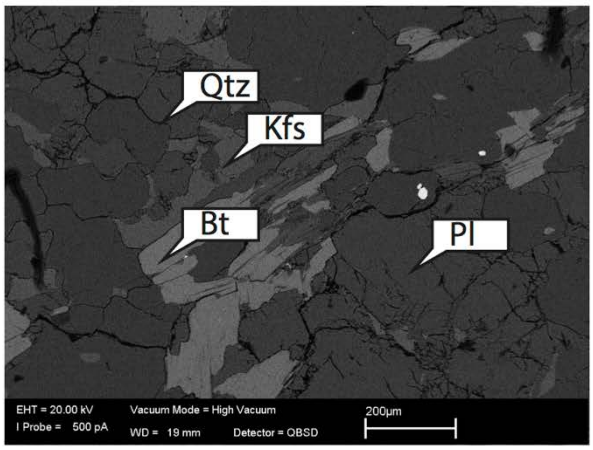

Figure 3.5.4.1 SEM images of TLN18 Diatextite with abundant k-feldspar, plagioclase and schiellern of biotite marking the foliation, larger monazite can be found commonly within plagioclase and biotite, lack of muscovite suggest the muscovite dehydration melting reaction was the dominant melting process.

3.5.5 TLN20A

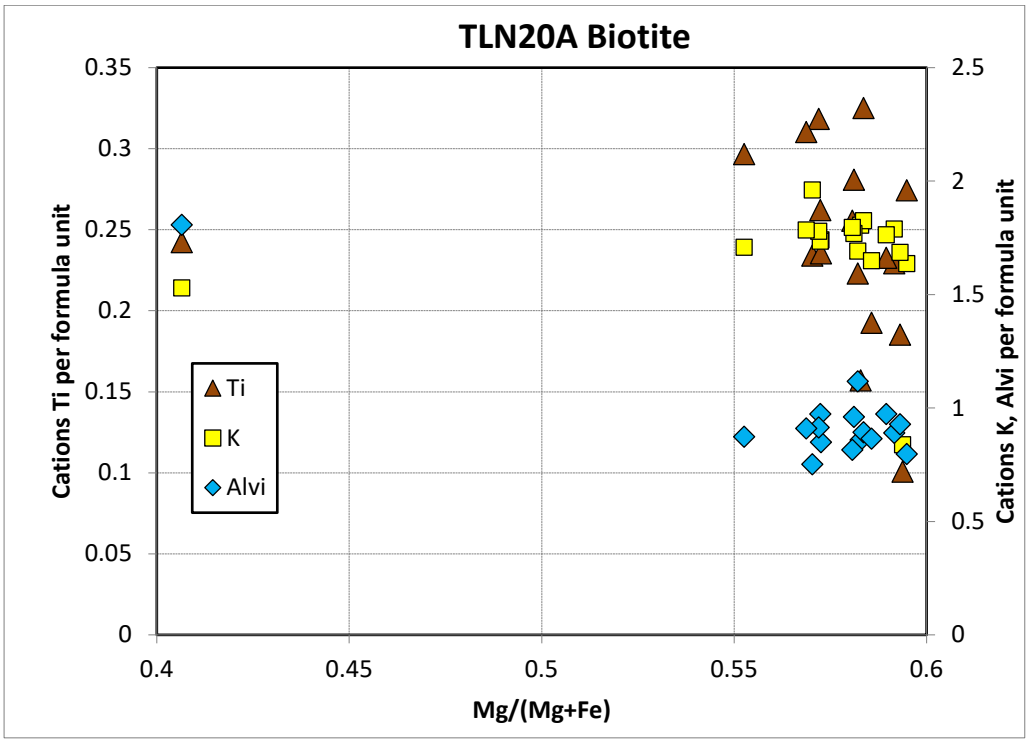
TLN20A Biotite
Cations Ti per formula unit
Cations K, Alvi per formula unit
Mg/(Mg+Fe)
Ti
K
Alvi
0.35
0.3
0.25
0.2
0.15
0.1
0.05
0
2.5
2
1.5
1
0.5
0
0.4
0.45
0.5
0.55
0.6

3.5.6 TLN34

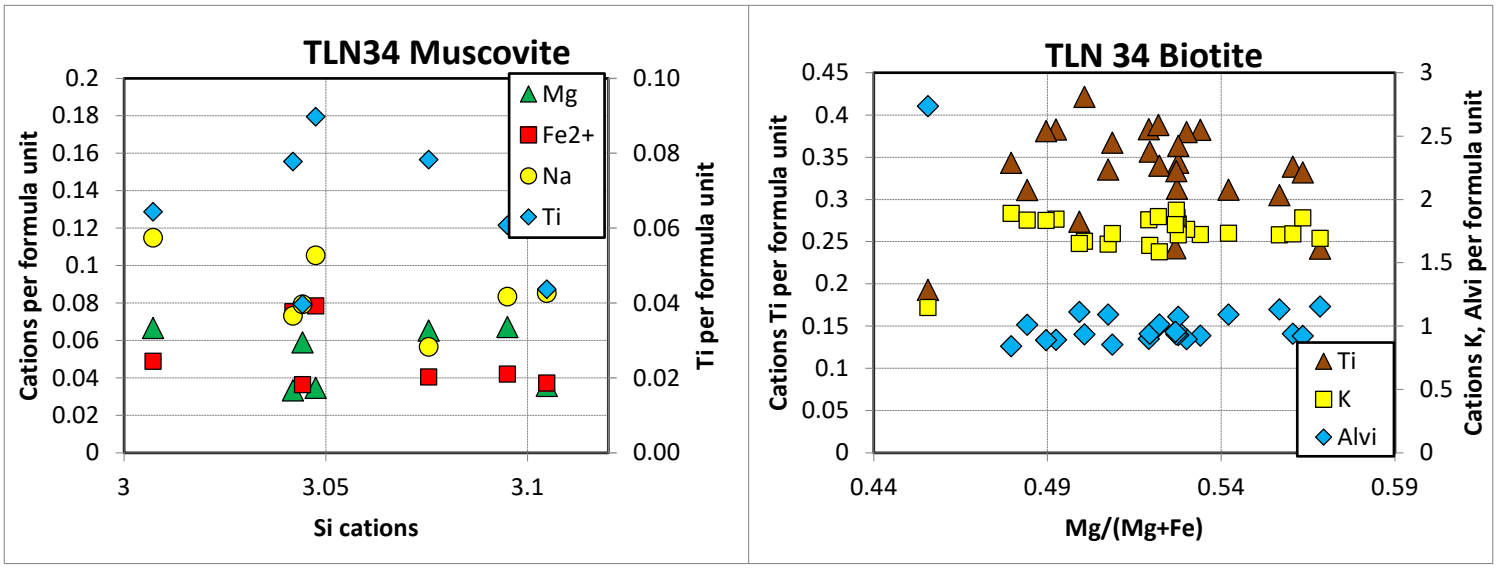

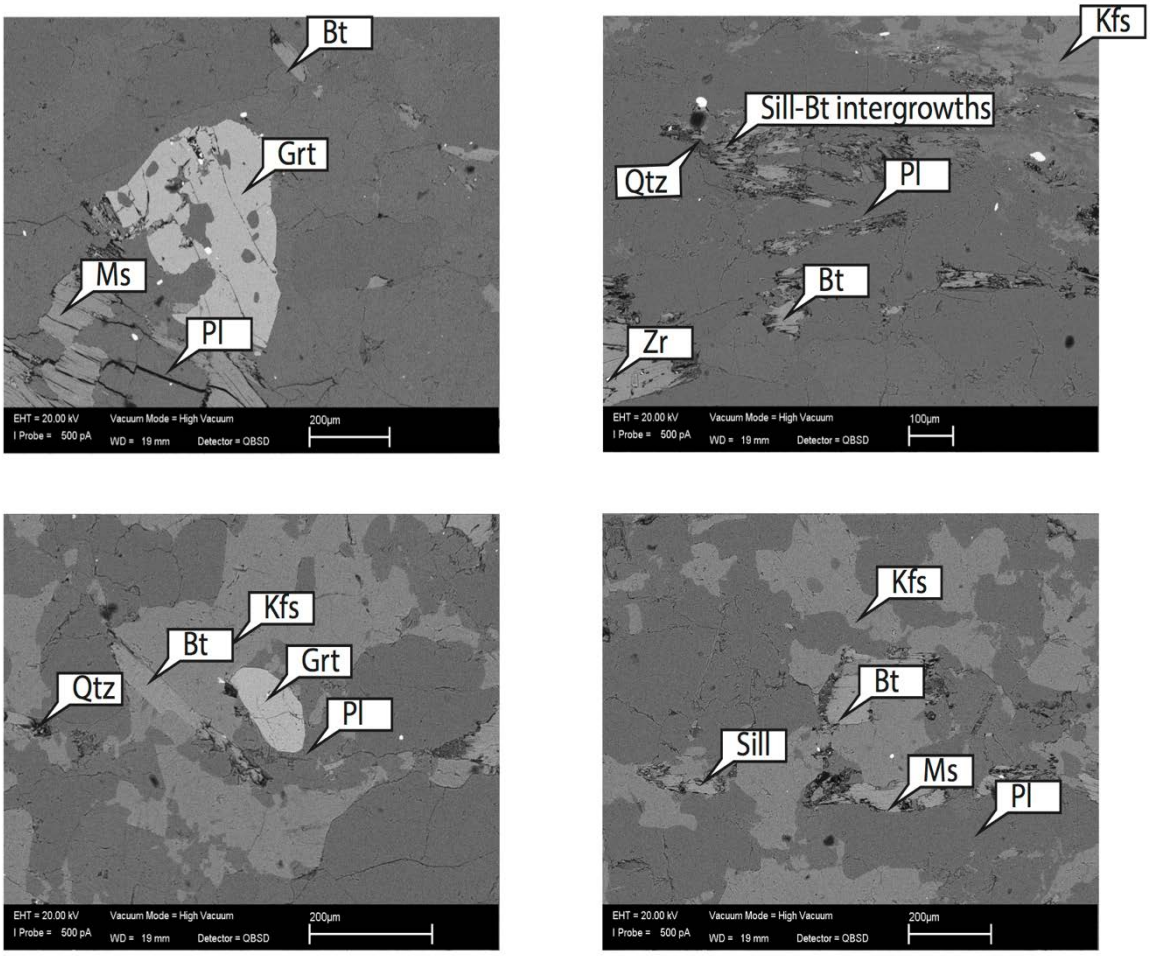

Figure 3.5.6.1 SEM images for TLN34 showing diagnostic textures of muscovite dehydration melting. There are sillimanite-biotite-quartz intergrowths and peritectic K-feldspar. Minor secondary muscovite off plagioclase garnet and sillimanite and maybe pseudomophing K-feldspar.

Garnet line Profiles

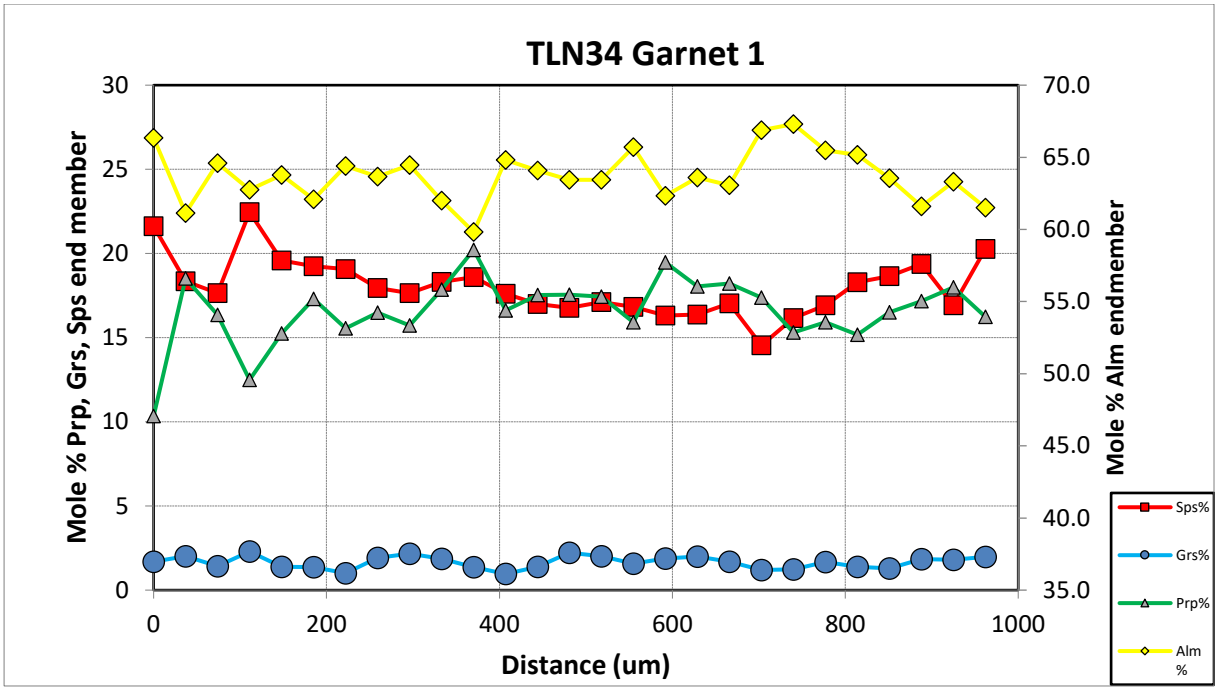

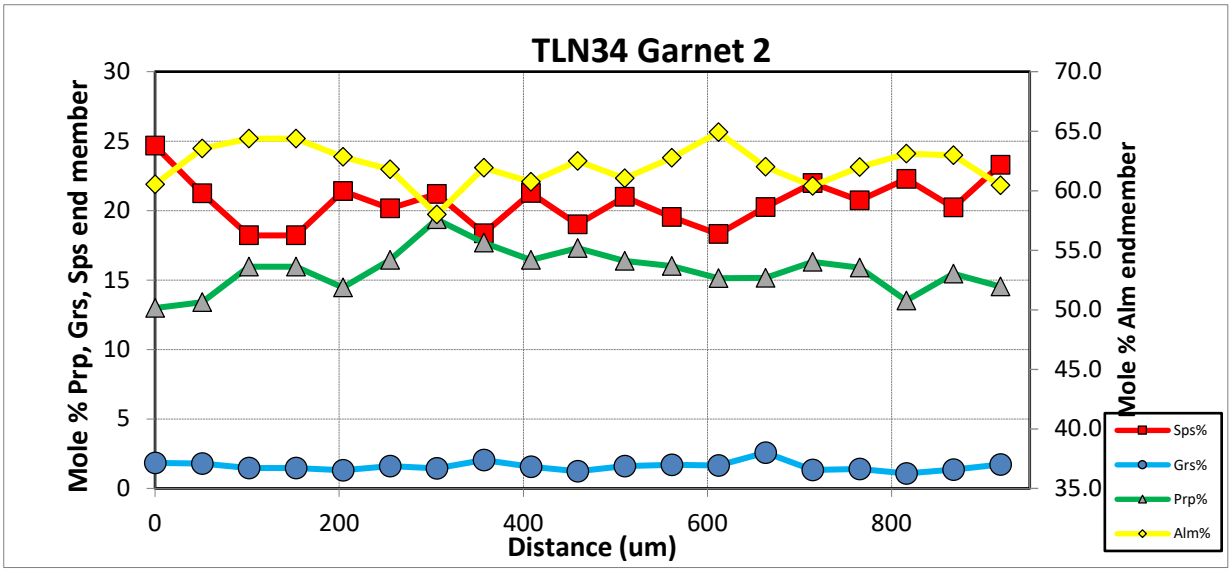

Garnets from this sillimanite migmatite from the core of the dome with muscovite dehydration melting features and peritectic Kfs, shows classic garnet homogenization profiles with a flat uniform amount of grossular and overall decrease in pyrope towards the rim. We interpret this as high temperature diffusion homogenization and growth of garnet in the presence of melt at low pressure with ~ 16-17% pyrope at 2% grossular. There is a classic kick in Mn towards the rim, characteristic of high-grade resorbtion.

3.5.7 TLN35

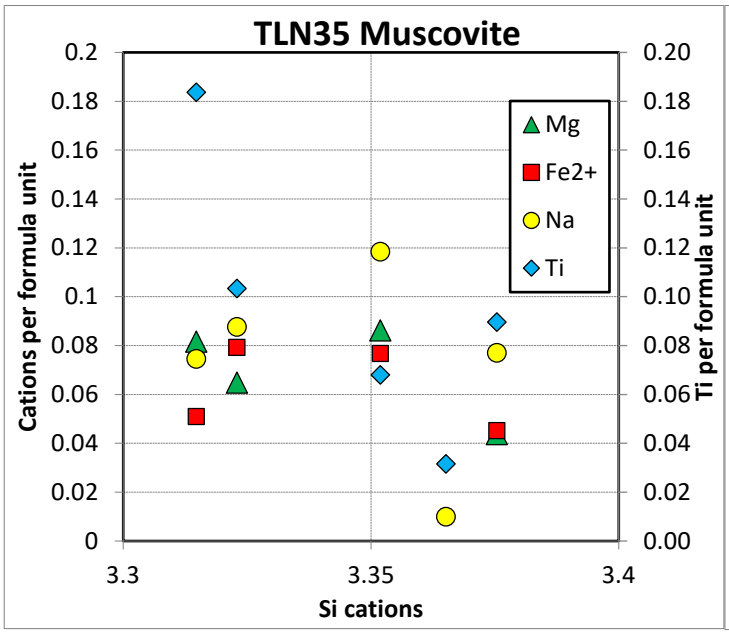

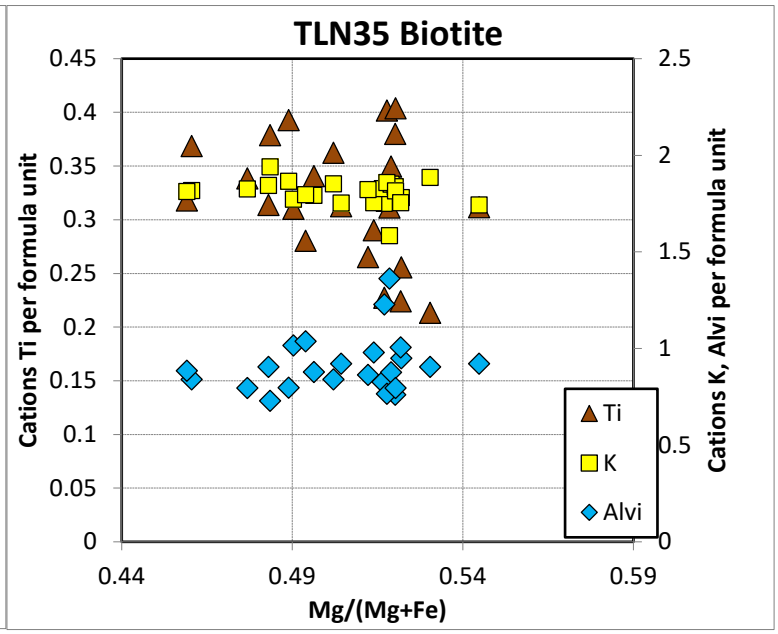

Garnet Line profiles

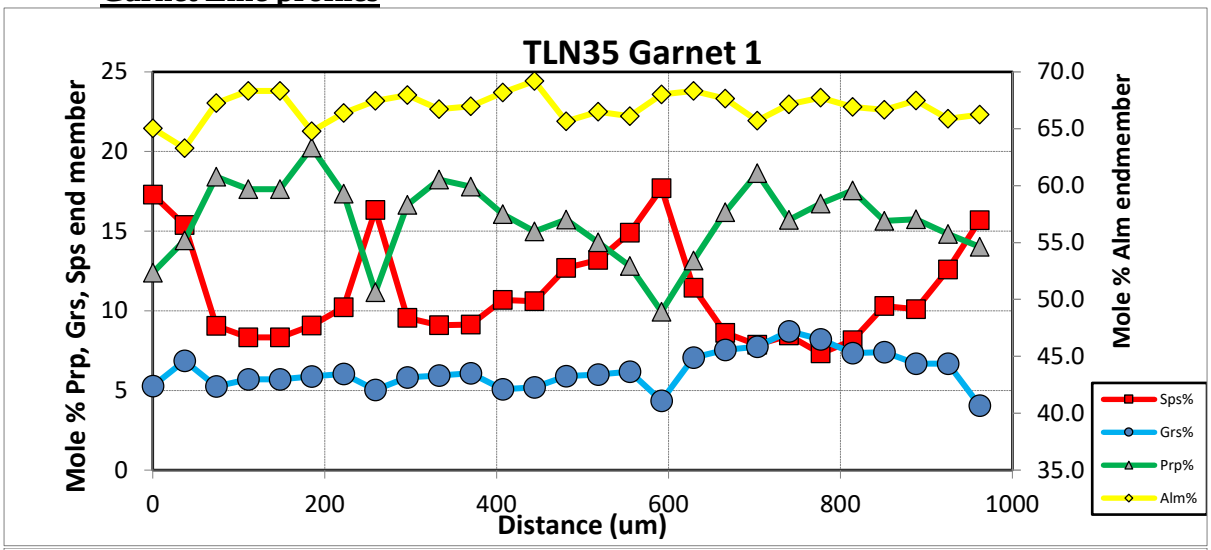

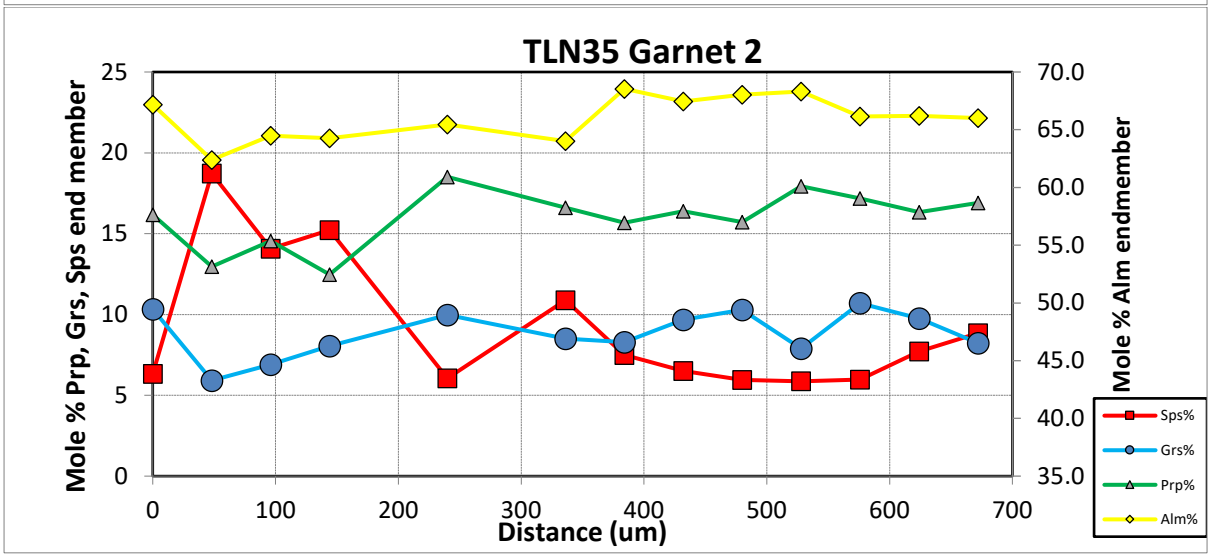

Garnet in TL35 are characterised by homogenized profiles with classic diffusion profiles with almost flat grossular and pyrope profiles that are interrupted by fractures within garnet causing small irregular spikes in Spessartine and decreases in Pyrope. The spikes in Spessartine content is due to resorbtion at high temperature following garnet formation causing the irregular and poor shape preserved in thin section. This is interpreted to have occurred at low pressure when garnet is less stable at ca. 5 kbars corresponding to the garnet out reaction.

4. Thermobarometry and Equilibrium Phase Modelling

A range of thermobarometric tools were used to harness the *P-T* conditions of the Naxos Core Complex. These included classical thermobarometers (GASP) and others that are compiled in Av-PT (Thermocalc v3.40i mode 2 average *P-T* calculations), independent Ti in bitiote thermometry and also a pseudosection approach using Thermocalc v3.40i and dataset 62 for samples TLN54, TL15, TL66, TL67.

4.1 Classical thermobarometry:

Grt-Als-Pl-Qtz and Grt-Bt Fe-Mg exchange thermometry ((Bhattacharya et al., 1992; Spear et al., 1993):

Grt-Ky/Sill–Plag–Qtz geobarometry (Spear, 1993) combined with Grt–Bt Fe/Mg exchange thermometry (Bhattacharya et al., 1992), was applied to all samples with the relevant phases in the Koronos and Core Units as a 1st pass estimate of the *P–T* conditions within the Naxos Core Complex. Representative analyses from garnet cores and garnet rims where used with representative mineral data to see the trend of the *P–T* path during garnet growth. The quoted uncertainities are ± 1.3 kbar and ± 50 °C. The results are presented below in table combined with Ti in Biotite thermometry and Thermocalc mode 2 Average-PT results for all studied samples.

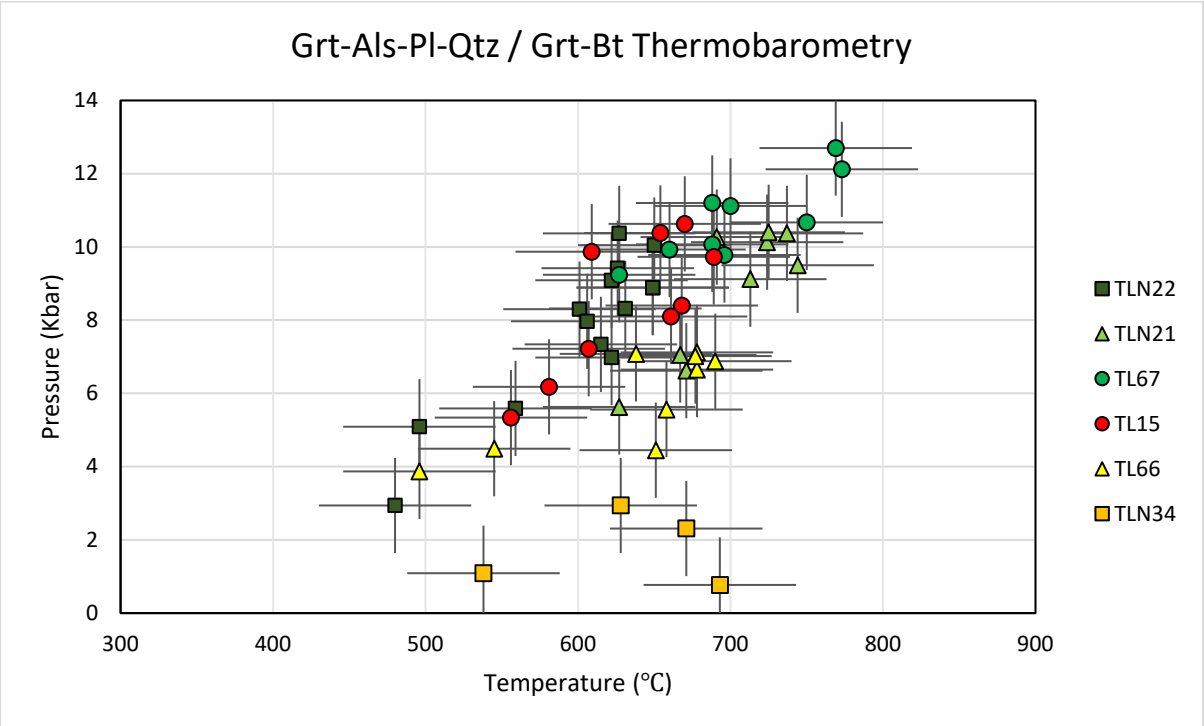

Figure 4.1.1: Grt-Als-Pl-Qtz / Grt-Bt thermobarometry results from samples, TL67, TLN21, TLN22 from the Koronos Unit and samples TL15, TL66 and TLN34 from the Core Unit migmatites, note the lower pressures and temperatures of the Core Unit due to equilibration at high-temperatures in the presence of melt.

Table 4.1.1 Grt-Bt / Grt-Ky-Pl-Qtz Thermobarometry Results

Unit	Sample	Notes	Temp (℃)	Pressure (Kbar)
Koronos	TLN22	Inner Rim	650.000	10.050
Koronos	TLN22	Core	627.000	10.370
Koronos	TLN22	Outer rim	496.000	5.090
Koronos	TLN22	Mid rim	601.000	8.300
Koronos	TLN22	Int	626.000	9.420
Koronos	TLN22	Core	649.000	8.890
Koronos	TLN22	Rim	615.000	7.340
Koronos	TLN22	Rim	480.000	2.940
Koronos	TLN22	Int	649.000	8.890
Koronos	TLN22	Core	606.000	7.970
Koronos	TLN22	Rim	622.000	6.980
Koronos	TLN22	Rim	631.000	8.320
Koronos	TLN22	Core Int	622.000	9.090
Koronos	TLN22	Rim	559.000	5.590
Koronos	TLN21	Inner Rim	744.000	9.500
Koronos	TLN21	Inner Rim	724.000	10.130
Koronos	TLN21	Inner Rim	725.000	10.400
Koronos	TLN21	Inner Rim	691.000	10.270
Koronos	TLN21	Inner Rim	737.000	10.370
Koronos	TLN21	Outer Rim	667.000	7.050
Koronos	TLN21	Inner Rim	713.000	9.120
Koronos	TLN21	Core	627.000	5.630
Koronos	TLN21	Outer Rim	671.000	6.620
Koronos	TL67	Inner Rim	773.000	12.120
Koronos	TL67	Core	700.000	11.120
Koronos	TL67	Int	688.000	10.070
Koronos	TL67	Core	660.000	9.930
Koronos	TL67	Outer Rim	750.000	10.670
Koronos	TL67	Inner Rim	696.000	9.780
Koronos	TL67	Grt Core	627.000	9.240
Koronos	TL67	Grt Core-Int	688.000	11.200
Koronos	TL67	Grt Rim	769.000	12.700
Core	TL15	Core	609.000	9.870
Core	TL15	Int	689.000	9.730
Core	TL15	Inner Rim	654.000	10.380
Core	TL15	Core	668.000	8.400
Core	TL15	Outer Rim	556.000	5.340
Core	TL15	Outer Rim	607.000	7.220
Core	TL15	Outer Rim	661.000	8.100
Core	TL15	Inner Rim	670.000	10.630
Core	TL15	Outer Rim	581.000	6.180
Core	TL66	Inner Rim	690.000	6.880
Core	TL66	Inner Rim	638.000	7.080
Core	TL66	Inner Rim	678.000	6.650
Core	TL66	Outer Rim	545.000	4.490
Core	TL66	Core	678.000	7.120
Core	TL66	Core	677.000	7.020
Core	TL66	Outer Rim	658.000	5.560
Core	TL66	Outer Rim	496.000	3.870
Core	TL66	Outer Rim	651.000	4.450
Core	TLN34	Core	671.000	2.310
Core	TLN34	Int	693.000	0.770
Core	TLN34	Core	628.000	2.940
Core	TLN34	Rim	538.000	1.090

Ti in Biotite thermometry (Henry et al., 2005):

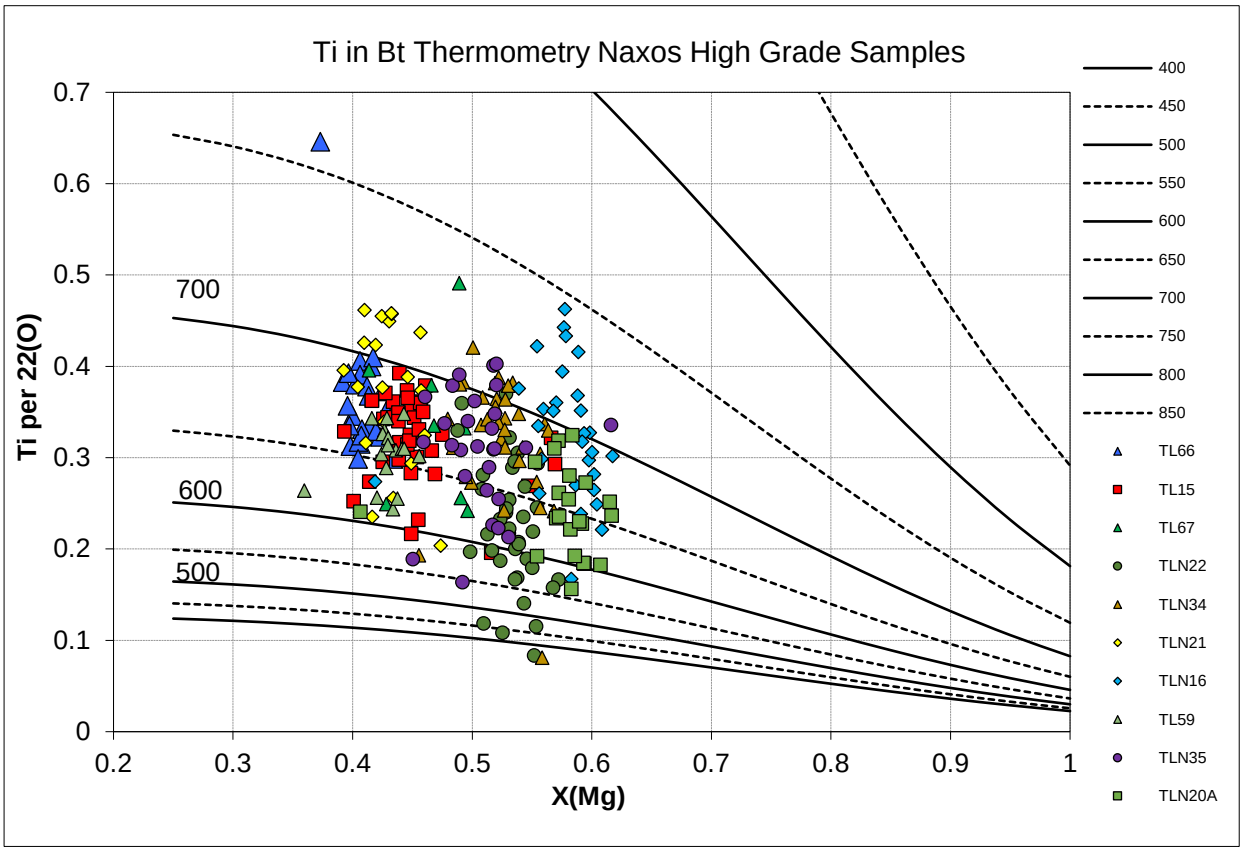

Figure 4.1.2: Results of Ti in Biotite thermometry using the thermometer of Henry et al., 2005 for Naxos high-grade samples from the Koronos and Core Units

Average *P-T* thermobarometry:

Thermocalc version 3.40i was used in mode 2 for average *P-T* calculations (avPT). This was applied to all studied samples. Activities of solid-solution end members were then calculated using AX (Holland, 2009) and these were used to determine independent sets of reactions based on mineral end members to calculate an average pressure and temperature based on the intersection of reaction lines. The results are presented below coloured for samples within each unit, see table 5 for full results.

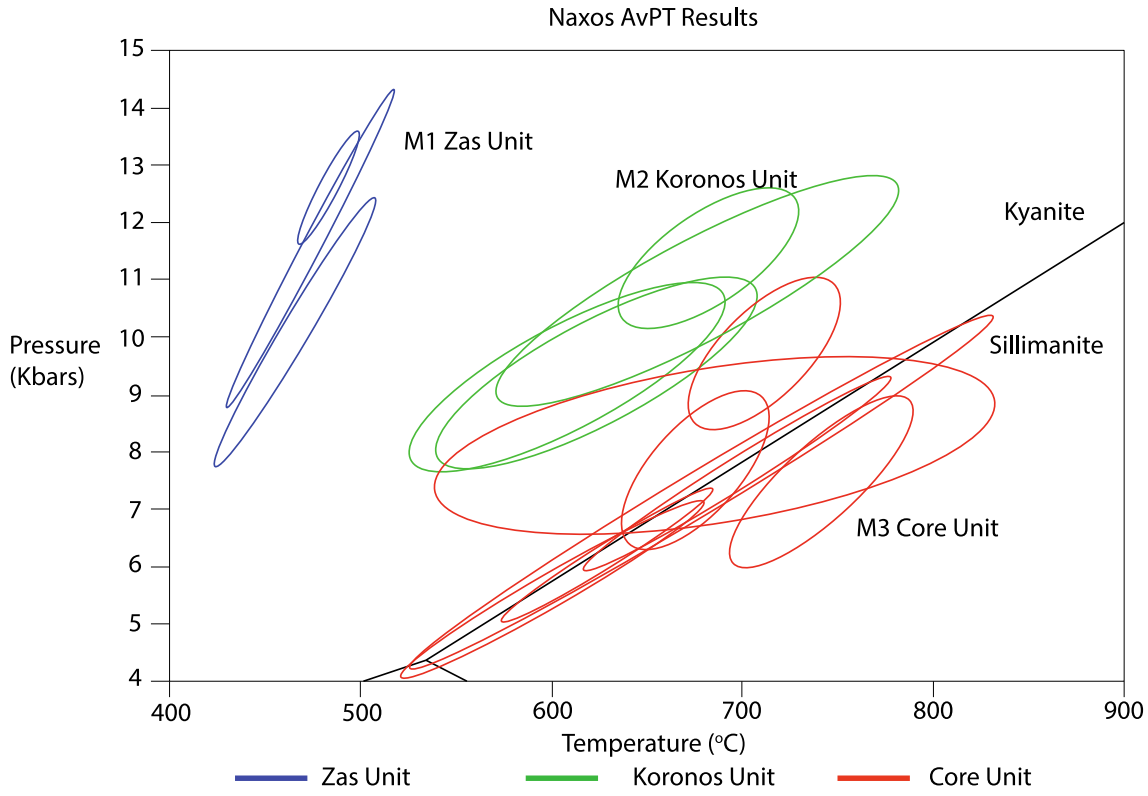

Figure 4.1.3 Average peak P-T results for Naxos samples with ellipses representing a 1 S.D. level uncertainty. There are 2 distinctly different P-T conditions, the Zas Unit recording HP-LT conditions and a regional MP-HT Barrovian P-T loop recoded by the Koronos and Core Units within Naxos. The Koronos Unit records higher-pressures because it was not thermally re-equilibrated at supra-solidus conditions. Note, the re-equilibration of biotite and secondary muscovite within the core unit record lower than peak temperatures and is a result of diffusion associated with high-temperature. i.e. the granulite uncertainty problem.

4.2 Equilibrium Phase Modelling:

Pseudosections were constructed using THERMOCALC version 3.40i and internally consistent data set 62 (Powell & Holland, 1988; Holland & Powell, 2011). Modeling of metasedimentary lithologies TL67, TL15, and TL66 was performed in the MnO–Na_2O–CaO–K_2O–FeO–MgO–Al_2O_3–SiO_2–H_2O–TiO_2–O (MnNCKFMASHTO) system using the following activity–composition relations: silicate melt (White et al., 2007), cordierite (Mahar et al., 1997; Holland & Powell, 1998), garnet and ilmenite (White et al., 2005), orthopyroxene (White et al., 2002), chlorite (Mahar et al., 1997; Holland et al., 1998), biotite (Ti-bearing model; (White et al., 2007)), muscovite (Coggon & Holland, 2002), K-feldspar and plagioclase (Holland & Powell, 2003) and magnetite (suprasolidus model; (White et al., 2002)). Modeling of metabasic lithologies TLN54 was performed in the MnO-absent NCKFMASHTO system, with the additional usage of the omphacitic clinopyroxene and amphibole activity–composition relations of Green et al. (2016). The pure phases andalusite, kyanite, sillimanite, rutile, quartz, and H_2O were considered in all cases. The bulk-rock supra-solidus water content of migmatitic units was fixed on an individual basis in order to allow minimal fluid saturation at the wet solidus; here defined as ~1 mol% free H_2O.

4.2.1 Harnessing bulk compositions

The effective bulk composition used for modeling was initially calculated following the method of Carson et al., (1999). Bulk rock compositions were calculated by point counting various phases within a representative area of the thin section that is envisaged to be in equilibrium at a certain set of *P-T* conditions. Areas were targeted within the thin section that were believed to represent peak metamorphic conditions in the rock and a well equilibrated area. Full slide scans combined with representative SEM images were used to discriminate between optically similar minerals quartz, plagioclase and K-feldspar using J-microvision imaging software. These proportions were then combined with their representative average compositions using mineral geometrical data for un-zoned minerals. Garnet was the only phase to have internal compositional zoning; therefore, a compositional contribution was produced by the integration of concentric shells, assuming spherical geometry in order to obtain an average chemical composition. Where relevant, the Fe content of individual minerals was calculated using the software AX (Holland, 2009). Because THERMOCALC utilizes molar proportions of oxides, an in house spreadsheet recalculates averaged data from individual minerals into overall molar proportions, suitable for THERMOCALC.

Table 4.2.1 below summarizes the bulk compositions of each sample investigated.

Table 4.2.1 Bulk Rock Calculation

Mineral	Si	Ti	Al	Fe3+	Fe2+	Mn	Mg	Ca	Na	K	H	cat sum (-H)	Mol vol	for (O)	Vol% in:
TLN54															
Na-amp	7.96	0.01	1.80	0.15	1.70	0.01	1.41	0.04	1.94	0.01	15.02	15.02	263.60	23	17.0
Bt	3.30	0.01	1.30	0.11	0.88	0.00	1.09	0.00	0.00	1.00	2.00	7.68	149.63	22	2.0
Chl	2.77	0.00	2.46	0.00	2.70	0.00	2.07	0.00	0.00	0.00	8.00	10.00	208.81	14	11.0
Ms	3.41	0.00	2.15	0.00	0.19	0.00	0.26	0.00	0.05	0.95	2.00	7.00	140.48	22	31.0
Pg	3.28	0.00	2.55	0.00	0.12	0.00	0.05	0.00	0.95	0.05	2.00	7.00	133.52	22	4.5
Ep	3.00	0.00	3.00	0.00	0.00	0.00	0.00	2.00	0.00	0.00	1.00	8.00	136.00	12.5	3.0
Pl	3.00	0.00	1.00	0.00	0.00	0.00	0.00	0.00	1.00	0.01	0.00	5.00	100.15	8	22.0
Ilm/Hem	0.00	1.04	0.00	0.00	0.91	0.00	0.00	0.00	0.00	0.00	0.00	1.95	31.75	3	0.5
Rt	0.00	1.00	0.00	0.00	0.00	0.00	0.00	0.00	0.00	0.00	0.00	1.00	18.82	2	3.0
Qtz	1.00	0.00	0.00	0.00	0.00	0.00	0.00	0.00	0.00	0.00	0.00	1.00	22.69	2	6.0
TL67															
Grt	3.00	0.00	1.91	0.09	2.05	0.16	0.34	0.42	0.00	0.00	0.00	7.97	116.2	12	10.2
Chl	2.52	0.00	2.96	0.00	2.36	0.00	2.16	0.00	0.00	0.00	8.00	10.00	208.0	14	0.6
Bt	2.70	0.18	1.68	0.12	1.01	0.02	1.07	0.00	0.00	1.00	2.00	7.78	150.3	11	17.5
Ms	3.05	0.00	2.84	0.00	0.08	0.00	0.05	0.00	0.04	0.96	2.00	7.00	140.8	11	12.0
Kfs	2.98	1.00	1.02	0.00	0.00	0.00	0.00	0.02	0.11	0.87	0.00	6	107.9	8	7.5
Pl	2.70	0.00	1.30	0.00	0.00	0.00	0.00	0.30	0.67	0.03	0.00	5.00	100.6	8	20.3
Ilm	0.00	0.41	0.00	1.19	0.39	0.01	0.00	0.00	0.00	0.00	0.00	2	30.9	3	0.3
Rt	0.00	1.00	0.00	0.00	0.00	0.00	0.00	0.00	0.00	0.00	0.00	1	18.8	2	0.1
Ky	1.00	0.00	2.00	0.00	0.00	0.00	0.00	0.00	0.00	0.00	0.00	3	49.9	5	5.3
Qtz	1.00	0.00	0.00	0.00	0.00	0.00	0.00	0.00	0.00	0.00	0.00	1	22.7	2	26.2
TL66															
Grt	3.00	0.00	2.00	0.00	0.00	0.30	0.35	0.18	0.00	0.00	0.00	5.83	115.9	12	1.6
Chl	1.95	0.00	4.10	0.00	0.00	0.00	3.95	0.00	0.00	0.00	8.00	10.00	205.1	14	0.6
Bt	2.71	0.16	1.76	0.14	1.16	0.03	0.84	0.00	0.00	1.00	2.00	7.80	150.5	11	18.2
Ms	3.06	0.00	2.73	0.00	0.00	0.00	0.20	0.00	0.07	0.93	2.00	7.00	140.6	11	24.1
Pl	2.65	0.00	1.35	0.00	0.00	0.00	0.00	0.35	0.63	0.01	0.00	5.00	100.5	8	21.2

Ilm	0.00	0.41	0.00	1.19	0.39	0.01	0.00	0.00	0.00	0.00	0.00	2	30.9	3	0.6
Rt	0.00	1.00	0.00	0.00	0.00	0.00	0.00	0.00	0.00	0.00	0.00	1	18.8	2	0.1
Sil	1.00	0.00	2.00	0.00	0.00	0.00	0.00	0.00	0.00	0.00	0.00	3	49.9	5	7.6
Qtz	1.00	0.00	0.00	0.00	0.00	0.00	0.00	0.00	0.00	0.00	0.00	1	22.7	2	26.0
TL59															
Grt	3.00	0.00	1.93	0.07	2.09	0.19	0.23	0.45	0.00	0.00	0.00	7.97	116.4	12	3.3
Bt	2.82	0.16	1.62	0.14	1.13	0.02	0.89	0.00	0.00	1.00	2.00	7.77	150.5	11	12.3
Ms	3.14	0.00	2.54	0.00	0.24	0.00	0.09	0.00	0.01	0.99	2.00	7.00	140.7	11	26.6
Pl	2.70	0.00	1.30	0.00	0.00	0.00	0.00	0.30	0.69	0.01	0.00	5.00	100.4	8	24.5
Ilm	0.00	0.41	0.00	1.19	0.39	0.01	0.00	0.00	0.00	0.00	0.00	2	30.9	3	0.9
Ky	1.00	0.00	2.00	0.00	0.00	0.00	0.00	0.00	0.00	0.00	0.00	3	49.9	5	1.0
Qtz	1.00	0.00	0.00	0.00	0.00	0.00	0.00	0.00	0.00	0.00	0.00	1	22.7	2	31.4
TL15															
Grt	3.00	0.00	1.98	0.02	2.16	0.11	0.41	0.33	0.00	0.00	0.00	8.01	115.9	12	4.5
Bt	2.72	0.16	1.69	0.13	1.06	0.01	1.03	0.00	0.00	1.00	2.00	7.80	150.3	11	18.5
Ms	3.10	0.00	2.68	0.00	0.10	0.00	0.11	0.00	0.10	0.90	2.00	7.00	140.7	11	16.0
Pl	2.73	0.00	1.27	0.00	0.00	0.00	0.00	0.27	0.72	0.01	0.00	5.00	100.4	8	31.0
Ilm	0.00	0.41	0.00	1.19	0.39	0.01	0.00	0.00	0.00	0.00	0.00	2	30.9	3	0.5
Ky	1.00	0.00	2.00	0.00	0.00	0.00	0.00	0.00	0.00	0.00	0.00	3	0.0	5	4.5
Qtz	1.00	0.00	0.00	0.00	0.00	0.00	0.00	0.00	0.00	0.00	0.00	1	22.7	2	25.0

Calculated bulk rock composition in moles for key samples

Table S4	**Calculated Bulk Rock Molar Proprtions**										
	SiO2	**TiO2**	**Al2O3**	**FeO**	**MnO**	**MgO**	**CaO**	**Na2O**	**K2O**	**O**	**H2O**
TLN54											
From mineral data	48.903	3.383	10.599	6.410	-	5.214	0.884	3.689	2.177	0.107	18.633
Anhydrous	60.101	4.158	13.027	7.878	-	6.409	1.087	4.534	2.675	0.132	0.00
TL67											
From mineral data	62.359	2.177	12.639	7.589	0.345	3.586	2.135	1.605	2.887	0.369	4.652
Anhydrous	65.166	2.275	13.208	7.931	0.361	3.747	2.231	1.677	3.017	0.386	0.00
6.5% H2O	60.930	2.127	12.349	7.415	0.337	3.504	2.086	1.568	2.821	0.361	6.500
TL66											
From mineral data	62.625	0.751	14.894	4.273	0.174	3.468	1.750	1.655	3.216	0.459	6.908
Anhydrous	67.146	0.805	15.969	4.582	0.187	3.718	1.877	1.775	3.448	0.492	0.00
7.6% H2O	62.043	0.744	14.756	4.234	0.173	3.436	1.734	1.640	3.186	0.454	7.600
TL59											
From mineral data	66.589	0.571	11.469	5.727	0.162	2.166	1.920	1.912	3.041	0.537	6.069
Anhydrous	70.769	0.607	12.188	6.087	0.172	2.302	2.041	2.032	3.231	0.570	0.00
6.5% H2O	66.169	0.567	11.396	5.691	0.161	2.153	1.908	1.900	3.021	0.533	6.500
TL15											
From mineral data	64.301	0.619	11.498	6.296	0.130	3.645	2.285	2.720	2.671	0.424	5.541
Anhydrous	67.980	0.655	12.156	6.656	0.138	3.853	2.416	2.876	2.824	0.448	0.00
6.5% H2O	63.561	0.612	11.366	6.224	0.129	3.603	2.259	2.689	2.640	0.419	6.500

4.2.2 Additional *P-T* Pseudosections

TLN22

TLN22 is a kyanite grade schist with small but many garnets that appear to cross-cut the fabrics. These garnets also have mixed H_2O/ CO_2 fluid inclusions particularly in their cores. Due to this reason, and the textures indicative that the rock did not melt indicate the fluid composition during prograde metamorphism was mixed, and therefore a reduced water activity of 0.5 was chosen to harness pseudosection *P-T* information. The bulk composition was calculated using the above techniques. Garnet core compositions of 10% pyrope and 14 % grossular intersect at ca. 9 kbars 590 °C, with a systematic increase in pyrope and decrese in grossular to inner rim compositions of ~ 16.5% Pyrope and 10.5% grossular of which intersect at ca. 10.9 kbars, 700 °C in the Grt-Bt-Ms-Kfs-Rt-Pl-Qtz-H2O field, decompression through the muscovite dehydration reaction to produce kyanite, results in kyanite porphyroblasts aligned with the S3 foliation, and a rapid increase in the garnet modal proportions. Back reaction through the Ms in, K-feldspar out reaction results in muscovite growing with plagioclase around the domains with kyanite. Garnet outer rim compositions of 14.5% pyrope and 5% grossular intersect at ca. 7 kbar, 660 °C in the Grt-Bt-Ms-Ky-Rt-Ilm-Pl-Qtz-H2O field. This corresponds to the garnet rims appearing to grow synchronous with kyanite and is demonstrated as some kyanite overgrows the garnets whereas elswhere some garnet overgrows kyanite.

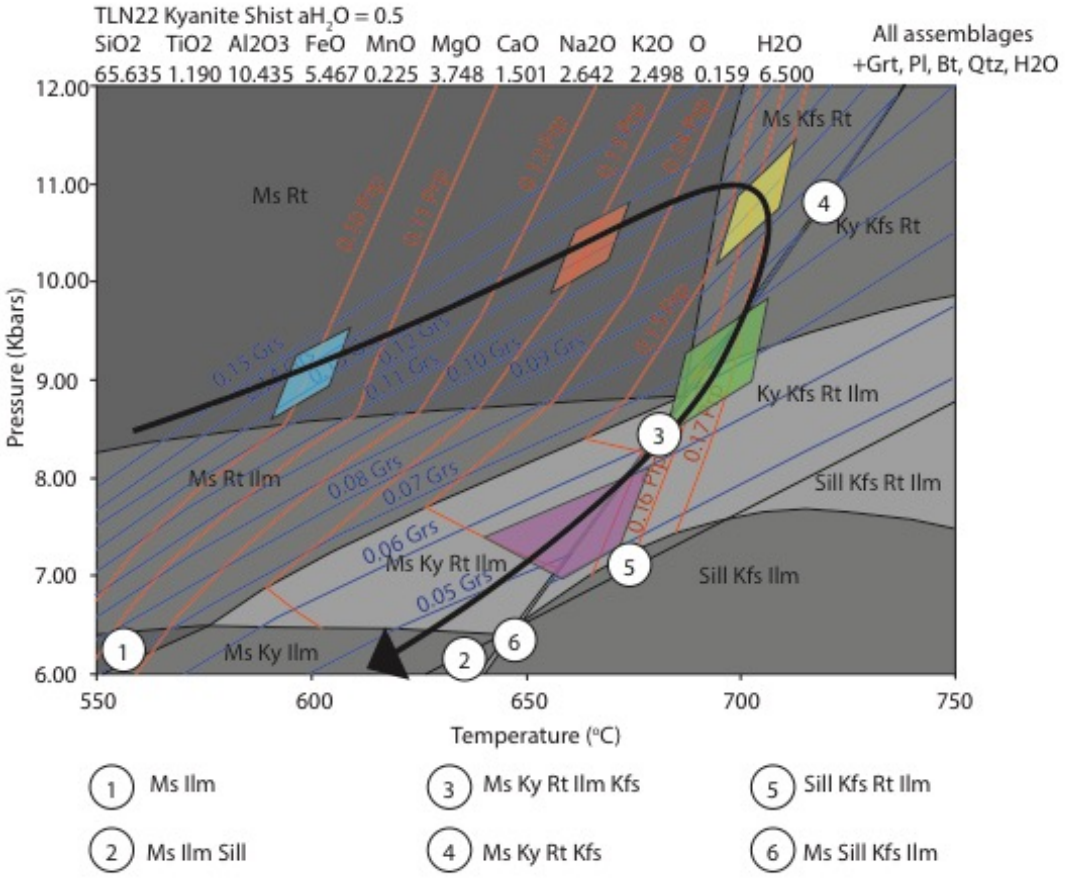

Figure 4.2.1: Calculated pseudosection for sample TLN22, using a reduced water activity to account for CO_2 inclusions within garnet and lack of melt textures. Peak P-T conditions predicted of 11 kbar, 700°C, similar to predicted P-T conditions from Grt-Ky-Pl-Qtz and Grt-Bt thermobarometry.

TL59

TL59 is a garnet biotite migmatite with no aluminium silicates, and was chosen for modelling as it represents the *P-T* conditions of rocks within 100m of the first appearance of melt. Its bulk composition was determined using the same methods as described above with excess H_2O used sub-solidus and 6.5% H_2O used for suprasolidus conditions. Garnet core compositions of ca. 17% grossular and 5% pyrope plot exactly on the garnet in reaction line at ca. 6.5 Kbars, 590 °C and then garnet compositions show a systematic decrease in grossular and increase in pyrope to inner rim compositions of ca. 10-11% pyrope and 12% grossular. This corresponds to an increase in both pressure and temperature during garnet growth, to peak conditions of ca. 9.5 kbars, 710 °C, beyond the water saturated melting reaction at kyanite grade conditions within the field, Grt-Bt-Ms-Pl-Kfs-Ilm-Qtz-Liq consistent with observed phase relations. This *P–T* condition is less than 10 °C beyond the Kfs in reaction line, and the lack of Kfs in this sample suggests the rock may not have overstepped the reaction, possibly because it didn't spend long enough at those conditions. The rock must have then decompressed with a slight decrease in temperature and not crossed the muscovite out reaction as no sillimanite or Kfs is preserved in the assemblage. Abundant secondary muscovite is found cross-cutting the fabrics and as garnet breakdown products suggesting the rock was re-hydrated at ca. 5-6 kbars as the it crossed the garnet out reaction along the hydrous solidus.

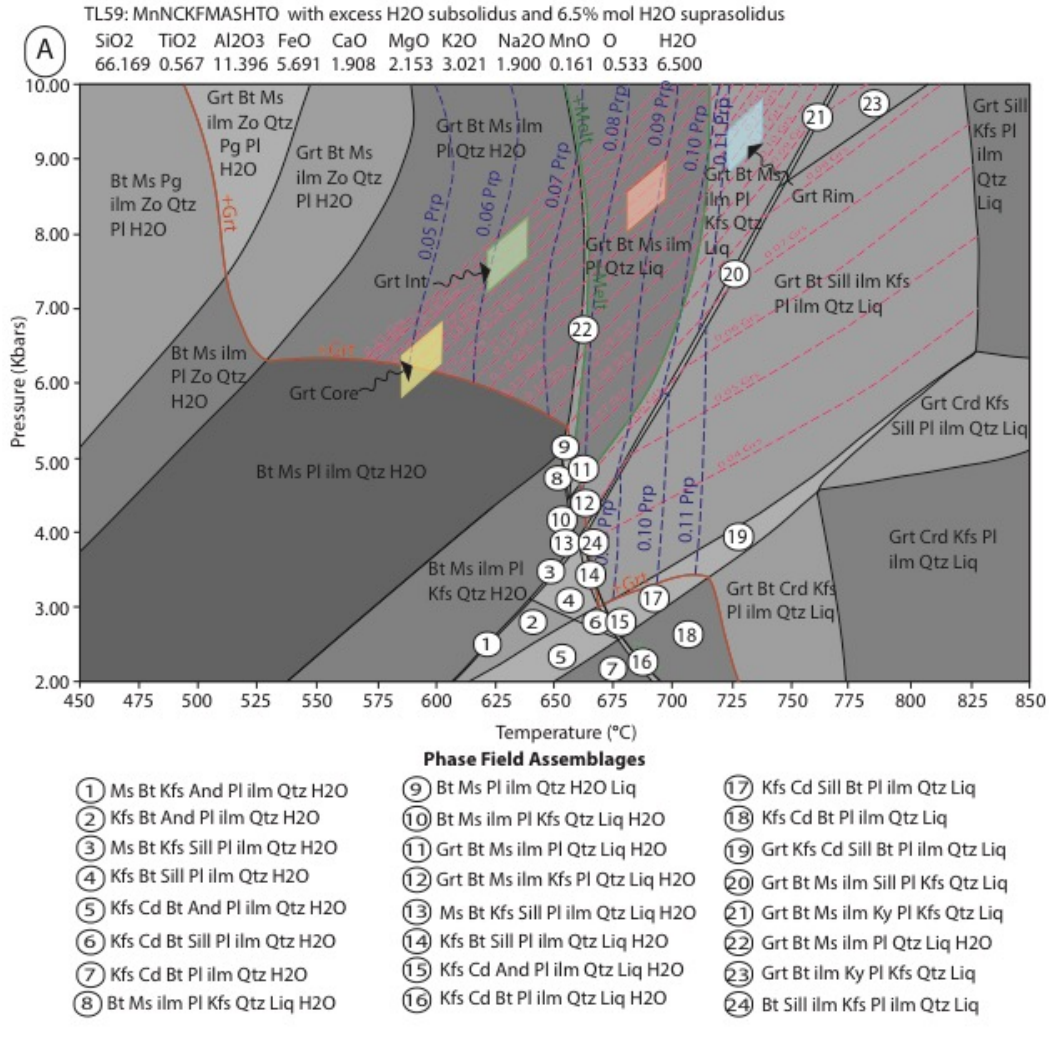

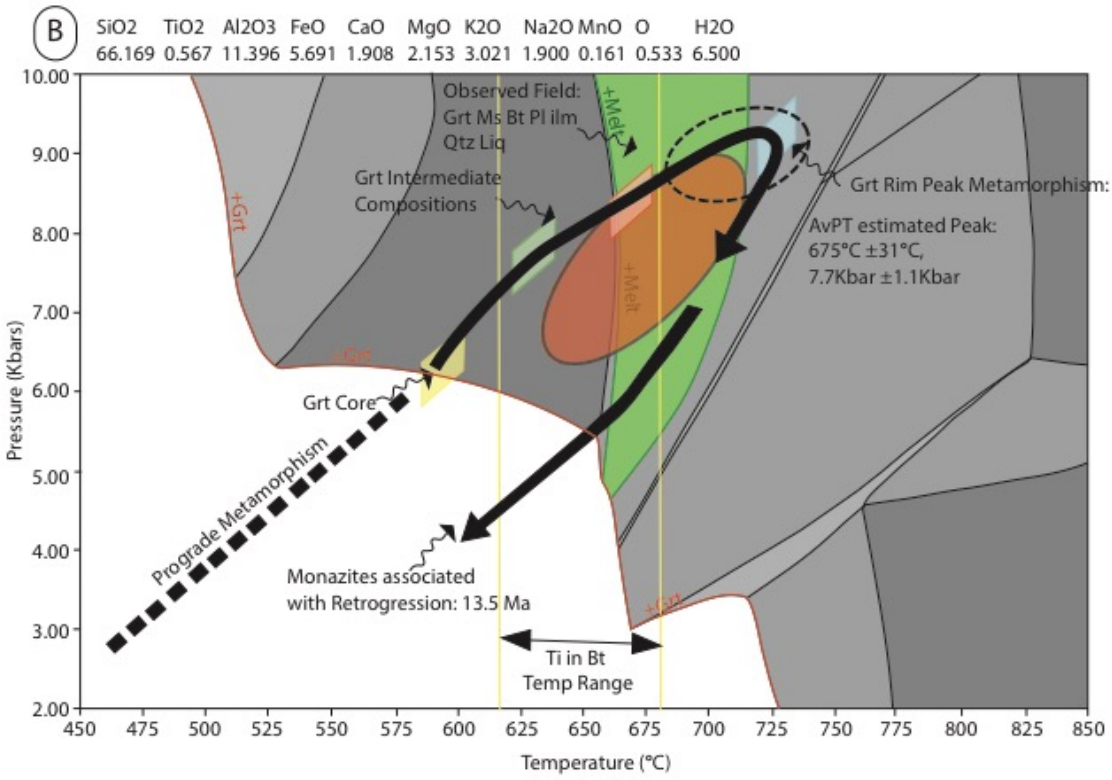

Figure 4.2.2 Equilibrium phase diagrams for sample TL59 revealing a clockwise P-T path with garnet core nucleation at the garnet in reaction at 6 kbar and 600 °C and peak P-T conditions of 9.5 kbar, 710°C with 12% Prp and 12% Grs, with overlaid average P-T results and Ti in Bt thermometry of Henery et al., (2005), which records lower temperatures due to requilibration.

TL66 Excess H_2O

Classical thermobarometry for TL66 predicts a clustered temperature of 660°C, however it is unlikely this represents peak metamorphism due to increased diffusivity with high temperatures making peak conditions unlikely to be preserved (Kohn and Spear., 2000) and extensive evidence for anatexis. Av-PT calculated an estimated peak of 6.5 kbar 730 °C (± 1.1 kbar, ± 22°C), indicating lower pressures than TL67. However, the presence of kyanite inclusions indicates of a higher pressure origin. Phase equilibria with excess H_2O was calculated for sub and supra solidus conditions, representing an external flux of water to produce maximum melting. A closed system model, more realistic of melting, was calculated using the best fitting molar % H_2O (7.6%) to ensure all water enters melt at the solidus, leaving water undersaturated conditions suprasolidus. An externally fluxing H_2O model was calculated to represent an endmember case when there is continuous supply of water to drive melting. For an externally fluxing water source, the model predicts large degrees of melts and no K-feldspar, consistent with the lack of K-feldspar in this sample. Garnet rim compositions (15% pyrope, 6% grossular) plot at 4.9 kbar, 705 °C with 33% melt. However, this extent of melting seems way too large, and kyanite preservation suggests little fluid infiltration that would have destroyed all earlier petrographic information. The predictions from this model are therefore unlikely to represent the reaction processes the rock experienced.

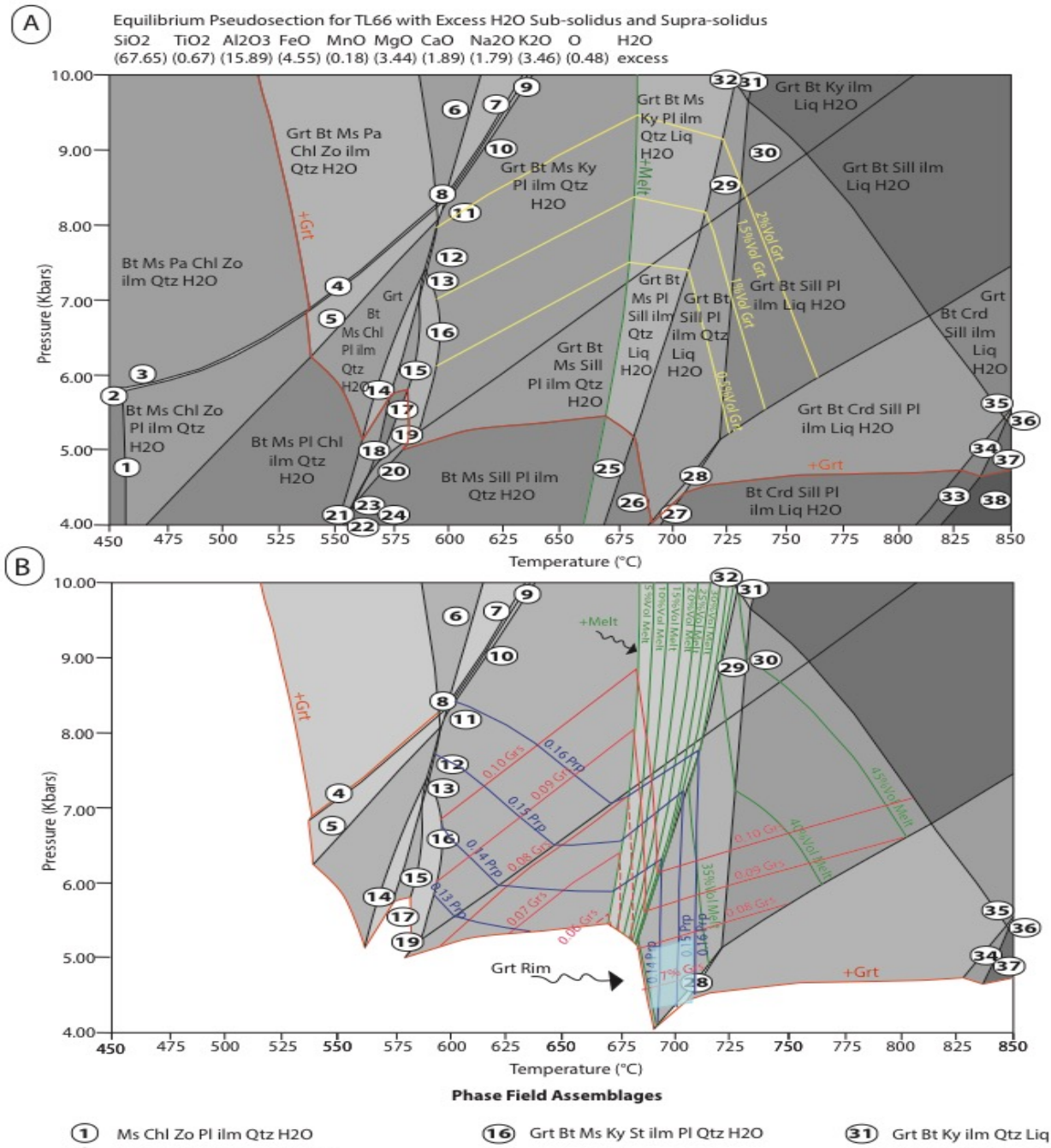

Figure 4.2.3: TL66 Sillimanite migmatite model for externally fluxing H_2O representing an open system of fluid, note the very large melt proportions which is inconsistent with petrographic observations

Melt re-integration (prograde evolution)

Melt re-integrated pseudosections were calculated to account for melt loss in migmatites as melt extraction leads to the formation of leucogranites. This occurs because once melt accumulation reaches a critical threshold in a rock, a portion may be lost, creating an open-system environment. This melt composition is dependent on the *P–T* conditions of formation (White & Powell, 2002), and melt extraction events may occur in an interrupted or continuous process (Sawyer, 1996). This open-system behavior, combined with the uncertainty concerning the proportion and composition of melt lost, makes recovering a bulk composition of the particular protolith very unlikely (Palin et al., 2013). However, White & Powell (2002) showed that various melt-loss scenarios do not change the major sub-solidus and supra-solidus topologies or compositions of peritectic phases. It is therefore possible to calculate an approximate bulk composition suitable for prograde modeling. To reduce uncertainty, the melt-loss was modeled as a single extraction event, representing a simple end-member case. A melt-reintegrated bulk composition was therefore calculated by the addition of a proportion of melt to the observed bulk composition to displace the solidus down-temperature to H_2O-saturated conditions maximizing the amount of mica present prior to melting following the method of White et al., (2004). The composition of reintegrated melt was calculated at 7.75 kbar and 680 °C by using the solidus of the original bulk composition in the presence of kyanite. Although higher-pressure than final melt crystallization, this *P–T* value was chosen because it accounts for the presence of kyanite-bearing migmatites and inclusions in secondary muscovite at higher structural levels (TL15), allowing for a clockwise *P–T* evolution. It was determined that 10% melt should be added to make the solidus water-saturated.

Contours for modal proportion of silicate melt are presented in the supplementary material, and show that melt production across the wet solidus in garnet-bearing assemblages are negligible (~1%). It is not until fluid-absent muscovite dehydration occurs that melt generation reaches significant volumes, increasing from 4% to 12% over a very small temperature interval. Contours for calculated modal proportion of garnet allow interpretation of probable conditions of garnet core growth with respect to the melting history. Although garnet cores lack prograde compositional zoning, making the early stages of the *P–T* evolution poorly constrained, certain inferences can be made. The presence of muscovite inclusions within garnet suggest garnet nucleated prior to the muscovite dehydration melting reaction in a muscovite present field. The presence of kyanite relicts within secondary muscovite suggests that garnet grew when kyanite was stable. A possible interpretation involves a *P–T* evolution along an initial continental geotherm of 25-30 °C km^{-1}. This allows initial garnet growth to occur at ~ 600 °C and 6 kbar in an assemblage containing Bt–Ms–Pl–Ilm–Qtz–H_2O. Contours for modal proportion of garnet reveals that growth in muscovite-bearing assemblages was minor and significant growth of garnet was delayed until K-feldspar is produced as a result of muscovite dehydration along the effective solidus where the proportion of garnet increases significantly with increasing temperature. However, due to the presence of only ~1.5% garnet, we conclude temperatures did not increase significantly upon passing this melting reaction, and thus it is likely that crossing the effective solidus is largely related to de-compression at peak metamorphic conditions.

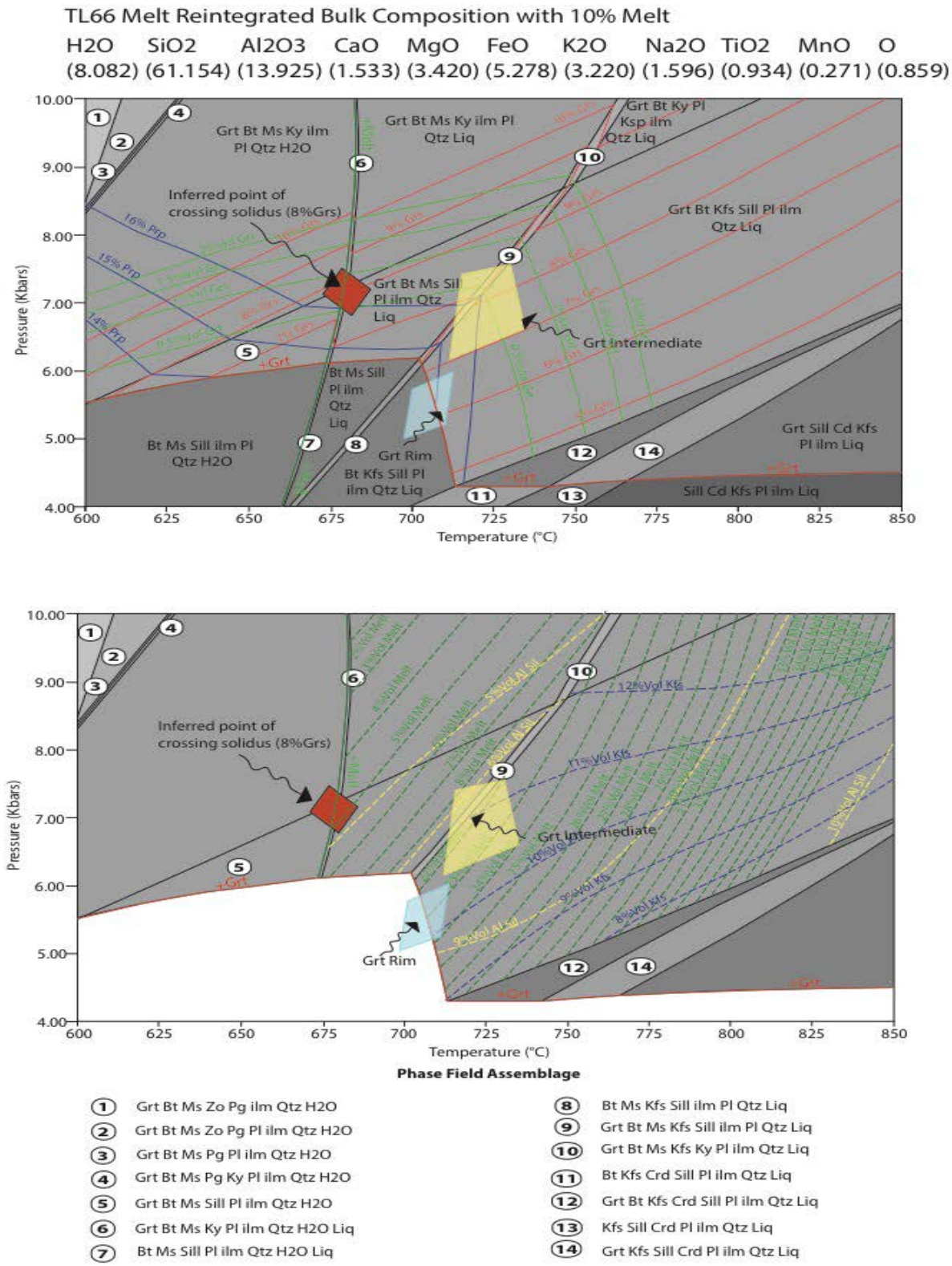

Figure 4.2.4: Melt-reintegrated pseudosection for sample TL66. 10% melt was assumed to be lost at the hydrous solidus at 7.75 kbars, 680 ℃. This predicts garnet rim compositions intersecting with the garnet out reaction at ca. 5.5 kbars, 710 ℃, consistent with garnet breakdown textures to biotite and secondary muscovite

5. References

Ashworth, J. R., 1975, The sillimanite zones of the Huntly Portsoy area in the north-east Dalradian, Scotland, Geological Magazine, v. 112, p. 113–136.

Bhattacharya, L., Mohanty,L., Maji, A., Sen, S. K., and Raith, M., 1992, Non-ideal mixing in the phlogopite-annite binary: Constraints from experimental data on Mg-Fe partitioning and a reformulation of the biotite-garnet geothermometer, Contributions to Mineral Petrology, v. 111, p. 87–98.

Carson, Powell and Clarke (1999), Calculated mineral equilibria for eclogites in $CaO–Na_2O–FeO–MgO–Al_2O_3–SiO_2–H_2O$: application to the Pouébo Terrane, Pam Peninsula, New Caledonia . Journal of Metamorphic Geology, v. 17, p. 9–24. doi:10.1046/j.1525-1314.1999.00177.x

Coggon, R. and Holland, T. J. B., 2002, Mixing properties of phengitic micas and revised garnet-phengite thermobarometers. Journal of Metamorphic Geology, v. 20, p. 683–696. doi:10.1046/j.1525-1314.2002.00395.x

Evans, B. W. and Guidotti, C. V., 1966, The sillimanite-potash feldspar isograd in western Maine, U.S.A. Contributions to Mineralogy and Petrology, v. 12, p. 25–62

Green, E.C.R., White, R.W., Diener, J.F.A., Powell, R., Holland, T.J.B. and Palin, R.M., 2016. Activity–composition relations for the calculation of partial melting equilibria in metabasic rocks. Journal of Metamorphic Geology, v. 34, p. 845–869.

Holland, T. J. B, and Blundy, J., 1994, Non-ideal interactions in Calcic amphiboles and their bearing on Amphibole-Plagioclase Thermometry: Contributions to Mineralogy and Petrology, v. 116, p. 433–447.

Holland, T. J. B., and Powell, R., 1998, An internally-consistent thermodynamic dataset for phases of petrological interest. Journal of Metamorphic Geology, v. 16, p. 309–344.

Holland, T. J. B. and Powell, R., 2011, An improved and extended internally consistent thermodynamic dataset for phases of petrological interest, involving a new equation of state for solids. Journal of Metamorphic Geology, v. 29, p. 333–383. doi:10.1111/j.1525-1314.2010.00923.x

Holland, T. J. B., Baker, J. M., and Powell, R., 1998, Mixing properties and activity–composition relationships of chlorites in the system MgO–FeO–Al2O3–SiO2–H2O. European Journal of Mineralogy, v. 10, p. 395–406.

Holland, T. J. B., 2009, AX: a program to calculate activities of mineral end-members from chemical analyses. Available at: http://www.esc.cam.ac.uk/research/research-groups/holland/ax.

Kohn, M. J. and Spear, F. S., 2000, Retrograde net transfer reaction insurance for pressure–temperature estimates. Geology, v. 28, p. 1127–1130.

Mahar, E. M., Baker, J. M., Powell, R., Holland, T. J. B. and Howell, N. 1997, The effect of Mn on mineral stability in metapelites. Journal of Metamorphic Geology, v. 15, p. 223–238. doi:10.1111/j.1525-1314.1997.00011.x

Palin R. M., Searle, M. P., Waters, D. J., Parrish, R. R., Roberts, N. M. W., Horstwood, M. S. A., Yeh, M.-W., Chung, S.L., and Anh, T.T., 2013, A geochronological and petrological study of anatectic paragneiss and associated granite dykes from the Day Nui ConVoi metamorphic core complex, North Vietnam: constraints on the timing of metamorphism within the Red River shear zone, Journal of Metamorphic Geology, v. 31, p. 359–387. doi: 10.1111/jmg.2013.31.

Palin, R.M., Weller, O.M., Waters, D.J. and Dyck, B., 2016, Quantifying geological uncertainty in metamorphic phase equilibria modelling; a Monte Carlo assessment and implications for tectonic interpretations. Geoscience Frontiers, v. 7, p.591–607.

Powell, R., Holland, T.J.B., 1988. An internally consistent dataset with uncertainties and correlations: 3. Application to geobarometry, worked examples and a computer program. Journal of Metamorphic Geology 6, 173–204, doi: 10.1111/j.1525-1314.1988.tb00415.x.

Sawyer, E. W., 1996, Melt segregation and magma flow in migmatites: Implications for the generation of granite magmas, Special Paper Geological Society of America, v. 315, p. 85–94, doi:10.1130/0-8137-2315-9.85.

Spear, F. S., 1993, Metamorphic Phase Equilibria and Pressure–Temperature–Time Paths. Mineralogical Society of America, Monograph Series, Washington, DC.

White, R. W. and Powell, R., 2002, Melt loss and the preservation of granulite-facies mineral assemblages. Journal of Metamorphic Geology, v. 20, p. 621–632.

White, R. W., Pomroy, N. E. and Powell, R., 2005. An in-situ metatexite–diatexite transition in upper amphibolite-facies rocks from Broken Hill, Australia, Journal of Metamorphic Geology, v. 23, p. 579–602.

White, R. W., Powell, R. and Baldwin, J. A., 2008, Calculated phase equilibria involving chemical potentials to investigate the textural evolution of metamorphic rocks. Journal of Metamorphic Geology, v. 26, p. 181–198.

White, R. W., Powell, R. and Clarke, G. L., 2002, The interpretation of reaction textures in Fe-rich metapelitic granulites of the Musgrave Block, central Australia: constraints from mineral equilibria calculations in the system K_2O–FeO–MgO–Al_2O_3–SiO_2–H_2O–TiO_2–Fe_2O_3. Journal of Metamorphic Geology, v. 20, p. 41–55.

White, R. W., Powell, R. and Halpin, J. A., 2004, Spatially focused melt formation in aluminous metapelites from Broken Hill, Australia. Journal of Metamorphic Geology, v. 22, p. 825–845.

White, R. W., Powell, R. and Holland, T. J. B., 2007, Progress relating to calculation of partial melting equilibria for metapelites. Journal of Metamorphic Geology, v. 25, p. 511–527.